RC/1
Review

RCA Review

Contents

Differential gain is defined as the change in amplitude of the subcarrier at the receiving end as the luminance varies from blanking level to white level, the average picture level being maintained at a particular value. Taking the blanking level value of the subcarrier as reference, the differential gain is quoted as the largest departure from the reference amplitude, expressed as a percentage.

Differential phase is defined as the change in phase of the subcarrier at the receiving end as the luminance varies from blanking level to white level, the average picture level being maintained at a particular value. Taking the blanking level section of the subcarrier as reference, the differential phase is quoted as the largest departure from the reference phase, expressed in degrees.

2. Test Signals

Test signals that allow the measurement of differential gain and differential phase distortions are shown in Fig. 1a–c. The figure show a horizontal sawtooth going from picture black to picture white and a 5-step or a 10-step staircase. The staircase and the sawtooth have a small amount of subcarrier added to them during the active portion of the line. The amount of subcarrier should be as small as possible so that only a small fraction of the luminance level is explored at each point. However, reducing the amplitude too far would produce a S/N ratio problem in the measurement. Thus, forty IRE units is the recommended superimposed subcarrier amplitude.

Using either the sawtooth or the staircase, a single test line can be followed by either three black lines (at 10% video) or three white lines (at 90% video) to evaluate differential gain and differential phase behavior under different average picture levels. A Tektronix 147A NTSC test signal generator is one device that can provide these waveforms, which are shown in Figs. 2a and 2b.

3. Test Set Up

The Tektronix 147A NTSC signal generator was used to supply the 10-step staircase with superimposed subcarrier. An EIE TV modulator with a GDP1A1 group-delay predistortion network was employed to provide a TV signal on channel #3 (61.25 MHz pix carrier). The test setup is shown in Fig. 3.

When measuring differential gain and differential phase distortions in television receivers, the test signal should be taken off with a low capacitance probe after the second detector, amplified, and fed to a Tektronix 520A vectorscope for measurement and display. The signals shown
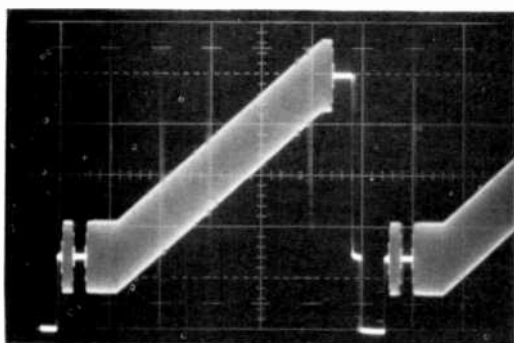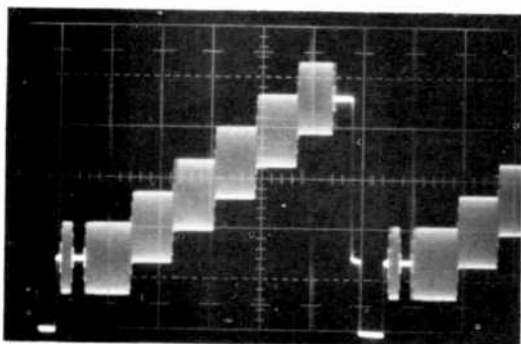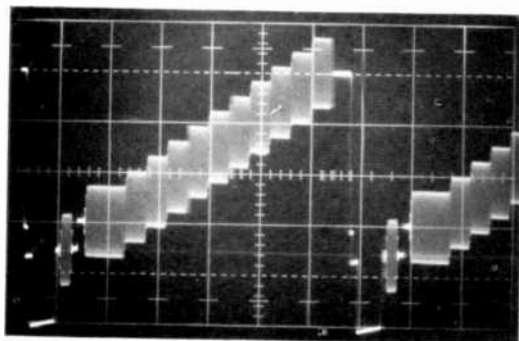
Fig. 1—Test waveforms from a Tektronix 147A used to test linearity and differential gain and phase distortions: (a) shows a horizontal sawtooth with superimposed subcarrier, (b) a horizontal 5-step staircase, and (c) a horizontal 10-step staircase.
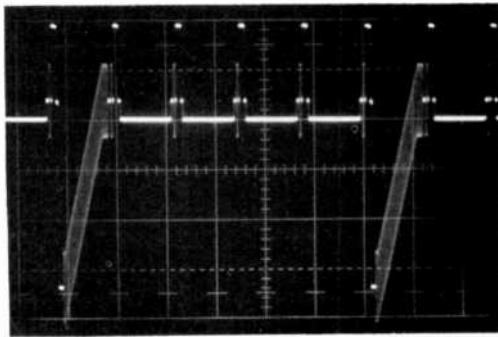
(a)
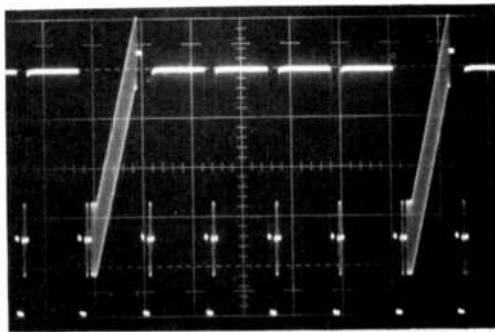
(b)

Fig. 2—Test waveforms, generated as in Fig. 1, used to check for differential gain and phase distortions under different average picture levels: (a) shows a horizontal ramp followed by three black lines and (b) horizontal ramp followed by three white lines.

in Fig. 4a, b, and c depict some examples of test data obtained by this technique.

4. The Distortions

The differential gain and differential phase distortions of a number of color TV receivers were measured. It was found that the shape and magnitude of these distortions can vary substantially. The shape and magnitude of the differential gain and differential phase distortions affects the displayed colors on the receivers kinescope. If a total impression of color errors is considered important, it is not sufficient to quote a single number or a maximum distortion value. Colors will be affected differently depending on the location of the subcarrier phase or gain distortion with respect to the luminance level.
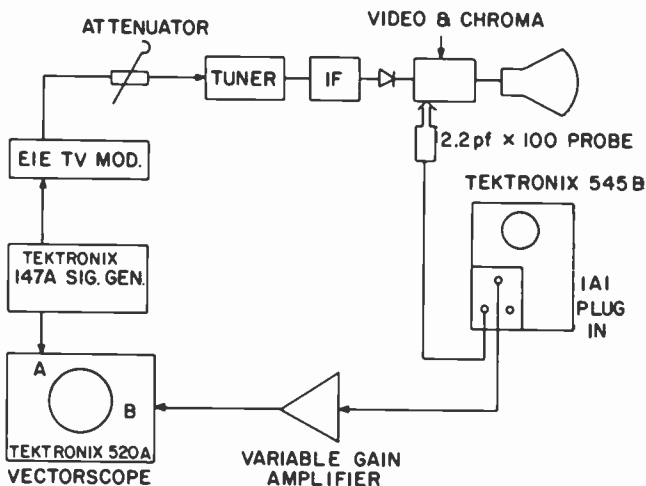
Fig. 3—Test setup for differential gain and phase measurements.

To classify the performance of TV receivers with respect to differential gain and differential phase errors, one must convert the shape, the direction, and the magnitude of differential gain and differential phase distortions into perceived color error values.

A good treatment of the subjective effects of differential gain and differential phase distortions in NTSC color television pictures is given in Ref. [2]. The present paper is of a general nature, and with the computer program described here, it is possible to change every parameter that affects the color rendition in the total TV system.

This paper is primarily concerned with providing a tool that allows the assessment of various differential gain and differential phase distortions and judgement as to the trade-offs in the shape and magnitude of these errors versus perceived color errors.

A representation of a typical differential gain distortion measured from the antenna input terminals to the output of the second detector of a commercial color TV set is shown in Fig. 4a. Fig. 4c is a photo of a vectorscope display showing differential gain and 4b shows differential phase errors. The overall differential gain and differential phase errors from an experimental video signal encoder to the output of a player amplifier, are shown in Fig. 5.

Differential gain is considered to be positive if the amplitude of the subcarrier signal increases, or negative if the amplitude of the subcarrier signal decreases with increasing luminance signal level. Similarly, differential phase is positive if the phase of the subcarrier signal increases or negative if the phase decreases with increasing luminance signal level.
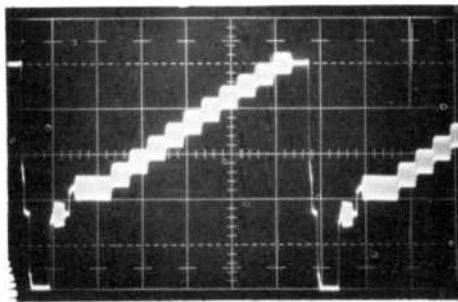
(a)
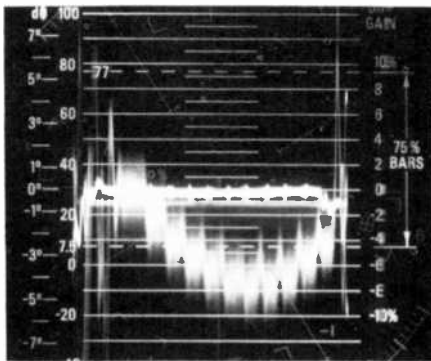
(b)
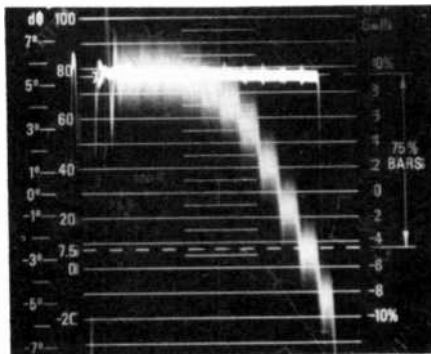
(c)

Fig. 4—10-step staircase test signal with superimposed subcarrier used to measure differential phase and gain distortion: (a) test signal at the output of the 2nd detector of a commercial color TV receiver, (b) differential phase distortion for the receiver, and (c) differential gain distortion for the receiver. (b) and (c) were measured with a Tektonix 520A vectorscope.
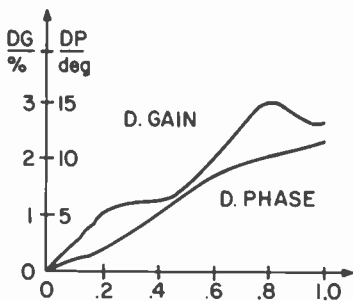
Fig. 5—Phase and gain distortion from an experimental video signal simulator and processor.

5. The Computer Program

A FORTRAN IV computer program for conversion of differential gain and differential phase distortions into perceived color errors has been developed. Through the use of subroutines, which were available for general colorimetry evaluation, this program allows us great flexibility in data input and data output.

The block diagram in Fig. 6 shows the various stages of conversion a light signal undergoes from the scene to the display output. Each one of the blocks can be addressed and defined from the computer terminal. This allows us to evaluate systems other than standard NTSC or to change NTSC parameters to judge their effect on perceived color errors for a given set of differential gain and differential phase distortions. Also we can assess transmitter gamma or shifts in camera primaries.

Similarly, the receiver can be defined when addressing the program from a computer terminal. This includes the change of the receiver demodulator and the insertion of any corrective matrix and display parameters such as phosphor primaries, kine gamma, and display white. Particular emphasis has been given to the flexibility of differential-gain and differential-phase distortion data input.

When calculating perceived color errors, a single differential gain number is meaningless without the associated luminance value. If only one differential gain value is given, the computer assigns this single error number to the highest luminance value of 1.00. It then interpolates the error for the set of chosen test colors linearly from the given differential gain value at maximum luminance to 0% at zero luminance. The same analogy holds true for the differential phase distortions. If only a single distortion number is entered, the intermediate values are interpolated linearly from the maximum phase angle at maximum luminance to zero degrees at zero luminance.

SCENE

$x \rightarrow$ $\bar{X}$ | R | $\frac{1}{\gamma}$ | R' | $Yo' = 30R' \cdot 59G' \cdot 11B'$ | Yo'
$y \rightarrow$ $\bar{Y}$ | G | | G' | $.877 \cdot (R'-Yo') \rightarrow$ | COMPOSITE NTSC SIGNAL
$\bar{Y} \rightarrow$ $\bar{Z}$ | B | | B' | $.493 \cdot (B'-Yo') \rightarrow$

$\begin{array}{ccc} x & u & \bar{X} \\ y & v & \bar{Y} \\ \bar{Y} & \bar{Y} & \bar{Z} \end{array}$ CAMERA MATRIX (NTSC)   CAMERA (TRANSMITTER) γ

Yo' + SUBCARRIER

TO RECEIVER

DISPLAY

$\left\{ \begin{array}{l} Yo' \\ SC\ AMPL \\ SC\ PHASE \end{array} \right\}$ Yo'' SC'' | DEMOD. OR CORRECTIVE MATRIX | Yo' $R'-Yo'$ $B'-Yo'$ | KINE DRIVER | Rm' Gm' Bm' | γ | Rd Gd Bd | DISPLAY MATRIX | $\bar{X}$ $\bar{Y}$ $\bar{Z}$

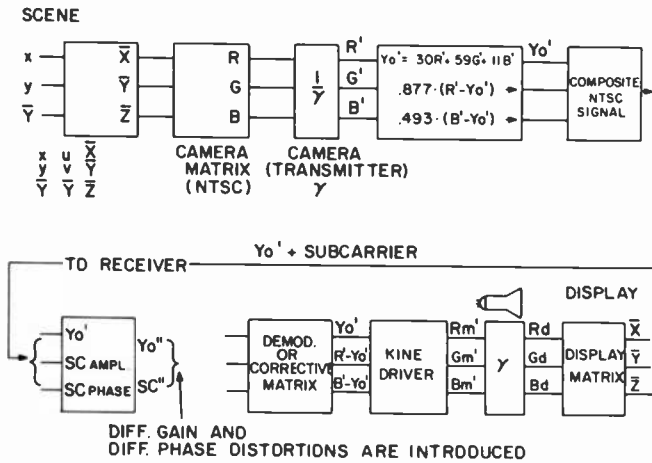DIFF. GAIN AND DIFF. PHASE DISTORTIONS ARE INTRODUCED

Fig. 6—Block diagram of computer program showing computational flow from the scene to the displayed color.

If, however, the differential gain and differential phase distortion curve is known, up to 100 pairs of differential gain and associated luminance values and up to 100 pairs of differential phase distortions, with their associated luminance values, can be entered as data.

The differential gain and differential phase errors for the test color luminance for which no distortion value has been entered is again linearly interpolated. This simulates a typical change in chroma subcarrier amplitude and angle that might be experienced, e.g., in the i-f portion of a TV receiver.

The differential gain and differential phase error introduction in the computer program takes place before demodulation, thereby simulating errors which, in real life, could have been introduced at the TV receivers rf, i-f, second detector, or chroma bandpass stage. This is shown in the block diagram in Fig. 6.

The data output from the computer program is available in a number of forms. The output can be in terms of a color shift in CIE x,y or u,v coordinates, in terms of XYZ tristimulus values, as U^*, V^*, W^* values, as equivalent linearized electrical signals RGB, or as gamma distorted electrical signals R' G' and B'. Color error output is available in $(UVW)^*$ units with and without the Eastwood modification. This modification allows us to place weighting factors to the U^*, V^* and W^* values to make the $(UVW)^*$ color error more perceptually linear.

Finally, the output data can be obtained within a file that is suitable for two dimensional plotting on a Tektronix or Hewlett Packard graphic display device. Files can be combined to allow three-dimensional plotting

wherever available. If a great number of data computations have to be done, computational data and final output values can be written into a data file and printed off line for savings in time and money.

For specific cases involving differential gain and phase distortions where the mean color error for a given set of test colors is much larger than in a reference case, one can easily decide on a merit rating. If the $(UVW)^*$ mean color errors are very similar in value, the color shifts for each set of differential gain and differential phase distortions can be examined on a CIE diagram. One could then use the color shifts seen on a CIE plot to select appropriate test slides to perform a subjective viewing test.

6. The Distortion Shapes

Six sets of general distortion shapes were evaluated for the special case of an NTSC transmitter, display field phosphors, a display gamma of 2.2, and the receiver demodulator matrix given in Sec. 7.1.

First: A set where the distortion increases linearly from zero at black level to a maximum at luminance white (Fig. 7), i.e., DG or $DP = \overline{Y}k$ where k is a constant. Positive and negative differential gain and differential phase values were evaluated.
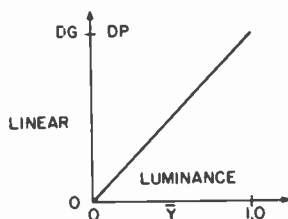
Fig. 7—Linear distortion shape (general case).

Second: A quadratic distortion shape from zero to maximum luminance for differential gain and for differential phase errors (Fig. 8).

Third: The differential gain and differential phase shapes found in many color TV sets were very similar to a SINE characteristic (see Fig. 9). Therefore one of the distortion shapes evaluated in a general form was that of a sine curve: (DG or $DP = \sin(\pi\overline{Y})$).

Fourth: A set of differential gain and differential phase distortion numbers derived from a current production color television set.

Fifth: Two sets of differential gain and differential phase distortions measured on two i-f chips for the purpose of determining which one causes larger perceived color errors.

Sixth: The differential gain and differential phase distortion measured
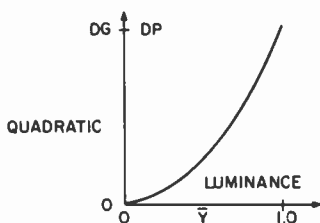
Fig. 8—Quadratic distortion shape (general case).
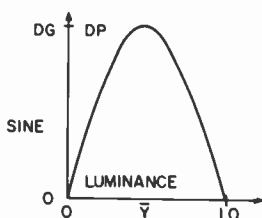
Fig. 9—Sine distortion shape (general case).

in an experimental video signal processor were shown in Fig. 5. The processor consisted of encoding a buried subcarrier at 1.5 MHz, simulating FM modulation, signal pick-up from a recording media, FM demodulation, and recoding NTSC.

7. Results

Color shifts and color errors for a series of differential gain and differential phase distortions have been computed for the general distortion shapes—linear, quadratic, and sine wave. The distortions ranged from plus/minus 20% to 1% and from plus/minus 20 degrees to one degree. The results are shown as $(UVW)^*$ color errors in diagram form and as color shifts on a CIE diagram.

7.1 The Linear Distortion Shape

The $(UVW)^*$ mean color error as a function of differential gain for selected phase values is shown in Fig. 10 for the linear distortion shape, where the differential gain and differential phase distortion increases linearly from zero at black level to a maximum at luminance white (see Figure 7).

Phase distortions, especially negative ones, produce a higher mean color error than differential gain distortions. Fig. 10 shows 12 $(UVW)^*$
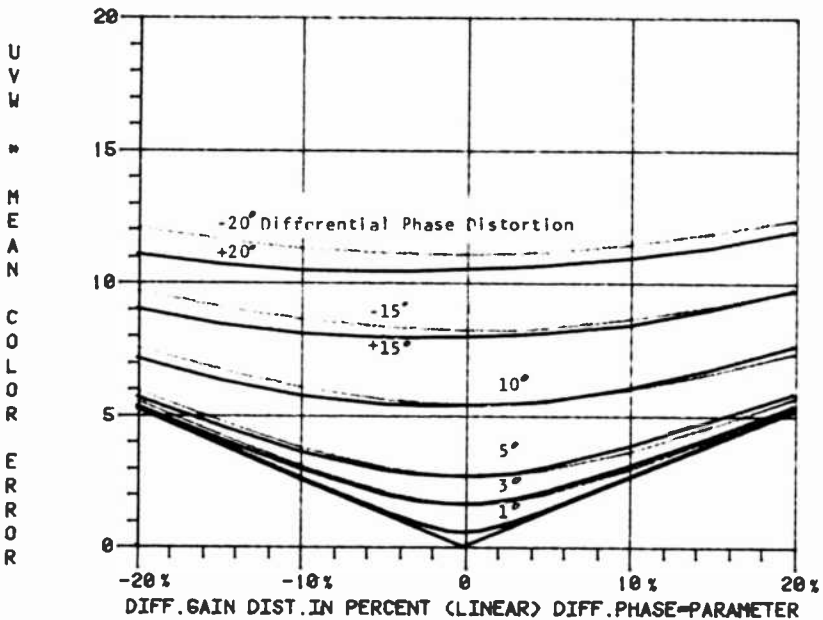
Fig. 10—Mean color errors versus differential gain distortion for linear distortion shape.

units of color error for -20 degrees of differential phase but only 6 $(UVW)^*$ units for plus or minus 20% differential gain distortion. The color shifts caused by a differential gain and differential phase error with a linear distortion shape are shown in Fig. 11.

In the CIE diagram in Fig. 11, a vector points from the scene color to the display color. This is the color rendition without differential gain and differential phase distortion. A number of vectors fan out from that display color. The endpoints of those vectors depict the displayed color with 20% differential gain and a number of fixed differential phase values. The color shifts are plotted for a set of 36 selected colors. Not all of the 36 colors can be clearly identified on the plot. Some of those colors are primary colors and no shift takes place in the transformation from primary colors to the display phosphor colors. Some scene colors have the same x-y coordinates but different luminance values. The color shift for the color with a different luminance value will be the same, but a $(UVW)^*$ color-error computation will show the difference in visibility. Only 22 colors, of the set of 36 used for plotting, are used for color-error computations.

The demodulation matrix used for the color shift and color error calculations is given below in terms of gains and angles and in a 3×3

format:

Demodulation Matrix				Gains and Angles	
Red	1.58	−0.42	−0.16	R-Y	2.06	94.5°
Green	−0.09	0.97	0.12	G-Y	0.7	−100.5°
Blue	0.03	−0.20	1.17	B-Y	2.47	3.5°
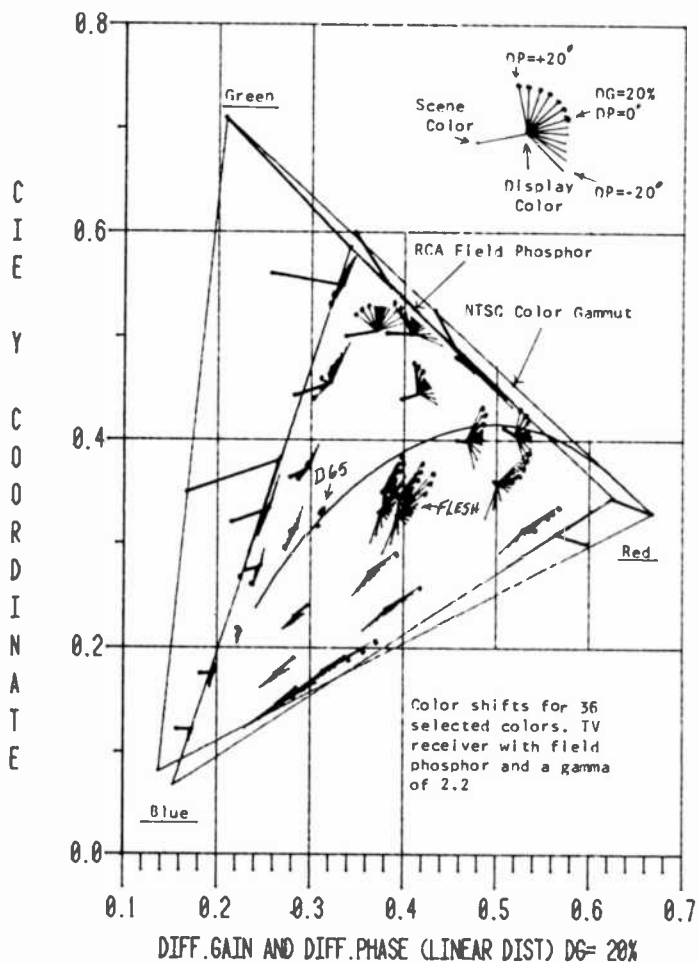
Fig. 11—CIE diagram for linear distortion shape.

7.2 The Quadratic Distortion Shape

The distortion increases in a quadratic form from zero to maximum luminance (see Fig. 8).

The same set of plots as for the linear-distortion shapes are provided for the quadratic distortion shapes. They are shown in Fig. 12, which shows the $(UVW)^*$ mean color error for various differential gain distortions and fixed differential phase errors, in Fig. 13, which shows the color shifts for differential gain and differential phase errors on a CIE x-y diagram. The quadratic distortion shape produces the smallest color errors of the three general distortion shapes evaluated.

7.3 The Sine Distortion Shape

The third of the general form of distortions has the shape of a sine wave (see Fig. 9). The differential gain or the differential phase increases from zero at black level to a maximum at 50% luminance and decreases again to zero at maximum luminance.
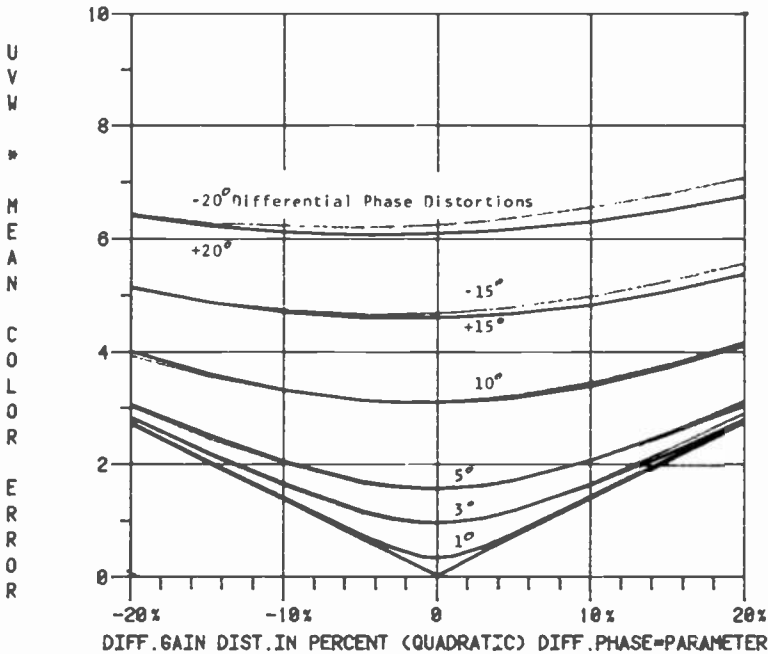
Fig. 12—Mean color errors versus differential gain distortion for quadratic distortion shape.
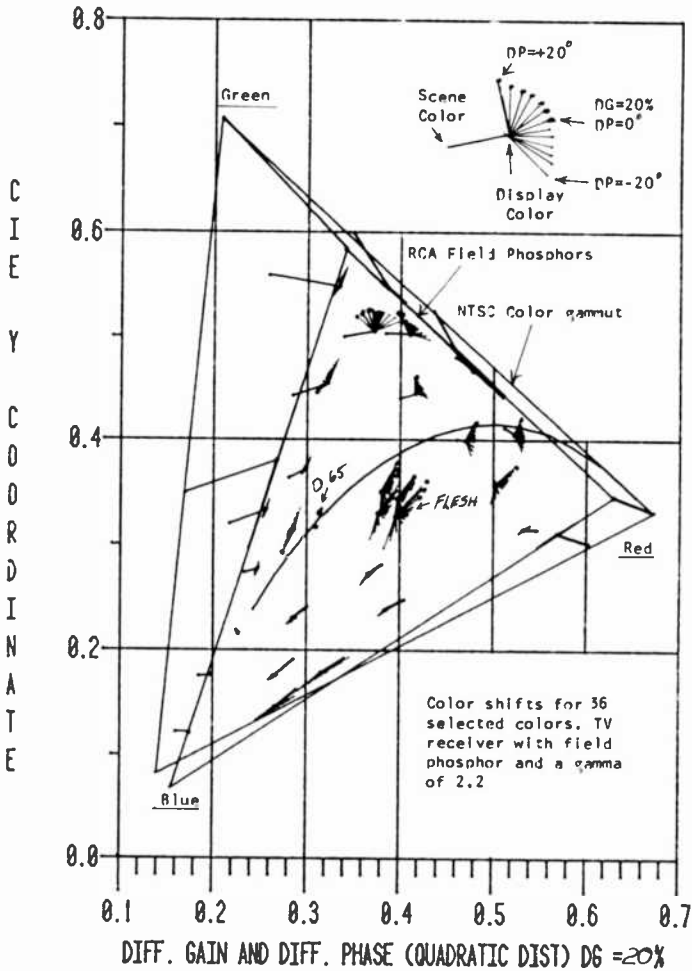
Fig. 13—CIE diagram for quadratic distortion shape.

Fig. 14 shows the $(UVW)^*$ mean color error for various differential gain distortions and fixed differential phase values.

The sine distortion shape causes the biggest color errors (see Fig. 15). The smallest color errors are caused by a quadratic differential gain and differential phase distortion shape. This is partially due to the selection of our set of test colors, most of which have luminance levels between 30% and 70%.
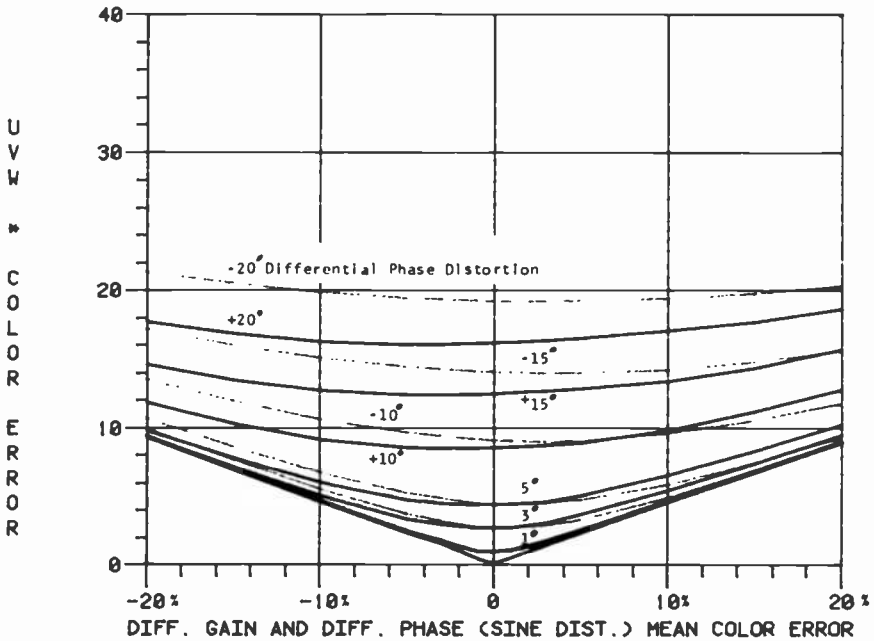
Fig. 14—Mean color errors versus differential gain distortion for sine distortion shape.

8. Application to a Typical Color TV Set

When judging the effect of differential gain and differential phase distortions on perceived color errors it was felt that the use of too many primary and complimentary colors should be avoided, since primary colors are not most dominant in the average transmitted color-TV picture material.

The color error characteristics produced for various general differential gain and differential phase distortion shapes for the typical domestic receiver we used as an example are very similar to the findings of Cavanaugh and Lessman[2,5] in their subjective study of differential gain and differential phase distortions in NTSC color TV pictures and of C. B. Neal[4] in his paper on the quantitative colorimetric effects of differential gain and differential phase distortions. One might suspect that, but one certainly could not have predicted it.

The sample set with differential gain and differential phase distortions compared to the same set without differential gain and differential phase errors shows a mean color error of 2.4 (UVW)* units. The CIE diagram in Fig. 16 shows the color shifts from the scene to the display with and without differential gain and differential phase distortions.

A single (UVW)* mean color error number was used to compare two
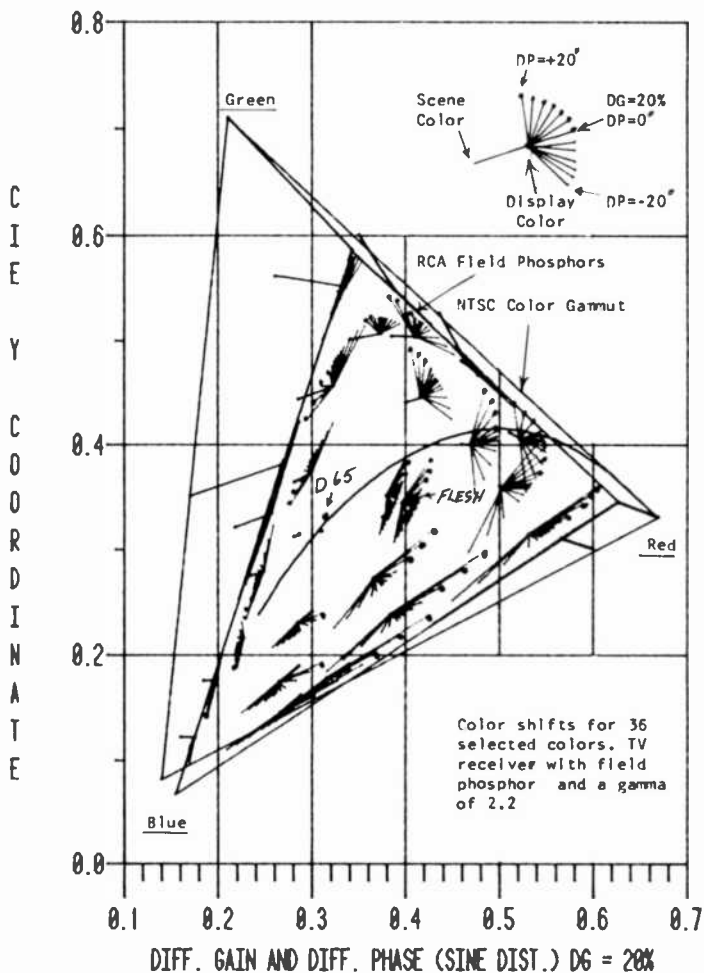
Fig. 15—CIE diagram for sine distortion shape.

i-f IC's with different differential gain and differential phase distortions. It turned out that both IC's exhibited about the same $(UVW)^*$ color error, a fact which was not apparent by just examining the measured differential gain and differential phase values. This information allows a judgement of the expected quantitative colorimetric effects of i-f IC's.
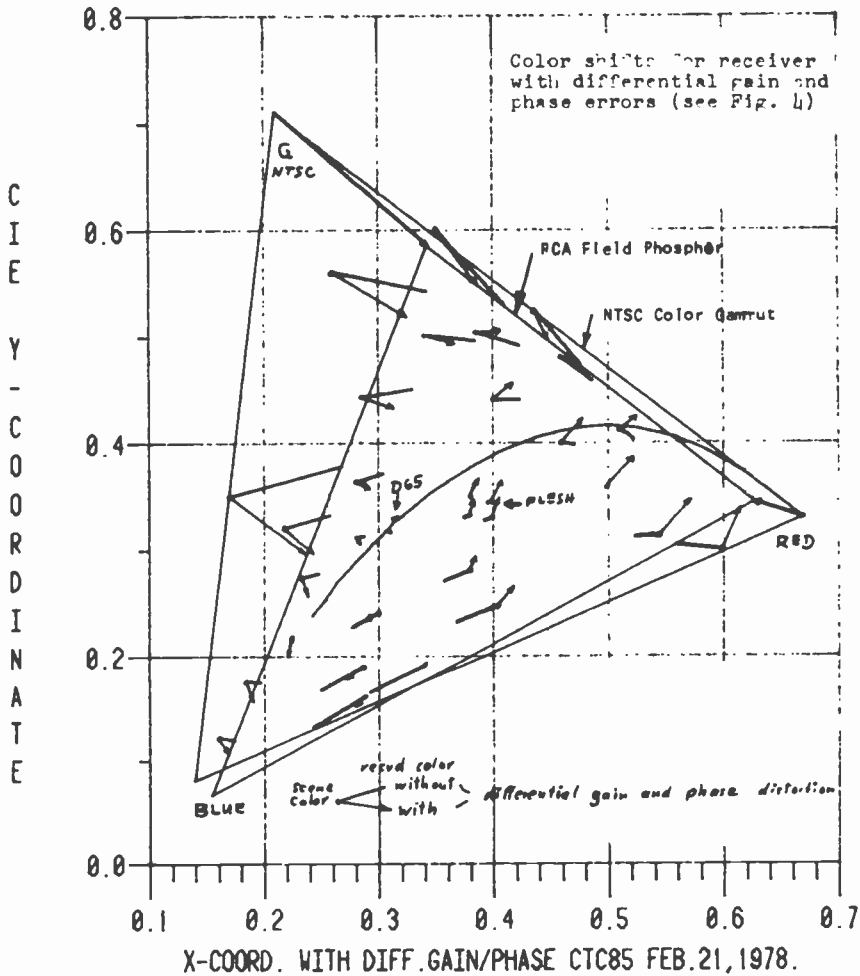
Fig. 16—CIE diagram for a typical modern color TV receiver. Color shifts for 36 selected colors; receiver with field phosphor and a kine gamma of 2.2.

9. Experimental Video Signal Simulator

The color shifts caused by differential gain and differential phase distortions of an experimental video signal simulator and video processor are shown in a CIE diagram. Combining the displayed colors without differential gain and differential phase distortions with one with differential gain and differential phase distortions yields the vectors seen in the CIE diagram in Fig. 17.

The differential gain and differential phase distortion shapes used in those calculations were shown earlier in Fig. 5.
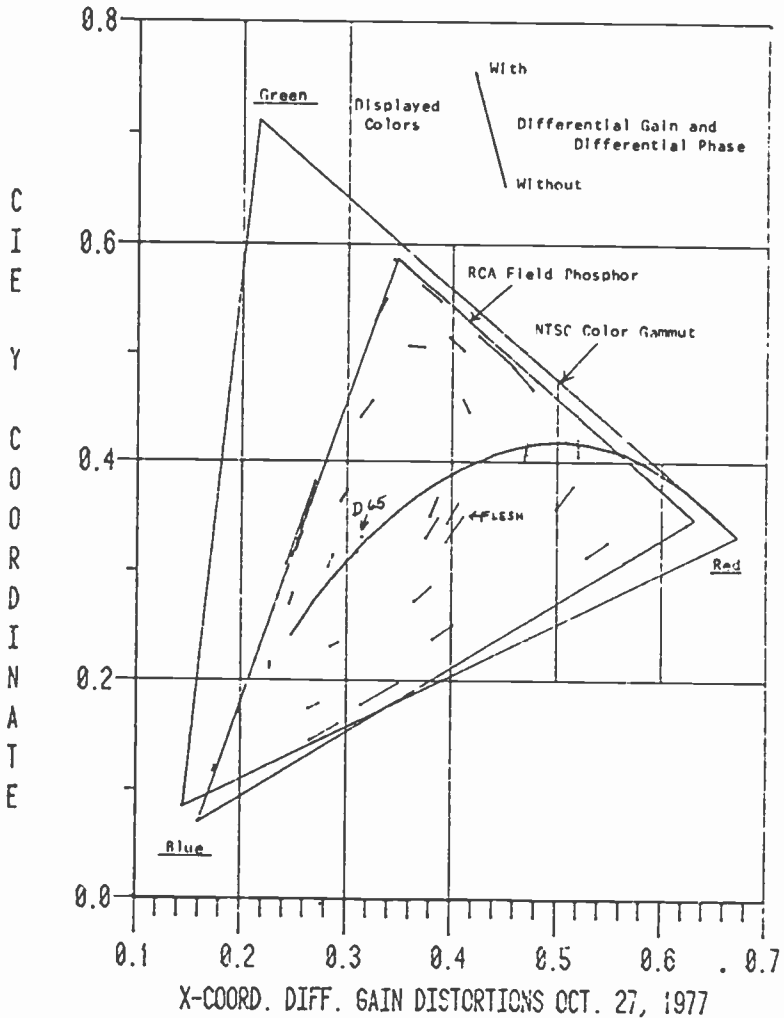
Fig. 17—CIE diagram of color shifts for a video signal processor and simulator with differential gain and phase errors (see Fig. 5).

10. Conclusion

A computer program to convert differential gain and differential phase distortions into perceived color errors is described. It can encompass most of the parameters between camera scene and receiver display that affect the system colorimetry. The quantitative colorimetric effects of differential gain and differential phase errors in a TV system can be shown in various forms.

The reason for the present investigation was to assess the effects on perceived color errors for NTSC signals with differential gain and differential phase distortions using display devices whose primary phosphors differ substantially from the NTSC primaries.

Additionally, the computer serves as a tool to evaluate the effect of distortions of subsystems on the displayed TV picture.

Acknowledgments

References

[1] L. E. Weaver, "Television Measurement Techniques," pp. 112–138, *Linear Waveform Distortion*, Peter Peregrinus Ltd., 2 Savoy Hill, London WC2R OBP.

[2] John R. Cavanaugh and Anthony M. Lessman, "Subjective Effects of Differential Gain and Differential Phase Distortions in NTSC Color Television Pictures," *J. SMPTE*, **80**, p. 614, Aug. 1971.

[3] H. P. Kelly, "Differential Phase and Gain Measurements in Color Television Systems," *Elec. Eng.*, **73**, p. 799, Sept. 1954.

[4] C. Bailey Neal, "The Quantitative Colorimetric Effects of Differential Gain and Differential Phase Distortions in NTSC Color Television Pictures," *IEEE Trans. on Consumer Electronics*, Feb. 1976.

[5] Anthony M. Lessman, "Subjective Effects of Delay Differences Between Luminance and Chrominance Information of the NTSC Color Television Signal," *J. SMPTE*, **80**, p. 620, Aug. 1971.

[6] C. A. Siocos, "Numberical Values for Subjective Picture Quality in Television, *J. SMPTE*, **80**, p. 958, Dec. 1971.

[7] M. T. Salter and M. O. Felix, "Improved Techniques for Measuring Phase and Gain in Digitized Video Signals."

[8] K. W. Robinson and J. J. Heinzl, "Measurement of Non-Linear Distortion on the Video Signal," *Marconi Instruments (GB)*, **13**, No. 4, p. 78, May 1972.

[9] A. Polemski, "Analysis of Different Methods in Adding Up of Differential Phase and Differential Gain of Color Television Signals," *Rozprawy Elektrotechniczne*, **19**, 7.3, pp. 561–578, 1973.

[10] C. W. Rhodes, "Measuring Distortions in the Television Signal," Tektronix Brochure A-2495, 1972.

[11] NTC Report No. 7, prepared by the Network Transmission Committee of the Video Transmission Engineering Advisory Committee, June 1975 (Revised Jan. 1976), Published by the Public Broadcasting Service for the Network Transmission Committee: ABC, ATT, CBS, NBC, PBS.

High-Power Low-Loss PIN Diodes for Phased-Array Radar

A. Rosen, R. U. Martinelli, A. Schwarzmann, G. J. Brucker, and G. A. Swartz

RCA Laboratories, Princeton, N.J. 08540

Abstract—This paper deals with the development of improved PIN diodes for use in phase shifters. Diodes having different geometries and using special fabrication techniques are described. System requirements, including survival in a radiation environment and circuit size, have led to special diode designs. Radiation-hardening experiments have resulted in a set of device design-parameter curves for high-power diodes resistant to neutron radiation. Circuit size of the phase shifters has been reduced by incorporating impedance-transformation networks in the branch hybrids. In addition to the above investigations, storage-time variations in silicon PIN diodes have been studied.

   PIN diodes have been demonstrated to operate at pulse peak power levels as high as 7 kW, at pulse widths of 50 μsec. The breakdown voltage of these diodes exceeds 1700 V, and the forward resistance at 50 mA is 0.3 ohm.

Preface

This paper is based on a number of articles on the subject of PIN diode research at RCA. The authors felt that editing the various articles into one paper would enable the reader to follow the progress made in the development of PIN diodes at RCA Laboratories in the last two years.

1. Introduction

In the past, power switching in phased-array radar antennas had involved large volume ferrite phase shifters. To reduce the cost, as well as the weight and volume of the antennas, PIN diodes have been developed to operate at S-band (3.1–3.5 GHz) as power switches, replacing the ferrite elements. A phased-array radar system can have many thousands of elements, with a phase shifter for each; therefore, the achievement of a low-cost radar system is closely related to the use of PIN diode switches (as compared to ferrite type phase shifters). When incorporated in microwave integrated circuits, the PIN diode phase shifter is very small, providing the additional significant advantage of a lightweight, thin array face.

This paper deals with the development of PIN diode phase shifters using improved diode fabrication techniques and diodes of different geometrical forms in accordance with system applications. PIN diodes have been designed to operate at pulsed peak power levels as high as 14 kW for 50-μsec pulse widths. The forward resistance of these diodes is 0.3 ohm at a forward current of 50 mA. The diodes are fabricated from single-crystal, high resistivity silicon wafers with deep diffused boron and phosphorus-doped contact layers. The diode's heat sink and heat capacitor are 75 μm of plated gold. Passivation layers of SiO_2 and Si_3N_4 on the exposed sidewalls of the diode enable it to pass stress tests, such as moisture resistance, temperature cycling, thermal shock, and reverse blocking voltage tests.

Neutron damage in PIN diodes has been investigated, and the experimental results are analyzed in this paper. In particular, experimental diodes subjected to a fluence of 4.4×10^{13} n/cm^2 operated at 4 kW rf power level without burnout.

Using the reverse-recovery technique, storage time variations have been investigated as a function of forward current density and diode diameter. The analysis of these measurements has led to an improved understanding of the operational characteristics of the diode, especially as these properties relate to loss, power handling, and switching time.

In this paper, we first discuss diode fabrication. This is followed by sections on passivation and stress tests, diode performance, and storage time variations in silicon PIN diodes (p^+-n-n$^+$). Also included is a discussion of neutron damage. Last we present circuit design considerations, including a discussion of the hybrid coupled-diode phase shifter and circuit parameters as determined by diode characterization.

2. PIN Diode Characteristics and Design Considerations

A PIN diode is composed of a lightly doped n-type region bounded by a heavily-doped p^+ type layer on one side and a heavily-doped n^+ type layer on the other. The lightly doped n layer is generally referred to as the i region, or i layer, since under normal forward biasing the injected charge density far exceeds the background impurity density. When the diode is reverse-biased, the i region is depleted of mobile charge, so that the diode approximates a low-loss parallel-plate capacitor. During forward biasing, holes and electrons are injected into the i region from the p^+ and n^+ layers, forming a dense plasma that substantially increases the i-layer conductivity.

The design of low-loss, high-breakdown PIN diodes for use at high power levels in an S-band phase shifter requires an evaluation of the effects of the following four device parameters on device performance:

(1) the i-region thickness,
(2) the i-region resistivity,
(3) the injected carrier lifetime,
(4) the diffusion profile of the n^+ and p^+ contact layers.

The i region's thickness, W, strongly influences the forward resistance R_f, the diode Q, and the thermal properties of the diode. The breakdown voltage V_B of the diode is a linear function of W.

The forward resistance is the sum of the plasma resistance, the diffusion resistance, contact resistance, and series resistance of the contact layers. At high frequencies, the plasma resistance is two orders of magnitude greater than the remaining resistance components and is given by[1]

$$R_f = W^2/(I_f \tau_e \mu), \qquad [1]$$

where μ is the sum of the hole and electron mobilities and τ_e is the injected carrier lifetime in the i region.

The Q of the diode at a given bias voltage is a function of the resistivity and thickness of the i layer as well as of the resistance of the contacts and contact layers. With stray capacitance neglected, the equivalent circuit of the diode is shown in Fig. 1. The diode Q for small signals is

$$Q = \frac{1}{C_o(r_s + \rho_c/A) + R_s} + \left(1 + \frac{C_1}{C_o}\right)\omega\tau_D \qquad [2]$$

where

R_s = the resistance of the undepleted portion of the i layer,
C_o = capacitance of the carrier depleted portion of the i layer,
C_1 = capacitance of the undepleted portion of the i layer,
$\tau_D = C_1 R_s$ = dielectric relaxation time of undepleted i layer,
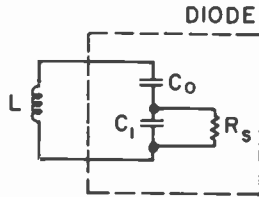
Fig. 1—Equivalent circuit of PIN diode.

ρ_C = is the specific contact resistance,
A = the junction area,
r_s = the series resistance of the contact layers.

The depletion distance X in the i layer is described by the Poisson equation

$$\frac{\partial^2 V}{\partial X^2} = -\frac{e}{\epsilon} N(X).$$ [3]

For a constant density profile $[N(X) = N_o = \text{constant}]$,

$$V + V_o = \frac{e}{2\epsilon} N_o X^2,$$ [4]

where V_o is the barrier potential at the p^+–n junction. Eqs. [2], [3], and [4] indicate that for a given bias potential, V_D, and a given charge carrier density, N_o, the carriers in the i layer are depleted if

$$W < \left(\frac{2\epsilon(V_o + V_D)}{eN_o}\right)^{1/2}.$$

For a 40 V reverse bias and an i-layer doping density, $N_o = 2 \times 10^{12}$ cm^{-3}, $W < 0.016$ cm for punchthrough. High Q is achieved by reducing W as much as possible within the confines of the breakdown potential. A high-Q diode implies a high resistivity i layer.

The temperature rise of the PIN diode during a single pulse is given by[2]

$$\Delta T = \frac{2q\sqrt{kt}}{\kappa} \left[\frac{1}{\sqrt{\pi}} - \text{ierfc}\left(\frac{a}{2\sqrt{kt}}\right)\right],$$ [5]

where

$k = \kappa/C_v$ = the ratio of thermal conductivity to volumetric specific heat, defined as the thermal diffusivity,
κ = the thermal conductivity of heat sink material,
a = the radius of the diode,
t = pulsewidth,
$q = P_o/A$ = power density absorbed by the diode, and

ierfc = inverse complimentary error function.

For a typical high power PIN diode during a 50-μs pulse, $a \gg \sqrt{kt}$, and the ierfc term is small compared to $1/\sqrt{\pi}$. For a given diode capacitance C,

$$q = \frac{\epsilon P_o}{CW}.$$

Therefore, Eq. [5] becomes

$$\Delta T \cong \frac{2\epsilon P_o \sqrt{t}}{CW\sqrt{C_v \kappa \pi}}. \tag{6}$$

The temperature rise during a single pulse is inversely proportional to the i layer thickness, W. A plot of ΔT as a function of W for $P_o = 300$ W, $C = 2.5$ pF, and with $t = 50$ μs using silicon and with gold as the heat-sink material is shown in Fig. 2. For a 50-μs pulse, the thermal diffusion length, $\sqrt{(\kappa/C)t}$, in silicon is 50 μm. If the main power-absorption region in the silicon is within 25–50 μm of the gold heat sink, the silicon acts as a heat capacitance during the pulse. The curves for gold and silicon shown in Fig. 2 are the low and high limiting values of ΔT at any given value of W. For $W = 100$ μm, the maximum temperature rise during the
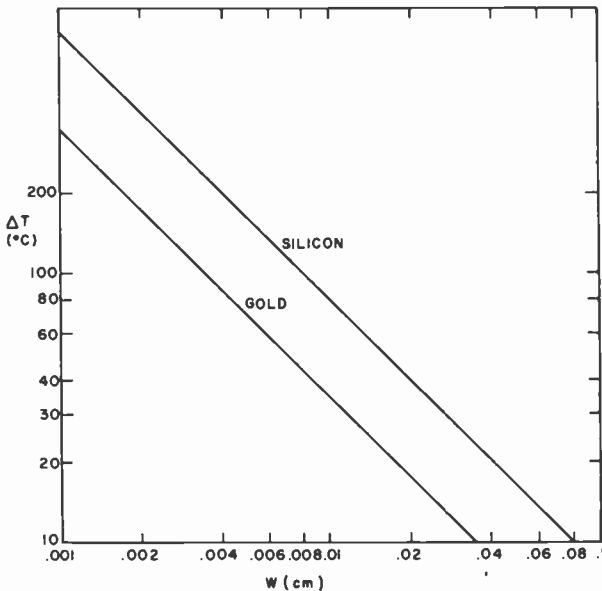

Fig. 2—Temperature increase as a function of i-layer thickness for a 2.5-pF diode with 300-watt power absorption during 50 μs long pulse.

50-μs pulse for absorption of 10% of the 3-kW input is 80°C. For a 0.8% duty cycle, the average temperature rise is insignificant if the diode is properly mounted to a thermal heat sink.

3. Diode Fabrication

Three diode designs are described, each one tailored to a different system's requirements: (1) Single Junction, (2) Moat Configuration, and (3) Stacked Diodes in Series.

3.1 Single Junction Mesa

(a) CVD Process

The PIN diodes are fabricated from n-type high-resistivity bulk-grown ⟨111⟩ silicon wafers with resistivity in the range of 1500 to 5000 ohm-cm. n-type material is used to reduce the chance of type conversion during the high-temperature processing. The wafers are 140 μm thick. Boron and phosphorus are diffused into opposite surfaces of the wafer from doped oxide layers. Diffusion depths of 23 μm for the p^+-n junction and 20 μm for the n^+-n junction were established through two-point spreading-resistance measurements.[3,4]

A trimetal system consisting of chrome–platinum–gold is sputter-deposited onto the silicon contact surfaces. Both surfaces are gold plated to a thickness of 75 μm. A photoresist pattern of dots is formed on the gold surface covering the n^+ layer, and the exposed gold is etched down to the platinum layer. With the thick gold dots acting as a mask, the exposed platinum–chrome is removed by ion-beam milling, and the exposed silicon is removed by an aqueous etchant. The final structure is a mesa with the gold plate serving as a heat sink for the PIN diode. The silicon surface is passivated with a layer of SiO_2 and a layer of Si_3N_4 using low-temperature plasma enhanced deposition,[5] as discussed in Sec. 4. A cured coating of Dow-Corning 648 resin on the mesa prevents air breakdown between the anode and cathode. An electron scanning micrograph of a PIN diode with the plastic coating is shown in Fig. 3.

(b) Ion Implantation Process[22]

The wafers were implanted on a high current Extrion Model 200-1000 ion implanter using a beam current of approximately 1 mA. One side of the wafer received a 1×10^{16}/cm^2 dose of ^{11}B atoms at an implant energy of 150 KeV, and the other side received a 1×10^{16}/cm^2 dose of ^{11}P atoms at an implant energy of 150 KeV. The sources were then driven in for 15 hours at 1200°C to form the n^+ and p^+ contact layers.
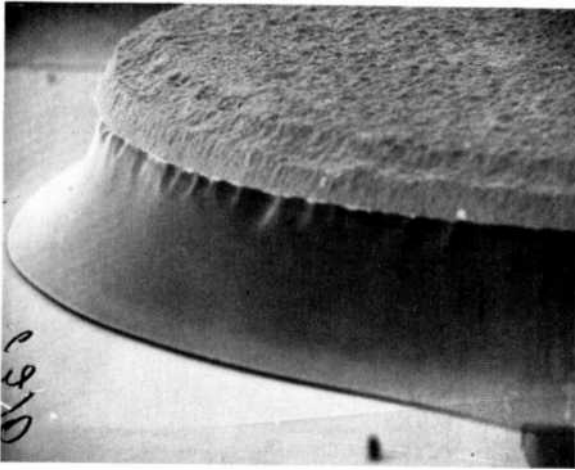
Fig. 3—Electron scanning micrograph of PIN diode with plastic coating.

3.2 Moat Configuration[6]

The moat configuration device, Fig. 4, has been developed to eliminate shadowing of the diode junction by the metal overhang (Fig. 5) during deposition of a sputtered passivation layer.
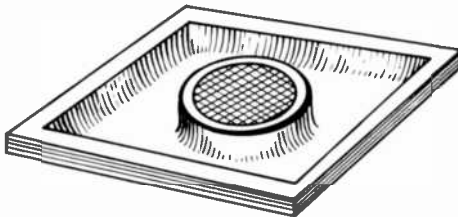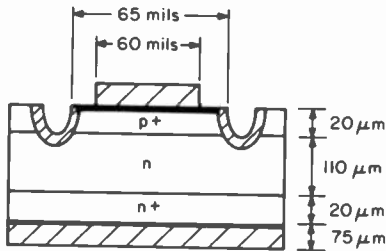
Fig. 4—Moat configuration PIN diode with SiO_2 and Si_3N_4 passivation.
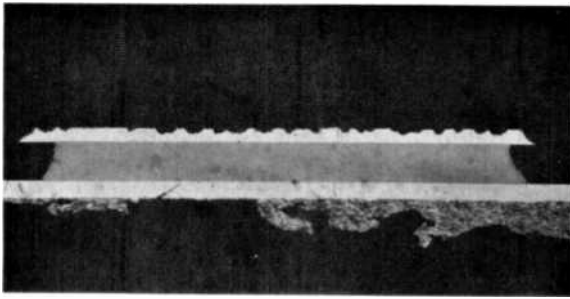
metallization
silicon
metallization

Fig. 5—Mesa structure PIN diode.

The silicon wafer, with an n^+ contact layer on one surface and a p^+ contact layer on the opposite surface, is metallized on both sides (Fig. 6). Contacts are defined on the p^+ side utilizing photoresist techniques, after which moats are etched to produce a mesa structure. The silicon mesa diameter, which is 5 mils larger than the metallization diameter, is also defined by photoresist, and the silicon is etched to a depth of 25
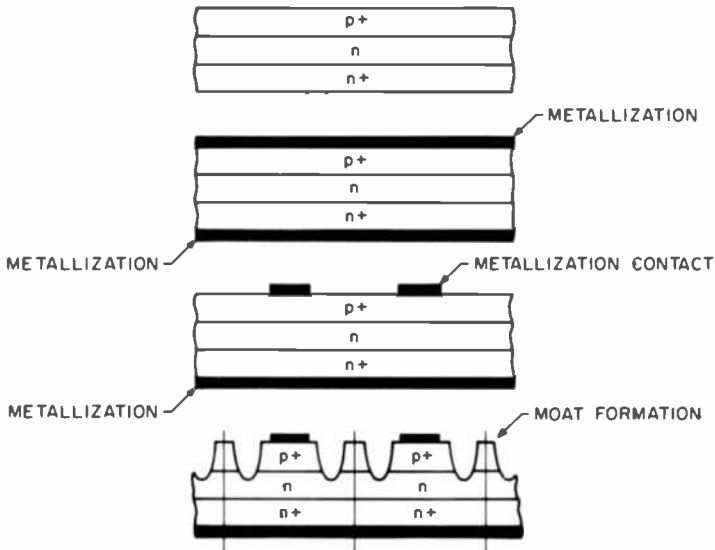
Fig. 6—Moat configuration processing steps.

μm. This procedure eliminates metal overhang. A two-point spreading resistance plot of the p^+n and n^+n region is shown in Fig. 7.

The moat configuration diode, having multilayer passivation with SiO_2 and Si_3N_4 by the sputtering technique,[7,8] withstood stringent environmental tests, as described in Sec. 4. Diodes fabricated by this method are cost-effective compared with the single junction type cited above due to their excellent uniformity and high yield.

3.3 Stacked Diode (Diamond Shape)[9]

(a) *High Power System Requirements*

The performance of phased array radars can be improved by increasing the transmitter output power, which, in turn, requires an improvement in the power-handling capability of the radar elements. One approach to such elements is a high-power microwave switch. Silicon PIN diodes have been used for medium power microwave switching and phase shifting. Power handling capabilities of typically up to 3.5 kW using the PIN diodes have been discussed previously.[4] To achieve higher power handling capability at low cost while maintaining low forward loss, the diode design as well as the fabrication technology had to be developed.
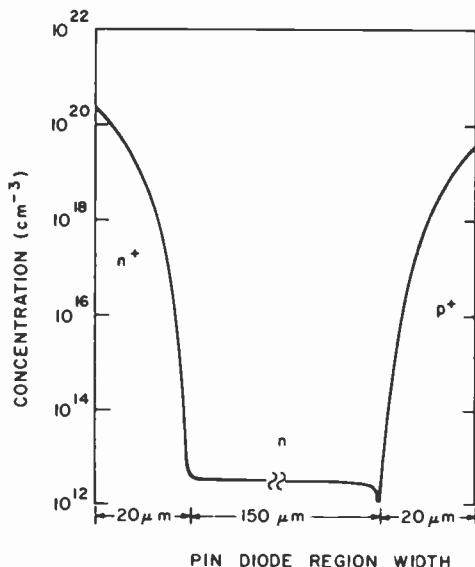
Fig. 7—Two-point spreading resistance plot of p^+n and n^+-n region.

The objective was to develop a silicon PIN diode capable of switching 7 kW of microwave power (14 kW tested in 180° phase shifter utilizing two stacked diodes).

The following section describes in detail a simple method of fabricating PIN diodes having a maximum forward resistance of 0.34 ohms and a minimum breakdown voltage of 1700 V.

(b) Batch Fabrication of Stacked Diodes

Typically, multiple diodes are stacked in series to achieve higher power handling capability. This increase in power occurs because the breakdown voltage of the stacked diodes is essentially equal to the sum of the breakdown voltages of the individual diodes. Furthermore, the diode stack has a lower value of R_f than an equivalent individual diode (provided the contact resistance is low).

In the stacked diode, the total forward resistance is the sum of the forward resistances R_f of the individual diodes in the stack. Since R_f is proportional to the square of the i-layer thickness (Eq. [1]), the R_f of a single diode of i-layer thickness W is greater than the R_f of a stacked diode comprised of N diodes of i-layer thickness W/N by a factor N.

Fig. 8 shows the results obtained from an experimental device having 0.2 pF capacitance and a breakdown voltage of 600 V, when the contact
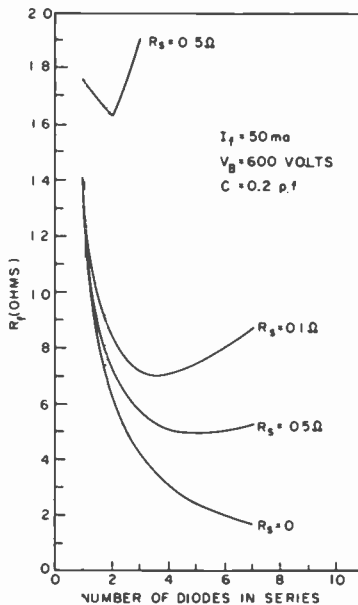
Fig. 8—Forward resistance of stacked diodes as a function of the number of diodes.

GOLD CONTACT
n⁺ DIFFUSED LAYER (25μm)
100 μm THICKNESS
ρ = 2000 Ω-cm
DOW CORNING #648 PASSIVATION
p⁺ DIFFUSED LAYER (25μm)
Au
n⁺
n⁻
p⁺
Au

DOUBLE STACKED PIN DIODE
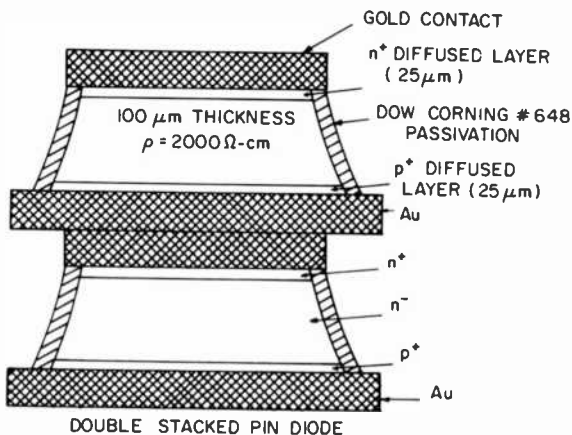
Fig. 9—Stacking configuration for diodes attached in series.

resistance is zero. Techniques for fabricating both individual and stacked diodes are known and used in the semiconductor industry. However, these existing techniques create difficulties when adapted to high-power low-loss applications. Producing a stacked configuration from individual diodes (Fig. 9) requires that a bonding operation be performed. This creates the need for a handling procedure to manipulate the small diodes, a potentially costly and inefficient operation.

To avoid the handling problems associated with a bonding operation performed on individual diodes, processes have been developed that include stacking the devices while they are in wafer form (Fig. 10). These techniques generally comprise the steps of semiconductor wafer doping

Au CONTACT
n⁺ DIFFUSED LAYER (25μm)
100 μm THICKNESS
ρ = 2000 Ω-cm
DOW CORNING #648 PASSIVATION
p⁺ DIFFUSED LAYER (25μm)
Au
n⁺
n⁻
p⁺
Au

DOUBLE-STACKED PIN DIODE
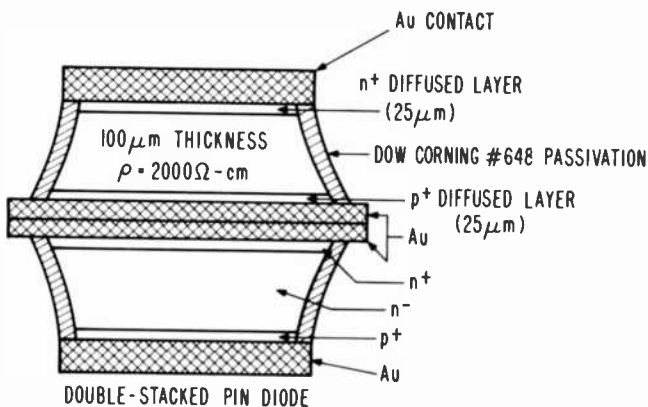
Fig. 10—Stacking configuration for diodes attached while in wafer form.

and metallization, laminating the desired number of wafers together, pattern generating the diodes on the exposed wafer surfaces, dicing the wafer into laminated stacks, and performing a finishing operation on the diced surfaces of the stacks. The laminated wafer is mechanically diced, since the laminations typically include layers of metal as well as of semiconductor material. The mechanical cutting operation, however, causes damage to the cut semiconductor surfaces, which necessitates etching the surface. However, in the case of stacks made up of two diodes, which are used in high-power, low-loss applications, this manufacturing technique is unsatisfactory. These diodes use high resistivity i-layer material (1500–5000 ohm-cm), and the damage caused to the semiconductor surfaces during the cutting operation cannot be adequately removed by subsequent chemical surface etching.

An efficient method for fabricating stacked diodes comprising two diodes was developed. The diamond-shaped devices, consisting of back-to-back mesas connected in series, are processed as follows (Figs. 11 and 12):

(1) The diffused wafers are metallized with Cr-Au and soldered together.

(2) After additional gold plating, a photoresist pattern of dots defining the diodes is made on both sides of the combined wafers.
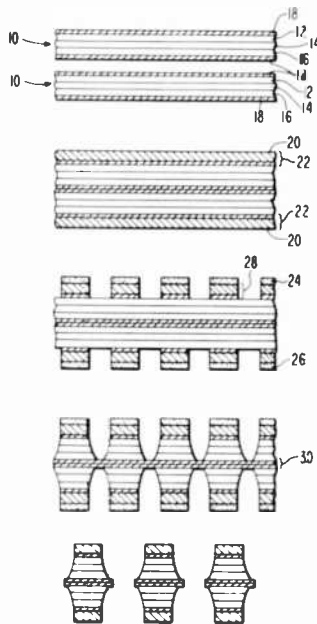
Fig. 11—Fabrication steps for mesa diodes stacked back-to-back to form diamond shaped devices.

Fig. 12—Back-to-back mesa diodes on wafer (back side of wafer can be seen in mirror).

(3) Au and Cr etchings are performed.
(4) Silicon etchings follow.
(5) The wafer is then diced into individual diodes.

4. Diode Passivation and Stress Tests

The PIN diodes passivated with SiO_2 and Si_3N_4 have been stress tested with (a) high humidity, (b) temperature cycling, and (c) thermal shock.

(a) Moisture Resistance Test
Diodes were subjected to 10 days of continuous cycles in a humidity chamber at 90–98% relative humidity and temperature varying between -10 and $65°C$. The moisture resistance test evaluates the resistance of the passivation to high humidity and heat in an accelerated manner. Most degradation effects result from surface wetting and absorption of water vapor. These effects will cause changes in the electrical properties of poorly passivated junction mesa diodes. This test differs from the steady-state humidity test, and derives its added stress in its employment of temperature cycling, which provides alternate periods of condensation and drying. Increased effectiveness of the test is also obtained by the use of a higher temperature, which intensifies the effects of humidity.

In addition, the test also includes a low temperature sub-cycle to reveal any cracks in diode passivation. At the end of this test, measurements of electrical characteristics, such as voltage breakdown and power handling capabilities, were performed, and these measurements showed no evidence of deterioration of these properties.

(b) Temperature Cycling
This test determines the diode's resistance to exposures to extremes of high and low temperatures during cycling, and it assesses the effect of alternate exposures at these extremes. Permanent changes in operating characteristics and physical damage produced during temperature cycling result principally from variations in dimensions and other physical properties. The test was conducted for 15 cycles, each cycle between -65 and $+200°C$. External visual examination revealed no change in diode configuration or passivation. In addition, no change in leakage current was observed.

(c) Thermal Shock
The passivated device was cycled fifteen times between the extremes of -65 and $150°C$. Devices were immersed in, and remained in intimate contact with suitable liquids at the temperature of $-65°C$ for 5 min and then were transferred to a liquid maintained at $150°C$ for 5 min. No physical or electrical degradation was observed. In addition, the diodes were subjected to a temperature-bias test (blocking test) in which they were reverse-biased up to 400 V at various temperatures between 25 and $130°C$ in air. The diodes passivated by the sputtering technique withstood all tests, except the blocking test, during which they developed excess reverse-biased leakage current and eventually burned out. Diodes from the same batch, which were passivated by plasma-enhanced silicon nitride deposition (Si_3N_4 thickness $\cong 1.2 \, \mu m$) were subjected to identical tests without failing. Also, these diodes successfully supported reverse biases of 400 V at $175°C$ for 160 h.

(d) Passivation
The diode passivation by sputtering SiO_2 and Si_3N_4 was inadequate, since the junction was shadowed by the overhanging metallization. Passivation by plasma deposition, on the other hand, permits a uniform nitride deposition over the silicon surface. Upon removal of the metal overhang or fabrication of the diodes in a moat configuration, in which there is no metal overhang, the diodes survived all tests, whether passivated by sputtering or by the plasma technique.

We have also compared the passivation by plasma-deposition of 1.2-μm silicon nitride with 1.2-μm silicon oxynitride yielding an average

composition $Si_{0.42}O_{0.42}N_{0.16}$.[10] Silicon oxynitride (except as a Na barrier) is superior. Ten diodes (80 mil in diameter) passivated with silicon oxynitride were subjected to a blocking test at 600 V reverse bias and at a maximum temperature of 165°C for a total of 765 hours without any failure. Not only did the diodes withstand the test, but some reduction in leakage current was observed as the test proceeded. The average leakage current under the above conditions was 60 μA, which is an order of magnitude less than that obtained during a similar test on PIN diodes passivated with silicon nitride.

As a barrier to the sodium ions, silicon oxynitride was tested by the Environmental Analysis Laboratories in California. In this test, experiments were performed to determine the diffusion of sodium into a layer of silicon oxynitride. Sodium-22 radioisotope was deposited on the silicon oxynitride surface. The sample was heated to about 600° ± 10°C to drive the Na ion into the oxynitride. The depth of Na penetration was determined by step etch autoradiography and gross beta count.[11] Final results showed the oxynitride to be an unsatisfactory barrier. A possible solution for low leakage current and high Na barrier would be to passivate first with 1.2 μm of silicon oxynitride to maintain uniform stress-free passivation and then to cover the oxynitride with 500 Å of Si_3N_4 which would serve as a sodium ion barrier.[10]

5. Diode Performance

In this section we describe results obtained from typical diodes in each of the geometrical configurations discussed—(1) single-junction mesa diode, (2) moat configuration diode, and (3) stacked diodes.

5.1 Single-Junction Mesa Diode

(a) CVD Process

The finished diode with an i-layer thickness of 100 μm has a depletion capacitance of 3 pF and a breakdown potential of 1000 V (Fig. 13). The stored carrier lifetime (as measured on a type S Tetronix) on a 60-mil-diameter diode is 15 μs. A detailed analysis of storage time versus diode diameter is discussed further on. The high frequency small-signal performance of the diode was measured in a resonant cavity at ultra high frequency (500–1000 MHz).

The coaxial microwave cavity[12] used in the measurement is shown in Fig. 14. With the diode replaced by a short, a reference unloaded Q_o of the cavity including the fixed capacitor is measured using a network analyzer reflection unit. To obtain the resistance of the diode (unpackaged), the measured Q_m and resonant frequency of the diode loaded cavity are used:
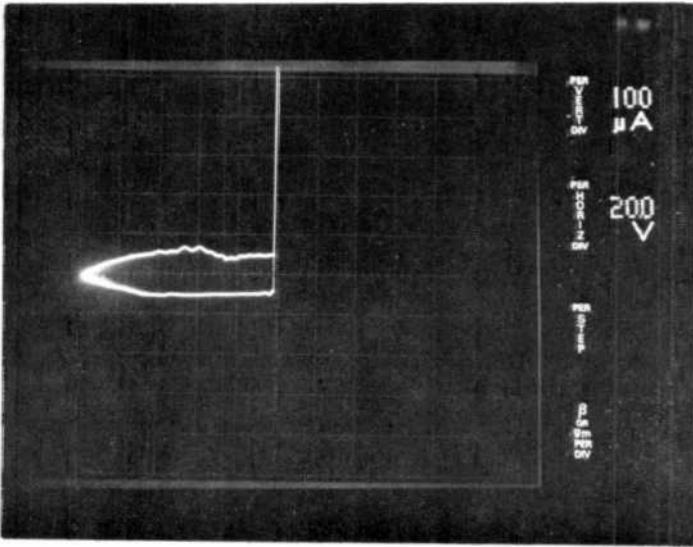
Fig. 13—Current–voltage characteristic of typical PIN diode.

$$R_f = \frac{1}{2\pi fc}\left(\frac{1}{Q_m} - \frac{1}{Q_o}\right). \tag{7}$$

The forward series resistance, R_f, of a typical single-junction mesa diode with an i-layer thickness of 100 μm at $I_f = 50$ mA is 0.24 ohm.

The power handling ability per diode as measured in a 180° microstrip hybrid type phase shifter, reverse biased to 40 V, and forward biased to
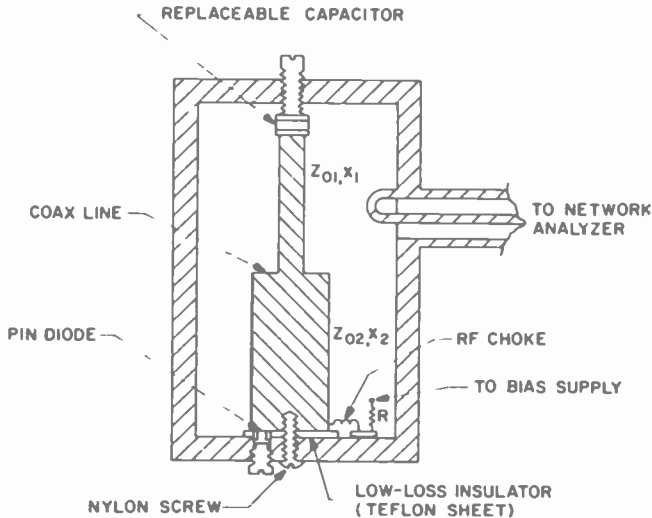
Fig. 14—Microwave cavity for forward-biased resistance measurements of diodes.

Parameter	Measured Value
Capacitance	2.5–3 pF
Diameter	0.060 inch
Breakdown Voltage	1000 V
Forward Resistance at 50 mA	0.24 ohm
Stored Carrier Lifetime	15 μs
Q at 40 V Reverse Bias at 900 MHz	800

50–100 mA is typically 3.5 kW.[4] The breakdown voltage is 1000 V. A summary of the diode parameters is given in Table 1.

(b) Ion Implantation

The measurements performed on the diode with ion implanted contacts are similar to the ones above. The obvious advantage of ion implantation is the excellent uniformity across the wafer and the good reproducibility from wafer to wafer.

5.2 Moat Configuration Diode

The electrical characteristics of the moat configuration PIN diodes are similar to those described before, with the exception that a breakdown voltage of 800 V was obtained with the negative bevel mesa as contrasted with 1000 V for diodes previously described (positive bevel), both having the same i-layer thickness.

A bevel angle is called positive when the lateral extension of the p$^+$ layer is larger than it is at the p$^+$n junction, otherwise the angle is called negative. In the case of negative bevel, a decrease in the width of the space-charge region occurs at the surface, and hence an increase in the maximum field results. According to Cornu's[16] analysis, the high-voltage breakdown occurs beneath the bevelled surface at the point of maximum electric field. For positive bevel angles, the space-charge region in the vicinity of the surface expands on the low-doped side of the p$^+$n junction more than it retracts on the highly doped side. This expansion of the surface depletion region results in a reduction of the maximum field on the surface with respect to the maximum field in the bulk.

5.3 Stacked Diode

Phase shifters employing two stacked diodes (see Figs. 10 and 12, except that here the i-layer thickness is 85 μm) have been tested successfully up to a peak power of 14 kW with 0.2% duty cycle and 50-μs pulsewidth. The average insertion loss of the 180°-bit phase shifter utilizing the stacked configuration was 0.64 dB. This loss is about 20% higher than

Table 2—Average Diode Insertion Losses for Different i-Layer Thicknesses (Measured in 180°-bit Phase Shifter)

Diode Configuration	W (μm)	Loss (dB)
Single Diode	56	0.38
Single Diode	112	0.55
Stacked Diode	160 (80/80)	0.58
Stacked Diode	180 (90/90)	0.64
Stacked Diode	200 (100/100)	0.70
Stacked Diode	280 (140/140)	0.76

Table 3—Performance of Double Stacked Diode

Diode Parameter	Value
Capacitance	3.0 pF
Breakdown Potential	1700–1900 V
Forward Resistance at $I_F = 50$ mA	0.3–0.34 ohm
Stored Carrier Lifetime in i region	25 μs
Q at 60 V Reverse Bias and $f = 3$ GHz	>100
Peak Power for 50 μs Pulse in 180° Phase Shifter for Reverse Bias of 60 V	7 kW

that of a 180°-bit phase shifter with a 7 kW capability that utilizes two single diodes having an i layer 100 μm thick. Table 2 shows the average insertion loss measured on several 180° integrated phase shifters together with the i-layer thickness of the single or stacked diodes used in each phase shifter. Table 3 summarizes the performance of the double stacked PIN diodes.

6. Storage-Time Variations in Silicon PIN Diode (p^+-n-n^+)

An important parameter of the PIN diode is the decay time, τ_e, of the injected, stored charge. For a given forward dc current, I_f, τ_e determines the average stored charge, N,

$$N = I_f \tau_e. \tag{8}$$

The forward resistance, R_f, is in turn inversely proportional to N; hence, the larger the τ_e, the smaller the R_f (see Eq. [1]).

Our studies[13] have shown that τ_e depends on at least three recombination mechanisms: (1) bulk recombination described by the bulk recombination lifetime, τ; (2) surface recombination at the n-layer sidewalls, which in this work is characterized by an extremely large recombination velocity; and (3) an interfacial recombination at the n-n^+ interface, which is described by an interfacial recombination velocity, $S_{n\text{-}n^+}$. The bulk and interfacial recombination depend on the forward drive current, or, more fundamentally, on the average injected charge density, $N/[W\pi a^2]$. The surface recombination is extremely large in

all cases. Surface recombination velocities are considered large when they are much greater than D/a, where D is the diffusion constant for stored charge and a is the diode radius.

The stored-charge lifetime is easily found from a measurement of the conventional reverse-recovery storage time, t_s.[14] The measurement setup is shown schematically in Fig. 15, along with a typical diode response. A forward current pulse, I_f, passes through the diode until a steady state exists. The current is then quickly reversed to a value $I_r = I_f$. The interval, throughout which the stored charge supports I_r, is the storage time t_s. Beyond t_s, the reverse current quickly decays to its reverse saturation level, which in our case is many orders of magnitude below I_r. The variations in t_s were measured over a wide range of diode radii and forward current levels.

The storage time is simply related to the injected charge decay time:[15]

$$t_s/\tau_e = \ln\left[1 + (I_f/I_r)\right]. \qquad [9]$$

Since $I_f = I_r$ in all of our experiments,

$$\tau_e \cong 1.4\, t_s.$$

The PIN diodes have chemically etched n-layer sidewalls that act as very high recombination surfaces. Essentially, every injected carrier that reaches the surface recombines there. Under such circumstances, if we assume that the injected charge density is uniform in the axial direction, τ_e depends on the diode radius a in the following way:

$$1/\tau_e = (1/\tau_1) + (\alpha_1{}^2 D/a^2), \qquad [10]$$

where α_1 is the first zero of the zero-order Bessel function ($\alpha_1 \approx 2.405$)
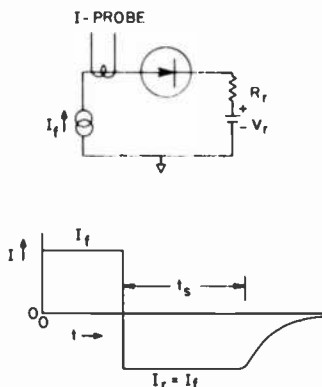
Fig. 15—Schematic of setup to determine stored-charge lifetime by measurement of reverse-recovery storage time, t_s.

and τ_1 is the decay time for injected charge in the absence of recombination at the sidewalls. τ_1 depends on τ and $S_{n\text{-}n^+}$. The term $\alpha_1{}^2 D/a^2$ embodies the effects of the high surface recombination velocity on the stored charge lifetime.

Fig. 16 is a plot of $1/\tau_e$ versus a^{-2} for a set of diodes with radii ranging from 0.05 to 0.95 cm. These data were taken at low drive levels where t_s is independent of I_f. The slope of a linear fit to the data gives a value of $D = 26$ cm^2/s and a value of $\tau_1 = 280$ μs for the y-axis intercept. The linearity of the data substantiates the assumption that the surface recombination velocity is very large. The high recombination rate at the diode surfaces greatly reduces the stored charge lifetime. Note that if $\tau_1 = \infty$, a 0.05-cm-radius diode would have $\tau_e = 17$ μs.

This reduction in τ_e by surface recombination is seen more clearly in Fig. 17, where τ_e is plotted against d, giving a typical S-shaped curve. At moderate diode diameters of 0.1 to 0.2 cm, τ_e is dominated by surface recombination. Only when d approaches 2.0 cm does τ_e approach the limit set by internal recombination. Physically, the effect of the diameter on τ_e can be understood as follows. With high internal lifetimes, the injected carriers can diffuse relatively long distances to the surfaces of the n-layer sidewalls where they quickly recombine.

To reduce surface recombination, diodes can be made large in diam-
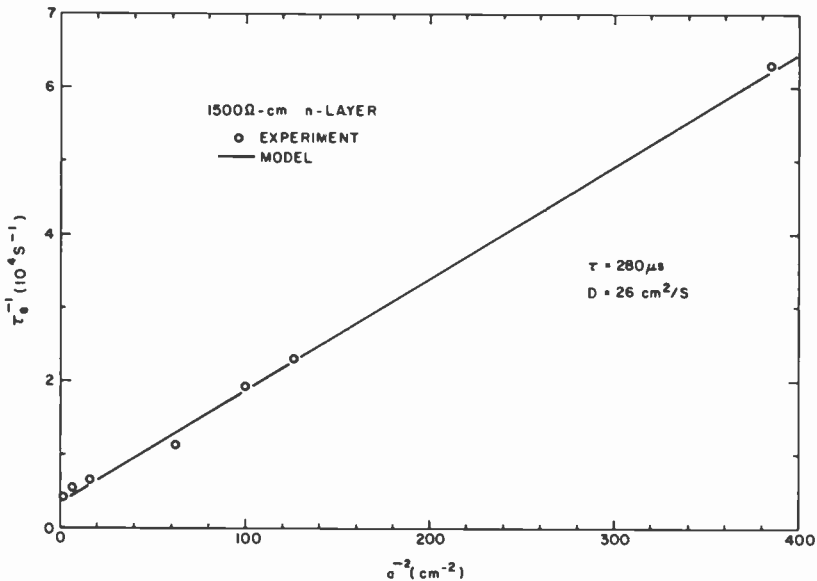
Fig. 16—Plot of $1/\tau_e$ versus a^{-2} for a set of diodes with radii from 0.05 to 0.95 cm.
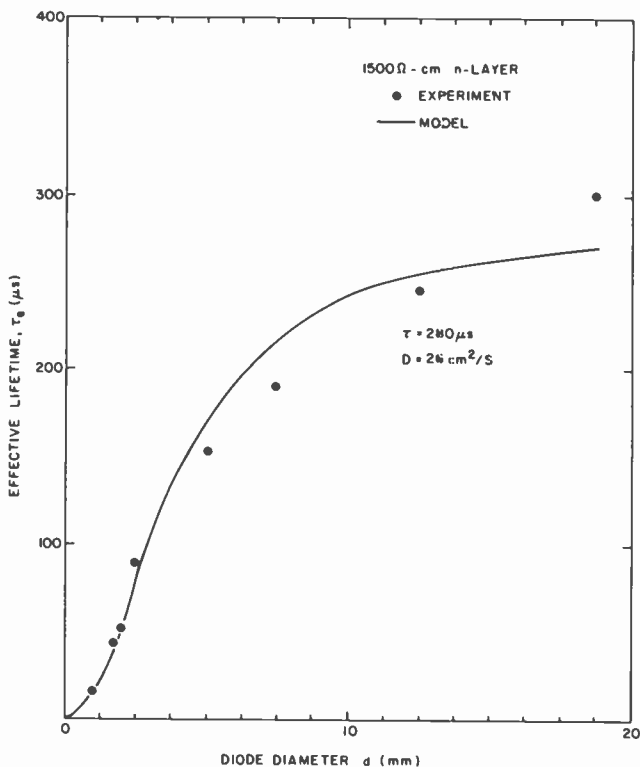
Fig. 17—Plot of effective lifetime versus diode diameter showing effect of surface recombination.

eter, but since diode capacitance scales as the diameter squared, such an increase in diameter may not be desirable. The alternative is to treat the n-layer surface so as to reduce recombination there. To date, no such successful surface treatment exists.

The effects of increased forward drive on the storage time are shown in Fig. 18(a) and (b). In part (a), t_s is plotted against forward current density $J_f = I_f/(\pi a^2)$ for a set of diodes with n layers of 1500 ohm-cm, 150 μm thick. At low current densities, t_s is constant, and it increases with increasing diameter for the reasons discussed above. As the forward drive increases, t_s reaches an upper bound independently of diode diameter. Fig. 18(b) shows the same data plotted against $\overline{N}$, the average injected charge density:

$$\overline{N} = I_f \tau_e/(W \pi a^2).$$

In the figure, t_s behaves similarly, but the upper limit at high values of
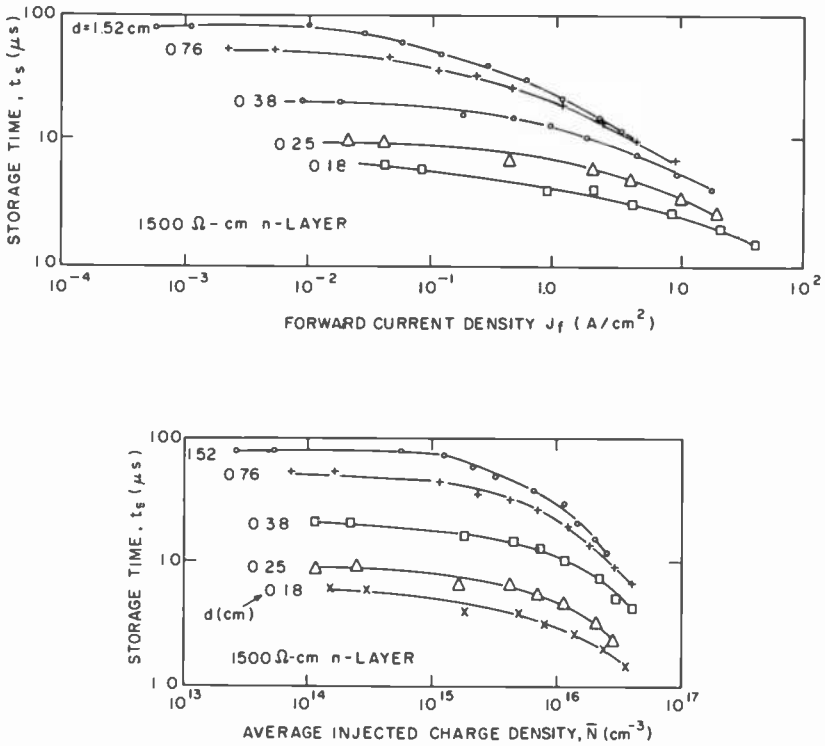
Fig. 18—Effect on storage time (a) of increased forward drive and (b) of average injected charge density.

$\overline{N}$ is less pronounced. From an analysis of the variation of t_s with a at given values of $\overline{N}$, the internal time constant τ_1 can be separated into τ and $S_{n\text{-}n^+}$. As $\overline{N}$ increases, τ decreases and $S_{n\text{-}n^+}$ increases, both of which decrease τ_1.

The change in τ_e with injected charge affects the forward resistance R_f at microwave frequencies:

$$R_f = W^2/[I_f \tau_e (\mu_n + \mu_p)] \text{ for } \omega\tau_e \gg 1,$$

where $(\mu_n + \mu_p)$ are the average mobilities of injected electrons and holes, which do not change greatly with increasing forward drive.[4]

If τ_e were constant, R_f would decrease as I_f^{-1}; but owing to the decrease in τ_e with increasing forward current, R_f decreases less rapidly. Fig. 19 shows the measured and the predicted values of R_f. The predicted values take into account the measured decreasing value of τ_e with increasing I_f. The agreement is good, and the somewhat lower predicted values for R_f may arise from a neglect of contact, n+-, and p+-layer resistances.
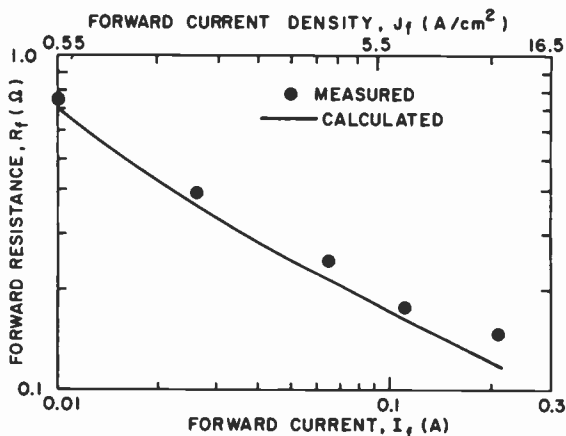
Fig. 19—Measured and predicted values of forward resistance.

The results emphasize the importance of knowing τ_e as a function of I_f, especially under conditions of high forward drive. R_f decreases less rapidly than I_f^{-1} because the total injected charge $Q = I_f\tau_e$ increases less rapidly than I_f owing to the decrease in τ_e at high injection levels.

The conclusion is that τ_e changes with injection level and with diode radius, and these variations must be considered when predicting diode performance. A major improvement in stored charge lifetime will come from the reduction of recombination at the n-layer sidewalls.

7. Neutron Damage in PIN Diodes[17]

The purpose of the study described in this section was to determine the fluence required for the PIN diodes to cause the insertion losses of the phased array elements to exceed the system specifications. Radiation damage measurements were made on experimental PIN diodes, and the results enabled a determination of the lifetime damage constant K_τ for 14 MeV neutrons, reactor neutrons, and Cobalt-60 gamma rays. The insertion loss measurements on the diodes were extrapolated to higher fluence levels in order to develop radiation-hardened diode designs for maximum neutron hardness compatible with radar system specifications.

7.1 Experiment

Experimental diodes (56 diodes of various intrinsic widths and lifetime) and six samples of commercially available units were exposed to 14 MeV neutrons supplied by a D-T neutron generator. Manufacturers' processing data for the commercial diodes were not available. These diodes' intrinsic region width, W, was determined by the spreading-resistance measurement. They were enclosed in a pill-type package; the experimental diodes were not packaged.

It should be noted that the experimental diodes, as opposed to the commercial diodes, are of the Mesa type described previously.

A Tektronix S-type diode recovery unit was used to measure stored-charge lifetime; however, with the decrease of lifetime to about one microsecond, this measurement technique is no longer applicable. For lifetime measurements of samples with $\tau < 1$ μs, the Refined Step-Recovery Technique of R. H. Dean and C. J. Neuse[19] was used; it permits measurements of lifetime as low as 1 ns. To normalize the results of both techniques, measurements of samples were compared in the 1 to 7 μs range and a normalization factor was determined. This factor was used to adjust the lifetime values only in the case of the experimental diodes exposed to the higher reactor neutron fluences.

Insertion loss measurements were made using a HP8540A network analyzer at a frequency of 3 to 3.5 GHz. The increase in power loss with irradiation could cause catastrophic failure of the diodes should the power dissipation exceed the limit. System requirements have limited the value of insertion-loss increase and, consequently, the allowable neutron or gamma exposure. The power-handling capabilities of some of the experimental diodes were determined after irradiation.

7.2 Results

The degradation of lifetime in the experimental diodes is plotted in Fig. 20 for all the samples bombarded by 14 MeV neutrons. It should be noted that regardless of the initial values of lifetime, all of the curves converge as the neutron fluence increases. A lifetime damage constant can be computed for any one of the samples and for different ranges of neutron fluence; however, the value of $K_\tau = 3.8 \times 10^{-7}$ cm^2/n-s noted in Fig. 20 is a reasonable fit of all three curves through the usual lifetime equation, with initial lifetimes ranging from 2.5 to 20 μs and corresponding intrinsic widths from 25 (experimental) to 152 μm (commercial).

Lifetime measurements made on six samples of the commercial diode exposed to 14-MeV neutrons are also plotted in Fig. 20 (dashed curve). This curve could also be fitted with the same damage constant K_τ as the
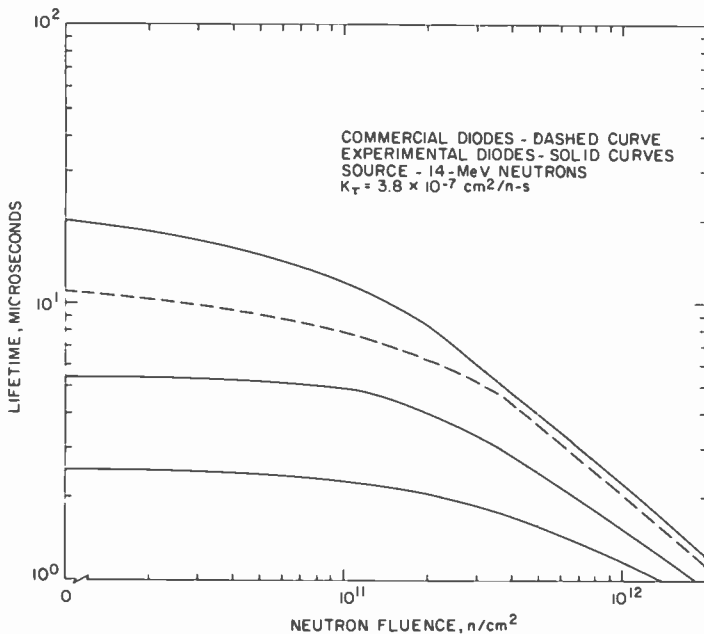
Fig. 20—Degradation of lifetime in experimental and commercial diodes bombarded by 14-MeV neutrons.

Table 4—Increase in Insertion Loss of Microwave Circuits Versus 14-MeV Neutron Fluences

$\phi(n/cm^2)$	45° Bit (dB)	90° Bit (dB)	180° Bit (dB)
6.43×10^{10}	0	0	0.05
4.64×10^{11}	0.05	0.14	0.15
8.95×10^{11}	0.11	0.32	0.28
1.46×10^{12}	0.125	0.59	0.6

experimental diodes. The six commercial devices were removed from the microwave fixture after the final exposure (1.46×10^{12} n/cm²) and after power losses were measured. The diode lifetimes were found to range from 1.2 to 1.5 μs, which agrees with the values extrapolated from the curve for the commercial diodes in Fig. 20. The microwave insertion losses were measured on the three phase shifters. Table 4 contains the increased losses measured on the 45°, 90°, and 180° bits versus the neutron fluence. The 45° bit circuit was the least sensitive. This is the result of a much lower rf current flowing in the diodes of the 45° bit for the conducting states.

The increase in insertion loss (Table 5) after bombardment by 14-MeV

Table 5—Average Insertion Losses for Experimental Diodes Exposed to Neutrons

Samples W	Unirra-diated Loss	Fluence	Irra-diated Loss	Increase Loss
56 μm	0.38 dB	1.39×10^{12} n/cm² (14-MeV)	0.39 dB	Not Detectable
	0.38	1.26×10^{13} (reactor)	1.0	0.66 dB
	0.38	4.4×10^{13} (reactor)	1.6	1.2
112	0.55	1.39×10^{12} (14-MeV)	0.6	0.06*

* Approximately within the accuracy of the measurement.

neutrons was small for these experimental diodes compared with that of the commercial diodes. After the final exposure, the experimental diodes fabricated with intrinsic regions of 56 μm width were subjected to a power test. These diodes were capable of operating at up to 5 kW of rf power in the forward direction, to 4.5 kW of power in the reverse direction, and to 1.5 kW in the zero-bias operating condition.
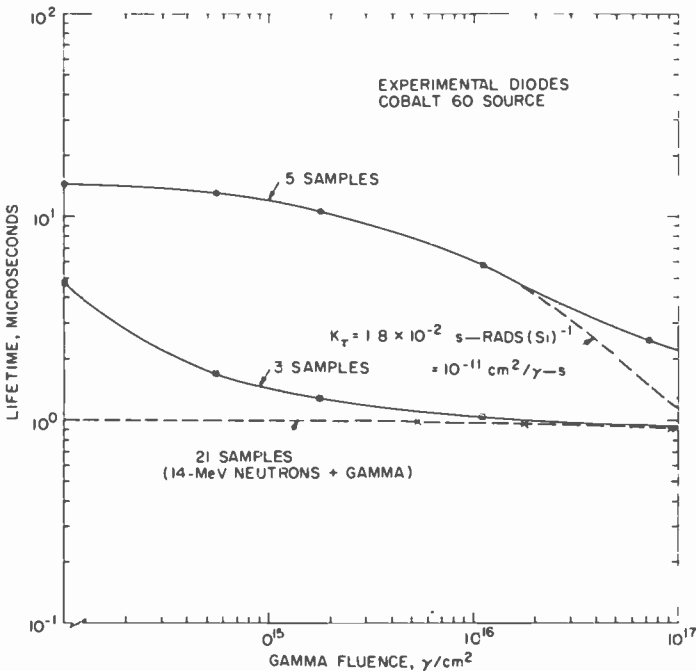
Fig. 21—Stored charge lifetimes as a function of gamma irradiation and of 14-MeV-neutron plus gamma irradiation.

Figs. 21 and 22 are plots of stored-charge lifetime as a function of Cobalt-60 gamma and reactor neutron fluences. The 14-MeV neutron-irradiated samples were irradiated by ^{60}Co gammas after completion of the neutron tests. Note that the gamma-irradiated or 14-MeV neutron-plus-gamma-irradiated samples clearly exhibit a practical limiting value of lifetime of 1 μs for these samples exposed to neutrons plus 10^8 rads of gammas. These measurements indicated that a dose of 10^8 rads was not sufficient to degrade the neutron-exposed samples significantly beyond the ≈ 1 μs lifetime value. A further check of this limiting value for gammas was made by irradiating five samples with initial lifetimes of 9 μs to a dose of 10^8 rads (Si). The resultant lifetimes varied from 0.94 μs to 1.1 μs, thus confirming this value. In contrast to this effect, the lifetime of the reactor neutron irradiated samples decreased to 175 ns after exposure to a maximum fluence. Continuation of the 14-MeV irradiations to a comparable maximum fluence would have reduced the lifetimes to similar values measured for exposure to 1-MeV neutrons.
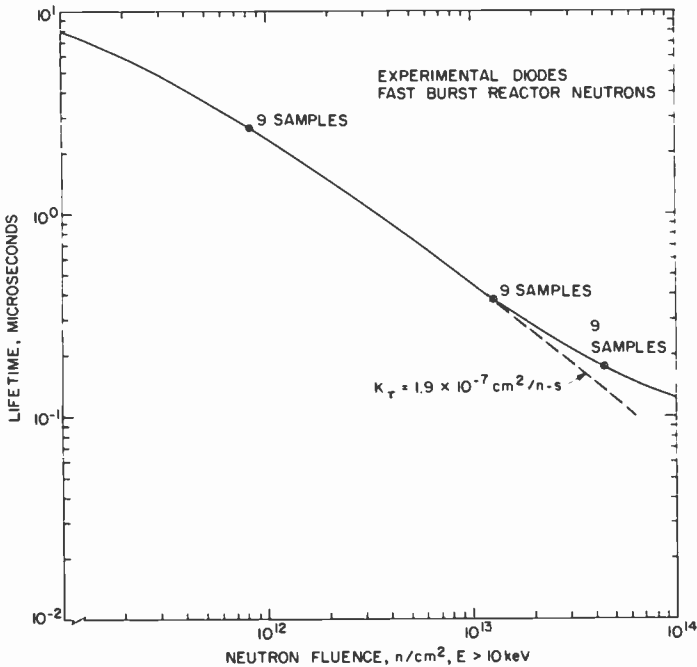
Fig. 22—Effect of reactor neutron fluence on lifetime.
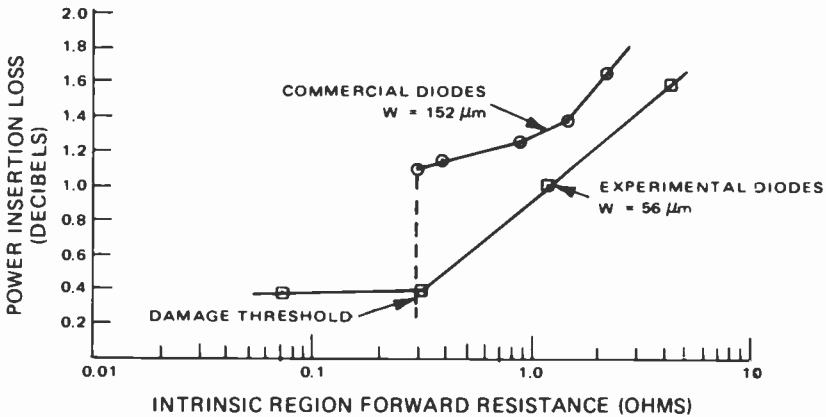
Fig. 23—Diode insertion loss versus forward resistance of intrinsic region as calculated from degrading lifetime.

7.3 Discussion

The forward resistance of the intrinsic region R_F varies with the square of the width of the intrinsic region W, which in turn is dependent on the impurity carrier density in the i region, and R_F varies inversely with the lifetime. The dominant damage effect was the decrease of lifetime with neutron or gamma bombardment, which increases R_F and therefore the insertion loss.[18]

Fig. 23 is a plot of the calculated values of R_F versus insertion loss for the commercial and experimental diodes (i.e., $W = 56\,\mu m$). Comparison of the insertion loss data of Tables 4 and 5 indicates that the experimental diodes are harder than the commercial ones considering the fluence required to cause a certain power loss. The curves of Fig. 23 indicate that the basic difference in the two types of diodes is due predominantly to the intrinsic width, W, and secondarily to the initial lifetime. The experimental diodes are characterized by needing a greater neutron fluence threshold for the insertion loss to increase. The threshold depends approximately on the value of $4D\tau_e$ relative to W^2. When these values are comparable, the insertion loss increases sharply. The threshold value of R_F is approximately 0.3 ohm for both diode types as shown in Fig. 23. Other possible differences between the diodes are the processing, the Mesa configuration of the experimental diodes, and the packaging. The specific differences in the processing are not known; however, the processing of the experimental diodes was carried out in a very clean and carefully controlled system. For example, experimental diodes have been processed with $W = 122\,\mu m$ and stored-carrier lifetime of as much as $20\,\mu s$, as compared with the $152\,\mu m$ and $11\,\mu s$ of commercial diodes. It

Table 6—Lifetime Damage Constants for PIN Diodes Exposed to Neutrons and Gammas

K_τ (14-MeV) cm²/n-s	3.8×10^{-7}
K_τ (1-MeV) cm²/n-s	1.9×10^{-7}
K_τ (^{60}Co Gammas) cm²/γ-s	1×10^{-11}

is important to maintain a long lifetime as W is reduced so that the threshold value of fluence remains high.

7.4 Conclusions—Radiation Hardening

Table 6 contains a summary of the damage constants for all types of diodes and radiation. It should be noted that these constants were determined from the linear portion of the damage curves; consequently, using them to predict damage for the higher fluences will overestimate the lifetime decreases and insertion loss increases.

It can be concluded from these results that a lifetime damage constant $K_\tau = 3.8 \times 10^{-7}$ cm²/n-s for 14-MeV neutrons applies to a wide range of PIN diodes. These diodes have intrinsic regions ranging from 25 to 152 μm and stored-carrier lifetimes ranging from 2.5 to 20 μs. The corresponding 1-MeV neutron and gamma damage constants were not measured on as many different samples as were those of the 14-MeV neutron; thus the universality of the damage constants may not be the same. The 14-MeV to 1-MeV neutron damage ratio is 2, and the ratio of neutron to gamma damage is about 10^4.

The measurement of microwave insertion losses after neutron exposure, which is the practical engineering parameter, suggests that reduction of intrinsic region width to a value of about 56 μm and lifetime of 6 μs in a PIN diode fabricated in the manner described herein will produce a hardened device. Further reduction of W will lead to increased hardness, but with an attendant reduction in peak power handling capability.

The radiation hardness of the stacked diode (i.e., two diodes in series) will be greater than the level of the single diode with the same total intrinsic width, W. This conclusion assumes that the lifetime τ is not significantly lower in the two diodes of a stack compared with the value of a single diode.

8. Conclusions—Diode Considerations

We have established pertinent guidelines for the design of high power, low loss PIN diodes. Unique and simple processing techniques were

developed that resulted in diodes meeting all specification requirements as discussed. Basic understanding of diode parameters was instrumental in the choice of diode configuration. In addition, radiation experiments led to a set of curves depicting device parameters necessary for the design of high power PIN diodes which are resistant to neutron radiation. The diodes' parameters and the results were obtained from unpackaged diodes in chip form. Nevertheless, the diodes were passivated and reliability tests were performed showing that they need not be packaged for use in systems. These tests have established the feasibility of utilizing PIN diodes in chip form, a great advantage to the circuit designer.

9. Circuit Design[20]

9.1 The Case for the Hybrid Coupled Bit

The phase shifter circuit selection is based on cost, power handling, and loss in that order. The switched line phaser can be made to handle the power but needs 12 diodes to complete three bits. Cost is proportional to the number of diodes. The loaded line phaser requires as many as 14 diodes. The hybrid coupled-diode phase shifter has good power handling capability and is cost effective with only six diodes.

Since the diode power-handling capability is dominated by the zero-bias survival, a comparison between the switched line, loaded line, and hybrid coupled diode phasers yielded a near constant for all three types.

The diode losses for a 3-bit phase shifter have also been shown to be the lowest for the hybrid-coupled type.[21] Table 7 is a comparison of diode losses. It shows that for a diode Q of 100, the diode losses for the hybrid coupled circuit are only 0.6 dB. This takes into account the higher loaded circuit Q of the hybrid-coupled circuit.

Circuit losses for this microstrip design are about equal to the diode losses.

Table 7—Comparison of Diode Losses for 3-Bit Phaser

Type	Switched Line	Loaded Line	Hybrid Coupled
Circuit Q	1	1.2	2
Diode	Diode Losses (dB)		
Q-50	2.2	2.0	1.25
Q-100	1.1	1.0	0.6
Q-200	0.5	0.5	0.3

9.2 Design Parameters

The best way to characterize a microwave PIN diode is in a fixture (see Fig. 24) that simulates the way it is used—the same substrate, the same interconnection, and the same mounting. This approach to characterization eliminates the guesses about the correct equivalent circuits for the diode. The resulting circuit parameters are plotted in a very useful form on the Smith Chart in Fig. 25. It shows that in a 50-ohm system the diode itself produces a differential phase shift of 50° at the low frequency end of the band and a 43° phase shift at the high frequency end.

To produce an even larger phase change using the same diode, transformation is introduced between the diode and the hybrid. A simple relationship provides the transformer impedance Z_T of a quarter-wave transformer.

$$Z_T = Z_o \sqrt{\frac{\phi_D}{\phi_T}},$$

where ϕ_D is the differential phase shift of the diode, as shown in Fig. 25, and ϕ_T is the differential phase shift required. Individual bits were tested before a complete three-bit phaser was put together. The bit accuracy for the 90° bit and 180° bit was ±3° and ±5°, respectively. To offset some of the slopes of the 90° and 180° bits, the 45° bit had a phase–frequency slope in the opposite direction. The average insertion loss of the 45°, 90° and 180° bits were 0.25, 0.38, and 0.53 dB, respectively.

Fig. 26 is a complete 3-bit phase shifter. The 45° bit is located in the center; the 90° and 180° bits are to the left and right, respectively, and are designed with three branch hybrids and transformers each.
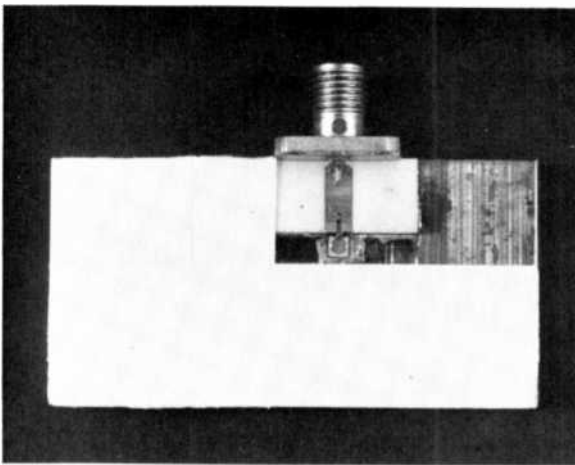
Fig. 24—Fixture for characterizing microwave PIN diodes.
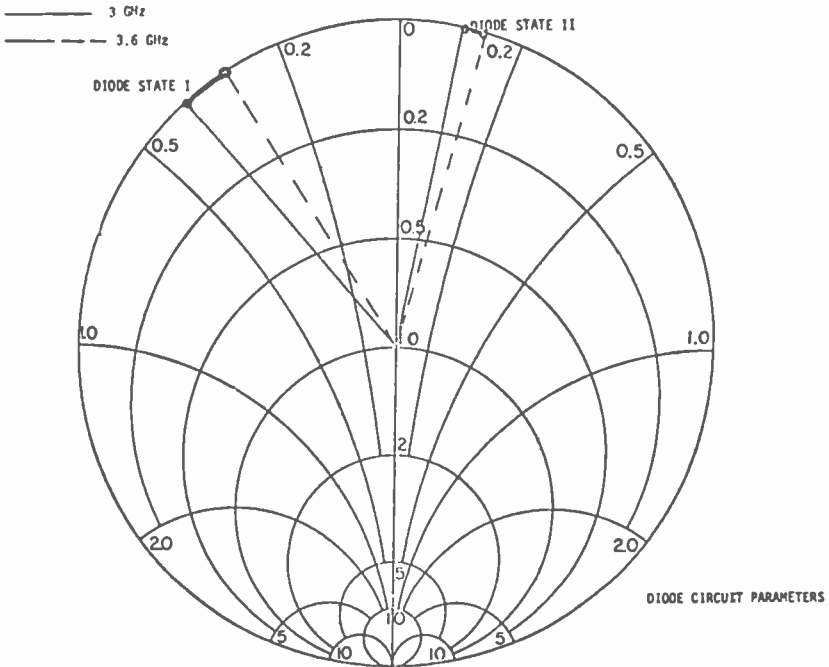
Fig. 25—Circuit parameters plotted on Smith chart.
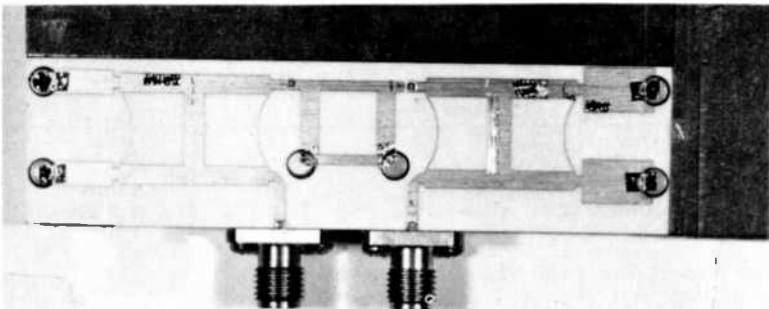
Fig. 26—Complete 3-bit phase shifter. The 45° bit is in the center; the 90° and 180° bits are to the left and right, respectively, and are designed with three branch hybrids and transformers each.
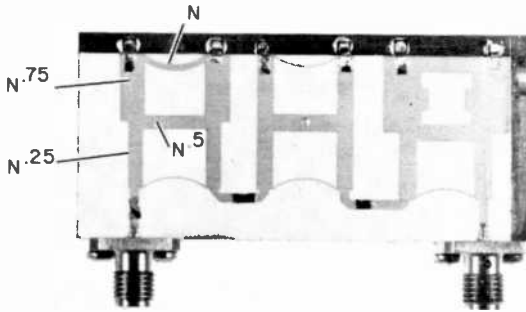
Fig. 27—Three-branch hybrid incorporating transformation. Transformation factors ($N = \phi_D/\phi_T$) on the line sections are indicated.

The transformation can be incorporated in the three-branch hybrid to save space. The transformation ratio $N = \phi_D/\phi_T$, and the transformation factors on the line sections of the hybrids are shown in Fig. 27. The performance of the phase shifter using all three-branch transforming hybrids is the same.

10. Phase-Shifter Performance

Table 8 summarizes the performance of 34 phase shifters. These data are compiled from data generated by an automated network analyzer.

The bit accuracy was 6.2° RMS and the average insertion loss was only 1.1 dB. The bias sensitivity was better than expected, permitting a reduction in driver and power supply specifications.

Power evaluation included "hot" switching of the phase shifter, zero-bias survival tests, measurements of leakage current power, phase sensitivities, and pulse fidelity.

Table 8—Low-Power Performance of Microwave IC 3-Bit Diode Phase Shifter (Summary of 34 Phase Shifters)

Bit Accuracy (RMS)	6.2°
Insertion Phase Variation (RMS)	5.7°
Insertion Loss, Average	1.1 dB
Insertion Loss Variance	0.25 dB
VSWR, Average	1.2
VSWR, Max.	1.5
Insertion Phase Linear per 50 MHz	±1°
Forward Bias at 50 mA/Diode	
Bias Current Loss Sensitivity	−0.3 dB/50 mÅ
Bias Current Phase Sensitivity	0.35°/50 mÅ
Reverse Bias at −40 V	
Bias Voltage Loss Sensitivity	−0.1 dB/40 V
Bias Voltage Phase Sensitivity	0.4°/40 V
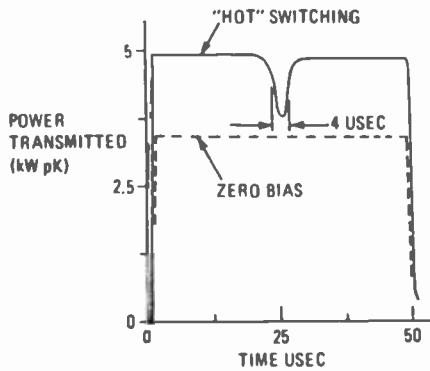
Fig. 28—Zero bias versus "hot" switching power transmission with 5-kW peak input to the phase shifter.

Experiments were conducted to show that "hot" switching is not as difficult to achieve as zero-bias survival. The areas above the curves, up to the 5 kW scale of Fig. 28, are the amounts of power dissipated for the two cases.

In the reverse bias state, the PIN diode shows a sharp increase in leakage current when the junction reaches about 180°C. Fig. 29 is a plot
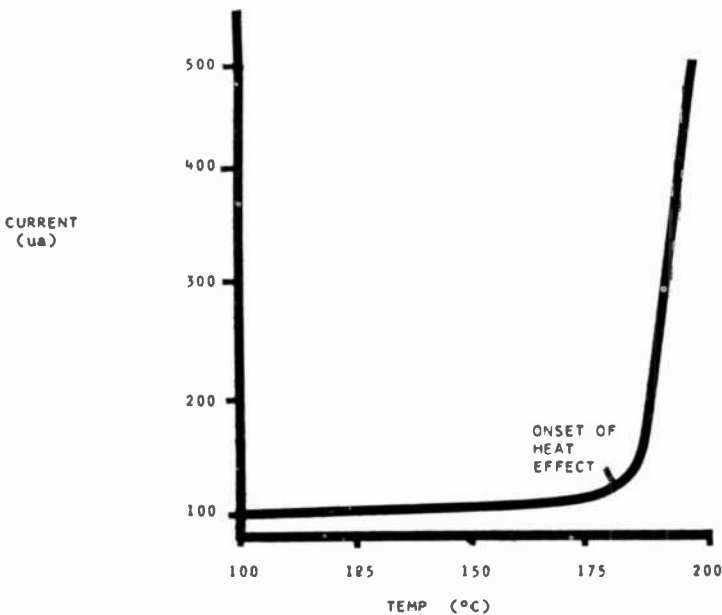
Fig. 29—Leakage current of 10 PIN diodes versus temperature.

of leakage current versus temperature for 10 diodes in parallel. It is this steep increase in leakage that limits the use of an accelerated life test at high temperature. In the forward bias state this leakage current does not present a problem.

At zero bias with high power applied, however, the condition of leakage current for some diodes could be reached at three times the incident power, as shown in Fig. 30. The sharp decrease in forward current as noticed on curve C is due to the increase in leakage current. At that point the junction has reached about 180°C.

At 40-V reverse bias, twice as much incident power could be applied to the same junction before heat-effect onset was reached (see Fig. 31).

Table 9 summarizes the high-power performance. There were no burnouts due to hot switching or zero bias at the indicated power levels. Increased insertion loss due to high-power compared with low-power tests was only 0.1 dB. Power sensitivities and pulse fidelity were satisfactory.

With the improvements in PIN diodes, high-power microwave integrated-circuit diode phase shifters offer comparable performance to stripline and waveguide forms at S-band, but with the significant advantage of very small size. The technique of incorporating the transformation into the design of the three-branch hybrids leads to further
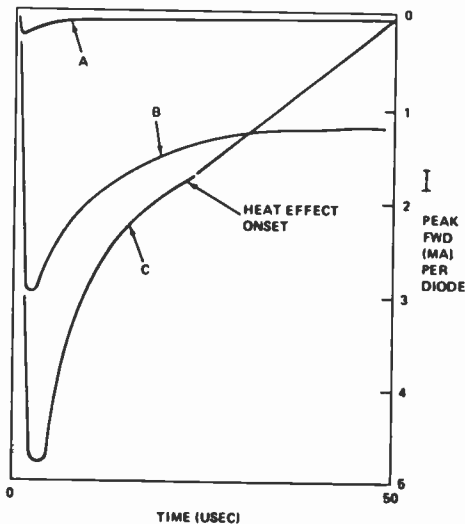
Fig. 30—Zero-bias forward current with power as the parameter. Curve A is for incident power, B for twice incident power, and C for three times incident power.
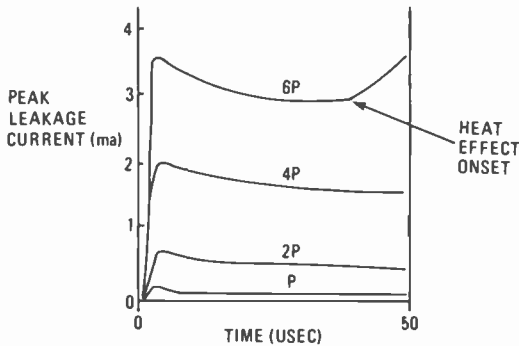
Fig. 31—Leakage current with power *P* as the parameter.

Table 9—High-Power Performance of Microwave IC 3-Bit Diode Phase Shifter

Hot Switching to 6.5 kW	No Burnout
Hot Switching Insertion Loss/Bit	0.8 dB
Zero Bias Operation to 5 kW	No Burnout
Zero Bias Insertion Loss	5 dB
Leakage Current at 1.5 kW	<0.1 mA
Leakage Current at 5 kW	0.1 mA
Increased Insertion Loss at 1.5 kW	<0.1 dB
Forward Bias Peak Power Phase Sensitivity	$1.3°$/dB
Reverse Bias Peak Power Phase Sensitivity	$1°$/dB
Switching Time Including Driver	$3 \mu s$
Delay Time Including Driver	$0.5 \mu s$
High Power Pulse Settling Time	
Amplitude	$0.4 \mu s$
Phase	$1 \mu s$
Pulse to Pulse Amplitude Variation	<0.05 dB
Pulse to Pulse Phase Variation	$<0.5°$

size reduction. The size advantage is becoming increasingly important in integrating the phase shifter with the radiating element in advanced phased-array-radar designs.

Acknowledgments:

The authors also appreciate the support of F. Sterzer, W. Patton and M. Breese in the initiation of the program, and the subsequent valuable discussions in which H. Veloric, J. Banfield, J. Vossen, J. O'Neill, and J. Zelez also participated.

References:

[1] H. A. Watson, Ed., *Microwave Semiconductor Devices and Their Circuit Applications*, H. M. Olsen, ch. 9, p. 286, McGraw-Hill, N.Y. (1979).

[2] H. S. Carslow and J. C. Jaeger, *Conduction of Heat in Solids*, 2nd ed., p. 264 ff, Oxford Univ. Press, London, 1959.

[3] P. T. Ho, G. A. Swartz, and A. Schwarzmann, "Low Loss PIN Diode for High Power MIC Phase Shifter," *1977 IEEE ISSCC*, vol. XX, p. 82.

[4] G. A. Swartz, A. Rosen, P. T. Ho, and A. Schwarzmann, "Low Loss PIN Diode for High-Power MIC Phase Shifter," *Trans. Electron Devices*, **ED-25**, Nov. 1978.

[5] R. S. Rosler, W. C. Benzing, and J. Baldo, "A Production Reactor for Low Temperature Plasma-Enhanced Silicon Nitride Deposition," *Solid-State Technol.*, **19**, p. 45, June 1976.

[6] A. Rosen, G. A. Swartz, F. C. Duigon, and A. M. Gombar, "Simple Method of Fabricating and Passivating High Power p-i-n Diodes," *J. Electrochem. Soc.*, **125**, p. 680 (1978).

[7] J. L. Vossen, "Control of Film Properties by RF-Sputtering Techniques," *J. Vac.-Sci. Technologies*, **8**, p. 512 (1971).

[8] A. W. Stephens, J. L. Vossen and W. Kern, "The Effect of Substrate Bias on Reactively Sputtered Silicon Nitride," *J. Electrochem. Soc.*, **123**, p. 303 (1976).

[9] A. Rosen, A. Gombar, and E. Mykietyn, "Stacked Configuration PIN Diode," private communication.

[10] J. L. Vossen and J. J. O'Neill, private communication.

[11] Environmental Analysis Laboratories, California, private communication.

[12] Y. S. Chiang and E. Denlinger, "Low Resistance, All Epitaxial p-i-n Diodes for Ultra-High Frequency Applications," *RCA Rev.*, **32**, p. 390, Sept. 1977.

[13] R. U. Martinelli and A. Rosen, "Storage Time Variations in Silicon p^+-n-n^+ Diodes," *1978 IEDM Technical Digest*, p. 556.

[14] M. Byczkowski and J. R. Madigan, "Minority Carrier Lifetime in p-n Junction Devices," *J. Appl. Phys.*, **28**, p. 878 (1957).

[15] H. J. Kuno, "Analysis and Characterization of p-n Junction Diode Switching," *IEEE Trans. Elec. Dev.*, **ED-11**, p. 8 (1964).

[16] J. Cornu, "Field Distribution Near the Surface of Beveled P-N Junctions in High-Voltage Devices," *IEEE Trans. Electron Devices*, **ED-20**, April 1973.

[17] G. J. Brucker, A. Rosen, and A. Schwarzmann, "Neutron Damage in PIN Diode Phase Shifters for Radar Arrays," IEEE Special Issue on Radioactive Hardening, Dec. 1978.

[18] R. J. Chaffin, "Permanent Neutron Damage in PIN Microwave Diode Switches," *IEEE Trans. Nuclear Science*, **NS-18**, p. 429, Dec. 1971.

[19] R. H. Dean and C. J. Nuese, "A Refined Step-Recovery Technique for Measuring Minority Carrier Lifetimes and Related Parameters in Asymmetric P-N Junction Diodes," *IEEE Trans. Electron Devices*, **ED-18**, No. 3, p. 151–158, March 1971.

[20] A. Schwarzmann, "The High Power Performance of a 5 kW MIC Diode Phase Shifter," *1978 IEEE MTT-S International Microwave Symposium Digest*, Ottawa, Canada, June 27–29.

[21] R. W. Burns and L. Stark, "PIN Diodes Advance High-Power Phase Shifting," *Microwave*, p. 38, Nov. 1965.

[22] E. C. Douglas and A. G. F. Dingwall, "Ion Implantation for Threshold Control in COSMOS Circuits," *IEEE Trans. Electron Devices*, **ED-21**, p. 324, June 1974.

On the Limits of the Electrophotographic Process

H. Kiess

Laboratories RCA Ltd., Zürich, Switzerland

Abstract—The limits of the electrophotographic process are investigated. A theoretical analysis shows that it should be possible to improve sensitivity as well as image quality considerably. An experimental investigation indicates that a sensitivity of ASA 100 can be achieved with CdSe as photoreceptor. The achieved image quality, however, does not meet these expectations. This discrepency was shown to be due to a lack in homogeneity of the charge acceptance and of the photosensitivity of the CdSe layers used.

1. Introduction

The investigation of the limits of the electrophotographic process has, beside its scientific interest, an economic and practical justification. To assess the potentialities of electrophotography, we will first compare the electrophotographic system in its present form with other photographic systems (Sec. 2). Then, in Sec. 3, we analyze the electrophotographic process with respect to sensitivity and image quality. Once this ground work has been laid, a more detailed discussion is given of the ultimate limitations on the sensitivity imposed by the development (Sec. 4.1) and by the photoreceptor (Sec. 4.2–4.8). Finally, some experimental results and an experimental demonstration of the principles outlined in the previous sections are presented.

2. Systems for Recording and Displaying Optical Information

Many systems are at present used to record and display optical information, the most prominent examples being the silver halide photographic process, television, and the electrophotographic process. These systems can be characterized by the sequence of steps each require to produce an image of the object to be taken. Table 1 gives a summary of these steps for all three systems.

In the case of the electrophotographic process, the object is imaged onto the photoreceptor, which must be sensitized prior to the exposure, i.e., it must be electrostatically charged. Usually the charging is achieved with a corona discharge unit. Therefore, a high voltage supply must be available, although the power requirements tend to be low (of the order of 5×10^{-4} watt per cm^2 to be charged) if losses during charging can be avoided and if the required charging time is about one second. After exposure the latent image is developed. The developing is actuated by the electrostatic forces between the charged areas of the latent image

Table 1—Steps Required to Produce an Image

System:	Electrophotography	Silverhalide-Photography	Television
Technological Character of the Process	Electrostatics	Chemistry	Electronic
Sequence of procedure steps	Original ↓ Imaging System — Charging System ↓ ↓ Photoreceptor ↓ Latent Image ↓ Development ↓ Image Hard Copy	Original ↓ Imaging System ↓ Photogr. Film ↓ Latent Image ↓ Development ↓ Image Hard Copy	Original ↓ Imaging System ↓ Image Sensor (CCD-Image Sensor, Vidicon) $(x-y) \rightarrow f(t)$ ↓ Storage (magn. tape, memory) $f(t) \rightarrow f(z)$ ↓ Display System $f(z) \rightarrow f(t) \rightarrow (x-y)$ Inkjet-printer / TV-Receiver Hard Copy / Soft Copy

and the charges located on the pigment particles of the developer. The dark decay of the charge on the photoreceptor is of the order of minutes. Thus, it is mandatory that the picture be taken and the latent image developed within a fraction of the dark decay period; otherwise the information will be distorted or even lost. The total time needed to obtain an image, including charging of the photoreceptor, exposure, and development, must be kept short; in practical systems, it is of the order of a few seconds. The low costs of the raw material and the simplicity of the process are the reasons why electrophotography dominates the field of copying and low-volume printing. Its limitations are low sensitivity and the inadequacy of gray scale reproduction.

The silver halide photographic process is well known and needs little comment. The sequence of steps is the same as that of the electrophotographic system, except that a sensitization step prior to exposure is not required. The film is always ready for exposure. The latent image, in contrast to that obtained in the electrophotographic process, can be stored for a long period of time, typically of the order of one year. Therefore no immediate processing of the film is required after exposure. The disadvantage of this system lies in the relatively high costs of the film and the long time required for developing the latent image—a process that requires wet chemicals. The chief advantages of silver halide photography are the small size of the apparatus required and the high quality of the pictures.

In both the electrophotographic and silver halide systems, the optical information is projected onto a plane and then processed in this plane. In contrast, a TV storage system transfers the information on the photoreceptor into a time dependent function $f(t)$ and then stores it, e.g., on a magnetic tape, as a linear function $f(z)$. For retrieval of the information, the time-dependent signal is restored and used to drive a TV receiver, which displays the image. Hard copy might be obtained from such a system with an electrophotographic technique or by using the time-dependent signal to drive an ink-jet printer. A television camera employing charge-coupled devices in combination with appropriately designed memories could make such a system attractive for photography, since the camera could be compact. The obvious advantages are that the information could be amplified and image-enhancement techniques applied, and various means to display the image would be readily accessible. The disadvantage is the extreme complexity of the components, which has so far hindered the use of this technique for photography.

Thus, with the present state of the art, good reasons exist to explain why each of the techniques covers only a specific domain in the field of recording and displaying pictorial information. If certain shortcomings can be be surmounted, however, an electronic system using TV tech-

niques or an electrostatic system based on the electrophotographic process could conceivably compete with silverhalide photography. In the case of electrophotography, this means improvement of the sensitivity of the process, the storage capability of the latent image, and of the image quality with respect to reproduction of gray scale. In the remainder of this paper, we focus our discussion on these points, with particular emphasis on sensitivity.

3. An Analysis of the Electrophotographic Process

3.1 Sensitivity and Gray Scale

A discussion of sensitivity and reproduction of a gray scale can be best performed using the four quadrant chart[1] in Fig. 1. The combined influence of the photoreceptor and the development process is then easy
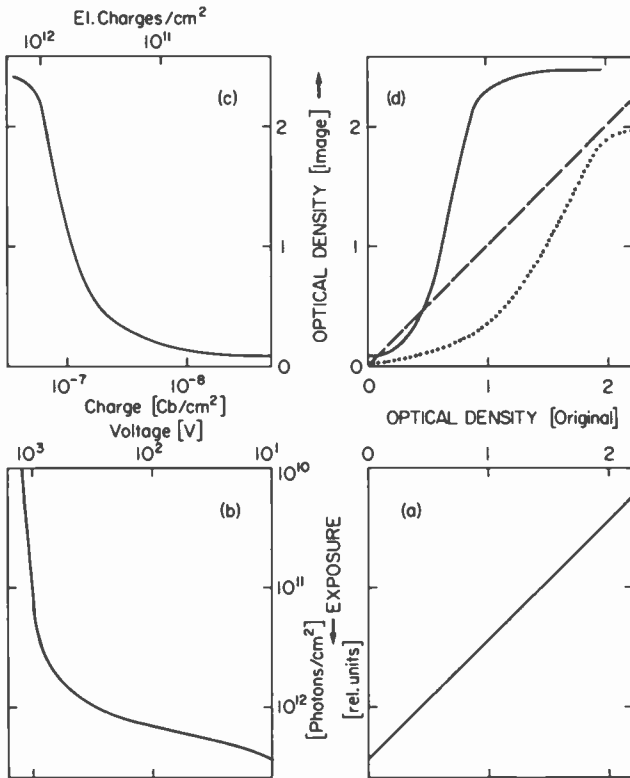

Fig. 1—Four-quadrant-chart representation of the original-to-image tone reproduction.

to visualize. Fig. 1(a) gives the relation between the optical density of the original (in the case of a copying process) and the amount of light falling on the photoreceptor and giving rise to locally varying exposures. The relationship between exposure and surface voltage is shown in Fig. 1(b). The toning characteristic is displayed in Fig. 1(c), i.e., the optical density obtained with a toning process as a function of the surface voltage. In Fig. 1(d), a comparison is made between the optical density of the image and that of the original. If in Fig. 1(d) a straight line under 45° is obtained (dashed line in the figure), then an ideal reproduction has been achieved without any distortion of the information content of the original.

Photographic processes, however, are never ideal. If we compare the original with the image obtained with, e.g., a positive silver halide film, it is seen that a considerable distortion of the gray scale of the original occurs. As an example, a characteristic curve for a positive silver halide film is shown by the dotted line in Fig. 1d.[2] The exposure of such a film lies between 10^{10} and 10^{11} photons per cm^2, as required to take pictures with a camera at reasonably short exposure times.

By comparison, the gradation obtained in the electrophotographic process is even steeper than that of the positive film and the exposure is in the range between 10^{12} and 10^{13} photons per cm.[2] The deviation of the characteristic curve from the ideal one in Fig. 1(d) and the lack of sensitivity are the result of a combined effect—the exposure characteristic of Fig. 1(b) and the toning characteristic of Fig. 1(d) are not matched to give either the highest possible sensitivity or to approach the ideal characteristic curve of Fig. 1(d). For the remainder of this section, therefore, we discuss why at the present state of the art the electrophotographic process performs as it does.

3.2 Sensitivity of the Electrophotographic Process

(a) *The development process.*

We will not use the ASA definition[3] for the speed of the electrophotographic process, but rather will use a definition for the sensitivity that allows us to establish a correlation between the sensitivity and its physical parameters. In particular, we define the sensitivity S as the product of the efficiency η of the photoreceptor and of the sensitivity θ of the developing process:

$$S = \eta\theta. \tag{1}$$

Hence, the sensitivity is split into two factors that can be discussed separately. The sensitivity θ of the developing is determined by the amount of charge needed to actuate it; in general it is higher the lower the charge density required to achieve a certain optical density.

For the sake of clarity and the ease of the arguments to come, we will assume powder cloud developing is the process used to develop the latent image on the photoconductor. Other developing processes lead to similar results, so that our selection represents no real restriction to the general validity of the considerations here.

We assume that an optical density of 2 of the image represents the highest optical density required for adequate image quality. Furthermore, we assume that the absorption constant of the toner particles lies between 10^4 and 10^5 cm^{-1}, so that a monolayer of particles having a thickness of $\sim 10^{-4}$ cm is sufficient to obtain an optical density of ≥ 2. It is known[4] that the charge on toner particles is proportional to their surface area and that particles with a diameter of a $2\ \mu$m carry a charge of about 500 elementary charges. This is indeed the highest charge that a particle of this dimension can have, since higher charges would lead to an electrical breakdown of the surrounding air.

After toner deposition, neutrality should prevail, i.e., the surface charge on the photoconductor should be exactly compensated by the charge of the deposited toner particles. For this condition, a charge density of 1.25×10^{10} elementary charges per cm^2 is needed to obtain an optical density of ≥ 2. This charge density represents an upper boundary, since our calculation has assumed the highest possible charge on the toner particles. Also, our estimate should be valid for a wide range of toner particle diameters (the surface as well as the cross sectional area of the particles, which are effective for the absorption of the light, are proportional to the square of the diameter). Thus the charge density required on the photoreceptor should be independent of the particle size down to diameters at which the optical density of 2 can no longer be achieved due to the limited thickness of the toner particles. In practice, however, charge densities are used that are far greater than 10^{10} elementary charges/cm^2, about two orders of magnitude higher. Why is this so?

The toner deposition usually takes place in a geometrical configura-
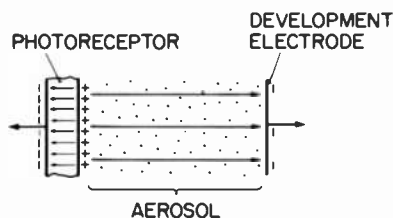

Fig. 2—Geometrical configuration of photoreceptor and development electrode during development.

tion, as shown in Fig. 2. The electric field strength in the development space is about 10^{-3} times smaller than in the photoreceptor itself due to the geometry involved. If we assume that the lowest force needed to deposit a particle is determined by the force of gravity, then an easy calculation shows that the photoreceptor must be charged to $1-2 \times 10^{10}$ elementary charges/cm^2 in order to start toner deposition.*

Only that charge deposited in addition to this bias charge can be utilized to carry the optical information. Hence, if an optical density of 2 is to be achieved we must deposit another 1.25×10^{10} elementary charges/cm^2. In such a system, small fluctuations of the bias charge give rise to serious distortions of the image charge. When the image charge is added, the electric field in the development space is, of course, also doubled and has a value of 10 V/cm. Therefore, small fluctuations of the toner deposition mechanism could be disastrous. The remedy for this situation is to increase the image charge in order to improve the signal-to-noise ratio. In television, the signal-to-noise ratio is usually chosen to be 50 dB. If we take the same S/N ratio and if we assume that the bias charge density fluctuates by 10%, then the charge density on the photoreceptor must be 6×10^{11} elementary charges/cm^2. This is close to the empirical value of 10^{12} elementary charges/cm^2. Thus for these conditions the high charge density is justified.

(b) The Photoreceptor.

Let us now consider the efficiency of a particular photoreceptor that is often used in electrophotography, namely, amorphous Se. The efficiency η is defined as the number of elementary charges dissipated per absorbed photon on the surface of the photoreceptor. The relationship of η for surface charge density Q_s (or electric field) for amorphous Se is shown in Fig. 3. The efficiency decreases strongly with decreasing field. At a surface charge density of about 10^{12} elementary charges/cm^2, approximately two photons are needed to dissipate one elementary charge, whereas about 100 photons are required if the surface charge density is lowered by a factor of 100. If we assume that the relationship $\eta = f(Q_s)$ is linear, then it would be irrelevant whether the discharge takes place

---

*The lowest field that attracts a particle has to overcome the field of gravity. Therefore, if the particles are assumed to be at rest, the threshold field is given by $E = G/q$, where G is the particle weight and q is the particle charge. For particles of 2 μm diameter with a charge of 500 elementary charges, the threshold field is ~5 V/cm, and hence the field in the photoreceptor has to be approx. 5×10^3 V/cm. From this value for the electric field the surface charge density is calculated. Since the weight of the particle G is proportional to d^3 and the charge $q \propto d^2$, the threshold field increases with increasing particle diameter d. Therefore the threshold field and the bias charge density are only valid for the particles specified.
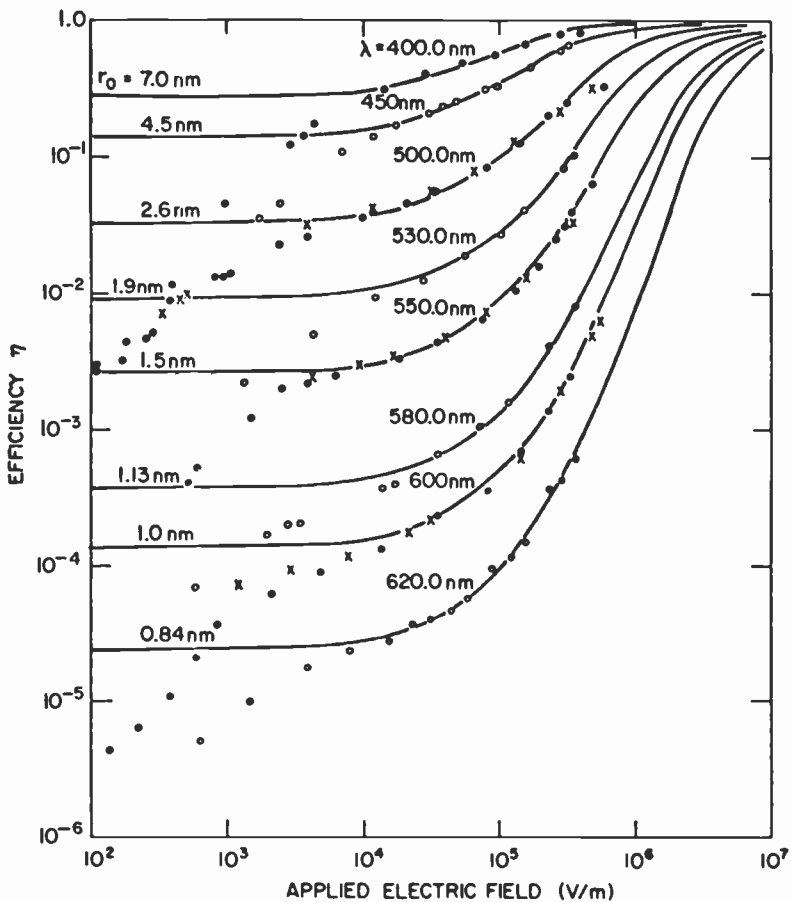
Fig. 3—Efficiency of Se as a function of electric field at various wavelengths (after Pai and Enck[27]).

between a surface charge density of 10^{12} and 10^{10} or 10^{10} and 10^{8} elementary charges/cm^2, since in both cases the exposure, i.e., the number of photons needed to discharge the photoreceptor, would be the same. The relation $\eta = f(Q_s)$ is not linear, but it is sufficiently close that we do not expect any significant reduction of the exposure by reducing the surface charge density on the Se. In general, the efficiency decreases with decreasing field for most of the photoreceptors used in electrophotography, although the physical reasons for the drop in efficiency may be quite different. Therefore, at first sight, it would seem that the efficiency of the photoreceptor and the sensitivity of the development are matched and limited by their very nature and that no significant improvement in the sensitivity of the electrophotographic process is possible.

(c) *Gradation.*

One remark remains to be made concerning the gradation of the electrophotographic process. We have seen that a surface charge density of $\sim 10^{10}$ elementary charges/cm^2 is required as bias charge to initiate the deposition process of the toner particles and that an additional 10^{10} elementary charges/cm^2 are sufficient to obtain an optical density of 2. These numbers put us in a position to establish an approximate relation between the optical density and the surface charge density for a photoreceptor charged to 10^{12} elementary charges/cm^2 (Fig. 4). The optical density rises sharply from the background density to the high value of 2 in the surface charge density range between 1 and 2×10^{10} elementary charges/cm^2. Optical densities in excess of 2.5 to 3 are seldom obtained, and even if they could be achieved, they barely could be utilized by the human eye.[5] Therefore, in the charge density range between 2×10^{10} and 10^{12} elementary charges/cm^2, the optical density only increases from 2 to about 3 in practice. The curve is indicative of the steep gradation of the electrophotographic process, which is due to the existence of a bias charge and its fluctuation, both of which mar the utilization of charge densities below 10^{10} elementary charges/cm^2. For copying alphanumeric information, such an optical density versus charge density curve can be
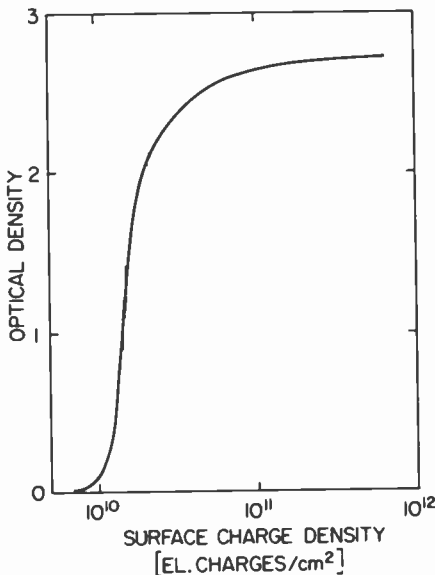
Fig. 4—Optical density as a function of surface charge density obtained with a model toner. Diameter of toner particles is 2 μm.

of advantage, since it gives a certain latitude in exposure; it is completely unsuitable, however, for copying pictorial information.

4. An Improved Electrophotographic Process.

4.1 The Development of Electrostatic Charge Patterns.

The reasons for the poor performance of the developing process are twofold. First, the field in front of a photoreceptor is only a small fraction of the internal field, so that the charge density needed to generate the bias field is comparable to the charge density required to obtain an optical density of 2. Second, the noise problem imposed by the approximate equality of the bias and image charge is solved by overcharging the photoreceptor sufficiently to give a reasonable signal-to-noise ratio.

The poor characteristics of the particle deposition are due to the choice of the geometrical configuration. A recently proposed system[6] using a different geometry shows a considerable improvement over previously existing schemes. Here, the charge pattern of the latent image is replicated from the photoreceptor onto an insulating film in the form of a monopolar charge pattern. The monopolar charge pattern is then developed conventionally. The proposed configuration during charge transfer is shown in Fig. 5. A thin insulating (plastic) film is brought into close contact with the photoreceptor. Then the free surface of the film is made conducting and is grounded with a conductive volatile liquid. If we assume that the insulating and the photoconducting films have the capacitance C_1 and C_2, respectively, then the charge induced on the insulating film is

$$Q_{ind} = Q_s \frac{C_1}{C_1 + C_2} \tag{2}$$

where Q_s is the surface charge density on the photoreceptor. After evaporation of the liquid, the insulating film is removed. A monopolar

Fig. 5—Generation of a monopolar charge pattern from a latent image: (a) induction of the charge on the insulating film and (b) separation of the film and generation of the monopolar charge pattern.

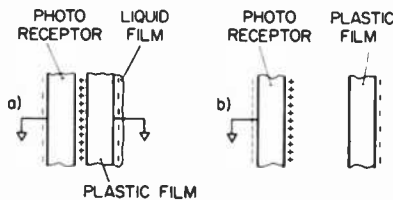charge pattern remains on its surface, provided the fields are sufficiently low that breakdown of the air is avoided. The formation of the monopolar charge pattern is accompanied by a strong increase in energy. The energy U_{ph} stored in a charged photoreceptor is

$$U_{ph} = \frac{1}{2} \frac{Q_s^2}{C_1}. \tag{3}$$

The energy of the monopolar charge pattern is given by

$$U_m = \frac{1}{2} \frac{Q_{ind}^2}{C}, \tag{4}$$

Where C is the capacitance of the free film. If we insert the induced charge Q_{ind} from Eq. [2], we obtain for the energy ratio

$$\frac{U_m}{U_{ph}} = \frac{C_1}{C} \frac{C_1^2}{(C_1 + C_2)^2}. \tag{5}$$

Obviously, U_m/U_{ph} is determined by the capacitances involved. If we assume a circular area to be charged, then C can be calculated[7] and is found to be $C \approx 4 \times \epsilon\epsilon_0 D$ where D is the diameter of the charged area and ϵ and ϵ_0 are the relative and absolute dielectric constants at the ambient. C_1 is determined by D, the thickness l, and the dielectric constant of the photoreceptor ϵ_{ph}. Hence, if C_2 is assumed to be approximately equal to C_1, Eq. [5] becomes

$$\frac{U_m}{U_{ph}} = \frac{\pi}{16} \frac{\epsilon_{ph} D}{\epsilon l} \tag{6}$$

For a photoreceptor with a thickness of 10^{-3} cm, a dielectric constant of 10, and a charged area of 1 cm, this ratio becomes approximately 2000. If we take the change in energy upon developing as a measure of the driving force for the developing, then obviously the speed of developing as well as the developability of weakly charged areas increase by orders of magnitude after formation of a monopolar charge pattern in comparison to the dipolar charge pattern on the photoreceptor.

If the process is to be useful, the following condition for the amount of the induced charge density Q_{ind} must be fulfilled. Q_{ind} should be below the breakdown field of the air and it should be higher than, or at least equal to, the charge density Q_o required to obtain an optical density of 2 by the deposited toner particles. Therefore, we have

$$Q_o \leq Q_{ind} \leq \epsilon_0 \vec{E}_b, \tag{7}$$

where $\vec{E}_b$ is the breakdown field of air. The breakdown field in air is about 3×10^4 V/cm, which corresponds to a charge density of 1.5×10^{10} elementary charges/cm^2. Q_o has been found to be 1.25×10^{10} elementary

charges/cm^2, so that indeed condition [7] can be fulfilled. The electric field, even at an appreciable distance from the fully charged surface of the film, is 2×10^4 V/cm, while the minimum bias field necessary to move a toner particle has been found to be approximately 5 V/cm. At first sight, therefore, there seems to be room left, at least in terms of electric field and charge density, for the reproduction of a decent gray scale and for a sufficiently large dynamic range. However, more detailed discussion is in order, since noise has not been taken into account.

Two noise sources dominate in monopolar charge patterns. The first corresponds to what is called fog in photography, i.e., areas of the image that should appear completely transparent show a small background optical density. This means, in the context of electrophotography, that toner is deposited in areas of the photoreceptor that are completely discharged. If the charge induction technique is used to transfer the latent image to an insulating film, then, due to the contact potential of the photoreceptor, charge is also induced on the film even if the photoconductor is completely discharged (Fig. 6). The charge density on the film is

$$Q_{ind} = V_c\, C_1. \qquad [8]$$

Here use was made of Eq. [2], assuming that $C_2 \ll C_1$ and that Q_s can be replaced by $Q_s = V_c C_2$, where V_c is the contact potential difference.

The second source of noise is common to all electrophotographic systems and is due to the inhomogeneous charge deposition and charge acceptance of the photoreceptors. If we assume the charge fluctuation to be ΔQ then the signal-to-noise ratio is

$$S/N = \frac{Q_{ind}}{\Delta Q + V_c C_1}, \qquad [9]$$

or, in terms of surface voltage V_s and contact potential difference, we have

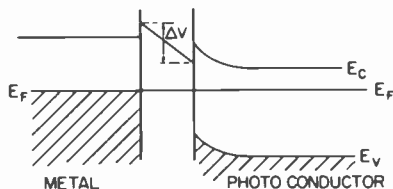$$S/N = \frac{V_s C_2 C_1}{\Delta V_s C_2 C_1 + V_c(C_1{}^2 + C_1 C_2)}. \qquad [10]$$

Fig. 6—Contact potential difference V_c between a metal and a photoreceptor.

All other possible noise sources have been neglected here.[8] Nevertheless, this formula reflects the problems involved in the electrophotographic process in general and in this transfer technique in particular. If the surface voltage V_s is chosen to be sufficiently large compared to V_c, we may expect that the fluctuation ΔV_s will dominate in the denominator, so that S/N is solely determined by $V_s/\Delta V_s$. The ratio $V_s/\Delta V_s$ can be considered to be independent of the surface voltage of the photoreceptor after partial discharge by light. Therefore, with decreasing surface charge, the second term with V_c in the denominator will become important and cause the signal-to-noise ratio in the nearly discharged areas to deteriorate. This is shown in Fig. 7.

For a signal-to-noise ratio of 50 dB, both ΔV_s and V_c should be approximately $0.003 \times V_s$. By appropriate selection of the materials, the contact potential difference can be minimized, so that even for small surface voltages V_s this condition can be fulfilled. Control of ΔV_s is probably more difficult to achieve. A relative fluctuation $\Delta V_s/V_s$ as low as 0.003 implies that the charge-deposition technique must be under good command and also that the photoreceptor to be charged must be fairly homogeneous with respect to charge acceptance and light induced discharge. If the required S/N ratio is not achieved, the image will be of poor quality; in particular, fine steps of a gray scale will remain invisible and the dynamic range will suffer.
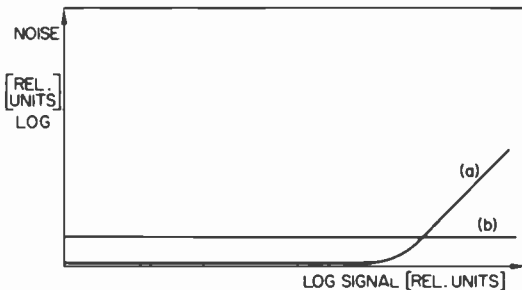
Fig. 7—Noise as a function of signal. Curve (a) represents the noise due to surface charge fluctuations, curve (b) that due to the contact potential.

4.2 Conditions for an Efficient Photoreceptor

The efficiency of a photoreceptor is defined as the ratio of the number of photons/cm^2 needed to dissipate the surface charge to the number of elementary charges per cm^2 on the surface. Therefore the smaller the number of photons required to dissipate the charge, the higher the efficiency. The aim, in the context of the previously discussed sensitivity

of the development process, is to obtain an efficiency as high as possible at and below charge densities on the photoreceptor of $\sim 2 \times 10^{10}$ elementary charges per cm^2, which means at fields $\leq 10^4$ V/cm. Since all photoconductors used in electrophotography so far perform badly at low fields, the question of the mode of operation and of which materials parameters are relevant will be investigated in more detail.

4.3 Operation at Constant Voltage

The claim has repeatedly been made[9] that the efficiency of photoreceptors can be raised to values above unity, i.e., that one photon can cause the dissipation of more than one elementary charge on the surface. The usual argument is that gains of up to 10^4 can be observed for steady-state photocurrents. H. S. Sommers, Jr.,[10] and A. Rose[11] have shown, however, that the highest efficiency possible for photoreceptors in photographic systems is unity, and that the efficiency is independent of the mode of operation and of the contacts used. We will briefly review the arguments leading to this conclusion for the case of ohmic contacts and constant applied voltage, i.e., the case of an electrophotographic system that utilizes the change of current due to illumination (Fig. 8). The main reason for an efficiency below unity is that, in photographic applications, the gain of stationary photocurrents is irrelevent. Of interest rather is the number of photons/cm^2 that must be invested to generate a certain current density after the onset of light. We assume now that the photocurrent is dominated by one type of carrier, although both electrons and holes are generated across the gap. This assumption is necessary if the gain of the stationary photocurrent is to be high.[12] The rise of the photocurrent depends on trapping. Each trapped carrier has been excited to the conduction band by the absorption of one photon, so that the number of trapped carriers is identical to the number of photons needed to generate them. The density of trapped carriers is in general given by

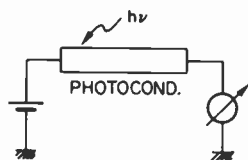$$N_t = \int_{\zeta_f}^{0} N(E)f(E)dE - \int_{\zeta_a}^{0} N(E)f(E)dE \qquad [11]$$

Fig. 8—Electrophotographic system that utilizes the change of current and is operated at constant voltage and with ohmic contacts.

$N(E)$ is the density of trapping states in the forbidden gap, $f(E)$ is the Fermifunction. ζ_f and ζ_a represent the position of the Fermi level before illumination and after the stationary photocurrent has been reached. In order to relate this to efficiency, one must compare the number of trapped carriers $(N_t l)$ with the number of elementary charges/cm^2, Q_s/e, on the contacts of the photoconductor. If blocking contacts had been used on the photoreceptor, then ideally the efficiency would be unity and, therefore, the number of photons needed to dissipate Q_s would be identical to the number density of the surface charge Q_s/e. Therefore, if the charge stored in the traps is larger than that on the contacts,

$$(N_t l) \geq Q_s/e, \tag{12}$$

then the efficiency is not improved over that for a photoreceptor operated with blocking contacts. Following arguments of Rose,[11] we assume now that the current in the photoreceptor is space-charge limited and that the current must be increased by the light by a factor of two to become observable. Then obviously $N_t l = Q_s/e$, since the onset of space-charge-limited current flow is given by the condition $(n + N_t)l = Q_s/e$,[13] where the free carrier concentration n is small compared to N_t. If the current is doubled, then the Fermi level is shifted by kT, and n, as well as N_t, is doubled. Hence $N_t l$ must be approximately equal to Q_s/e, which means an efficiency of unity if the current doubling was actuated by light. If the photoreceptor is operated at voltages below the space-charge-limited current regime, then $Q_x/e < (N_t + n)l$ and, therefore, doubling the current is achieved only with an efficiency smaller than unity.

4.4 Efficiency of Photoreceptor with Blocking Contacts

Using a photoreceptor with blocking contacts, one of which is floating, represents the normal mode of operation in electrophotography. The number of photons N_{ph} required to dissipate the charge on the floating electrode is related to the exposure time t by

$$N_{ph} = B_0 t. \tag{13}$$

Here B_0 is the incident light intensity in photons/cm^2 sec. The continuity equation states that, in the configuration of a solid with a free charged surface, the sum of the electron and hole current j and of the displacement current is zero during the discharge:

$$j(x,t) = -\epsilon \epsilon_0 \frac{\partial \vec{E}}{\partial t}. \tag{14}$$

ϵ and ϵ_0 are the relative and absolute dielectric constant and $\vec{E}$ is the electric field. Integration with respect to x gives

$$\int_0^l j(x,t)dx = \epsilon \epsilon_0 \frac{dV}{dt}. \tag{15}$$

Within certain limits[14] we may assume that j is independent of x. Then the discharge time is obtained by a simple integration,

$$t = \frac{\epsilon\epsilon_0}{l} \int_V^0 \frac{dV}{j(V)},$$ [16]

if $j(t) = j[V(t)]$. The convenience of this approximation is that only the $j(V)$ characteristic has to be calculated to obtain t. Also, Eq. [16] shows that all the processes that determine the exposure time are contained in the current density versus voltage characteristics. The efficiency is obtained by dividing the surface charge density Q_s/e by the number of incident photons/cm^2. Hence η is found using Eqs. [13] and [16]:

$$\eta = \frac{Qs/e}{B_0} \frac{1}{\frac{\epsilon\epsilon_0}{l} \int \frac{dV}{j(V)}}.$$ [17]

If the photocurrent density is saturated as a function of voltage, then $j = eB_0$, which, when inserted into Eq. [17], gives the well known efficiency of unity for photoreceptors with blocking contacts.

In general the current density j in a photoconductor is given by

$$j = eg\mu_n\tau_n\vec{E} + eg\mu_p\tau_p\vec{E},$$ [18]

where g is the generation rate in cm^{-3} sec^{-1}, τ_n and τ_p are the lifetimes of the electrons and of the holes, respectively, and the other symbols have their usual meaning. Since the contacts were assumed to be blocking, the current can only be due to the extraction of charge carriers that are generated either thermally or optically in the bulk of the photoreceptor.

In general, the photogeneration rate g and the drift length $\mu\tau\vec{E}$ are a function of the local field and of the voltage, respectively. For this discussion it is advantageous to treat both effects separately, though in practice they may affect the j-V characteristics of photoconductors similarly. Often a separation of the various effects is difficult to achieve.

4.5 Photogeneration

The photogeneration rate $g(x)$ is given by

$$g = \gamma B_0 \chi e^{-\chi x}$$ [19]

where χ is the absorption constant and γ is the photogeneration efficiency. The term $B_0\chi e^{-\chi x}$ determines the number of photons absorbed per sec and per cm^2 at position x, whereas γ is the ratio of the number of photogenerated free carriers and of the number of absorbed photons.

Our interest will be focused in the following to the photogeneration efficiency.

According to Warter[15] the photogeneration of charge carriers can be divided into two steps, an excitation step and an escape step. The excitation step involves the initial absorption of a photon and a thermalization process whereby the electron–hole pair separates while losing kinetic energy imparted by the photon. The escape step involves the drift of the two separated carriers under the influence of the applied field. Hence, it can be described in terms of the conventional photoconductive processes.

We consider now the separation of the electron–hole pairs in the thermalization process. This involves the loss of kinetic energy; depending on whether or not the electron and the hole are separated by more than a certain distance after thermalization, the carriers are free or else they form a bound state and recombine with a probability p_r. Therefore, it is logical to rewrite the photogeneration efficiency γ as

$$\gamma = \frac{p_i}{p + p_r}, \qquad [20]$$

where p_i is the probability of generating free carriers. p_r is in general a function of the thermalization radius r_c and will become vanishingly small whenever r_c is greater than some critical value. In these conditions $\gamma = 1$. We take as the critical value for that radius the Coulomb capture radius r_{coul}. If the electron and hole are separated after thermalization by more than r_{coul}, then the carriers will not immediately recombine but diffuse away. Therefore we assume that $p_r = 0$, if $r_c \geq r_{coul}$. The Coulomb capture radius is given by $r_{coul} = e^2/(2\epsilon\epsilon_c kT)$.[13] The thermalization radius will be estimated by assuming that it is proportional to the mean free path of the charge carrier with an energy E above the conduction band (for holes below the valence band edge).* Then we can write for r_c

$$r_c = v\tau_e. \qquad [21]$$

τ_e is the emission time for the phonons to which the energy is lost and v is the velocity of the carrier at kinetic energy E. The emission time is calculated from the rate of energy loss, which can be expressed in the form[17]

$$\frac{dE}{dt} = Av^n, \qquad [22]$$

---

*Knights and Davies[16] used the diffusion length $l_D = \sqrt{D\tau}$ as thermalization radius. Since in general the energy of the excited carriers is well above the thermal energy, it is not quite clear which value of D and τ should be taken.

A and n are constants determined by the loss mechanism; in particular they depend on whether the carriers lose their energy by optical or acoustical phonons, by impact ionization, or by some other loss mechanism. We will restrict our considerations here to the loss of energy by optical phonons; other loss mechanisms have been treated elsewhere.[18] If this loss mechanism prevails, then $n = -1$ and $A = (\epsilon_s - \epsilon_\infty)e^2\omega^2/(\epsilon_s\epsilon_0\epsilon_\infty)$, where ω is the phonon frequency and ϵ_s and ϵ_∞ are the low and high frequency dielectric constant, respectively.

The emission time is obtained by integrating Eq. [22] and replacing the velocity by $v = \sqrt{2Em}$. Inserting the emission time into Eq. [21] gives the thermalization radius r_c:

$$r_c = \frac{4\,E^2\,\epsilon_s\epsilon_\infty\epsilon_0 h^2}{3\,E_{ph}^2\,(\epsilon_s - \epsilon_\infty)em}.$$ [23]

The phonon frequency ω has been replaced by the phonon energy E_{ph} $= \hbar\omega$. The thermalization radius is thus inversely proportional to the effective mass m; hence, r_c will increase the lower the value of m (i.e., the greater the mobility of the carriers in a material) other parameters remaining constant. For a photogeneration efficiency $\gamma = 1$, r_c is equal to or greater than the coulomb capture radius, which gives the condition for the effective mass (or mobility) of the material that m has to be smaller than the limiting value:

$$m \le \frac{4\,E^2\epsilon_0\epsilon_\infty}{3\,E_{ph}^2\,(\epsilon_s - \epsilon_\infty)}\,\frac{2\epsilon_s\epsilon_0^2 h^2 kT}{e^2}.$$ [24]

For III–V compounds, $\epsilon_s\epsilon_\infty/(\epsilon_s - \epsilon_\infty)$ is of the order of 10^2. If E/E_{ph} is assumed to be 4 (with $E = 0.1$ eV and $E_{ph} = 0.025$ eV), then the effective mass should be $m \le 0.1$ for the photogeneration efficiency to become unity.

Similar conditions for the effective mass can be deduced for other loss mechanisms. Numerical estimates show that in those cases also the effective mass must be one or smaller than one if the photogeneration efficiency is to become one.

Thus far the arguments put forth are valid for crystalline materials with well defined (in terms of density of states) conduction and valence bands and energy gaps. In the case of amorphous photoconductors, the bands are not very well defined, since tails of localized states expand into the forbidden gap.[15] However, because of the change in the nature of the states, the mobility should fall by several orders of magnitude from values characteristic of transport via extended states to those characteristic of phonon-assisted hopping conduction in localized states. The energies at which the rapid change in mobility is to take place are called the mobility edges (for the electrons and the holes). In general, it is not

known how the mobility changes with energy near the mobility edges. It might be stepwise, linear with energy, or it might be some S-shaped curve.[20] If we assume that the S-shaped curve is closest to reality, it is nevertheless also reasonable to assume that the photoexcited carriers relax quickly to the mobility edge by loss mechanisms as described before, but that the relaxation to states lying below the mobility edges is considerably slowed due to the localization of the carriers in those states. The consequence of these assumptions is that the extended states are important for the photocurrent and that the localized states, in our context, play a role similar to that of traps in crystalline solids. Surely, this is not the only viable model for photoconduction in amorphous materials, and other models have been proposed.[21] But it allows us to qualitatively draw the conclusion, which is also true in the case of amorphous photoreceptors, that a high mobility is warranted in the extended states in order to obtain a γ of unity.

If the photogeneration efficiency is smaller than unity at zero field, then it will become a function of the electric field. The photogeneration efficiency will increase above the zero-field value whenever the lowering of the potential due to the applied field is comparable to kT (Fig. 9). From this condition, we obtain

$$\vec{E}_{th} = \frac{kT}{er_{coul}} = \left(\frac{kT}{e}\right)^2 \frac{2\epsilon\epsilon_0}{e}. \tag{25}$$

For materials with $\epsilon = 10$, we expect γ to increase at fields greater than 10^4 V/cm. This implies, in fact, that the field-aided separation of the carriers is ineffective for the range of fields at which the photoreceptor should be operated in order to match the development process proposed in Sec. 4.1. Therefore photoreceptors, which have a photogeneration efficiency γ of less than unity, must *a priori* be excluded for a highly sensitive electrophotographic process.

The carrier mobilities of most inorganic crystalline materials are usually high and of the order $\geq 10^2$ cm^2/V sec, indicating broad bands
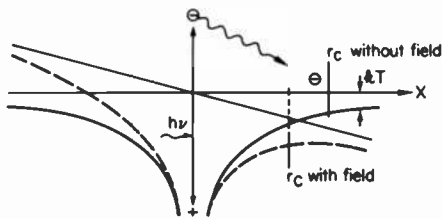

Fig. 9—Schematic representation of the thermalization of a charge carrier and of the change of r_c with applied field.

and therefore low effective masses. Therefore no problems should arise and, indeed, have never been observed concerning the photogeneration efficiency.

Organic crystalline solids usually show low mobilities,* which suggests narrow bands and hence high effective masses substantially above unity. For these materials, it is often assumed that the appropriate description of the motion of the carriers is the small-polaron model. Whatever model is assumed, γ is expected to be smaller than unity. This class of materials is, therefore, not suited to deliver a candidate for a highly efficient photoreceptor.

Similarly, the field dependence of γ has been established for a series of amorphous materials such as Se, As_2Se_3, PVK, and PVK-TNF, so that amorphous materials also seem to be unsuitable for our purposes. Whether the field dependence of γ in the above mentioned materials must be attributed to their specific molecular nature is not yet quite clear.

4.6 Transport Effects: Mobility and Recombination

We limit our discussion here to insulating photoreceptors, since the essential features a photoconductor must possess in order to satisfy our condition will become evident and can easily be generalized to semiconducting photoreceptors. If the photocurrent is saturated, then the efficiency is unity. Photocurrents (assuming blocking contacts) become saturated as a function of voltage above a threshold voltage determined by the condition[23] that the transit time T_{maj} of the majority carriers be equal to the dielectric relaxation time τ_{rel}

$$T_{maj} = \tau_{rel}, \qquad [26]$$

and that the transit time T_{min} of the minority carriers equals their lifetime,

$$T_{min} = \tau. \qquad [27]$$

For our purposes these conditions can be converted into a more practical form. The dielectric relaxation time is given by $\tau_{rel} = \epsilon\epsilon_o/(e\mu_n n)$ if electrons are the majority carriers. Assuming a homogeneous generation rate of the carriers in the photoreceptor, we can replace the electron density by $n = g\tau_n$ where τ_n is the mean free time of an electron in the conduction band. The transit time can be expressed in terms of the electric field and the electrode separation l as $T_{maj} = l/(\mu_n \vec{E})$. Using

---

*For a short review on organic photoconductors see Stockman.[22]

these relations we can calculate from Eq. [26] the threshold field for current saturation:

$$\vec{E}_{th_1} = \frac{eg\tau_n}{\epsilon\epsilon_0} . \tag{28}$$

Similarly, the condition for the minority carriers, which we assume to be the holes, can be modified to give a threshold field. Here one finds

$$\vec{E}_{th_2} = \frac{l}{\mu_p \tau} \tag{29}$$

If the light is strongly absorbed by the photoreceptor (so that the penetration depth of the light $1/\chi$ is smaller than the electrode separation), then l must be replaced by $1/\chi$ in Eq. [29], and Eq. [28] must be modified to reflect the fact that the region of carrier generation acts as a reservoir for carrier injection into the unilluminated region.

Whichever of the two fields of Eqs. [27] and [28] turns out to be greater will give the threshold field for current saturation. Except for high generation rates, it is safe to assume that the field determined by the majority carriers is smaller than that determined by the minority carriers. Therefore, in general, Eq. [29] will be the relevant one for our purposes. The important material parameters in this formula are the mobility of the minority carriers and the lifetime. From the discussion of the photogeneration efficiency γ, it was concluded that only high mobility materials are of interest in that context. The same consideration applies here. In this case, however, we must also take into account the lifetime. The lifetime is determined by the recombination, which we assume to follow a Shockley–Read mechanism. If we denote the density of recombination centers as R and their capture cross section as σ, then the lifetime is given by the wellknown expression, $\tau = (v_{th}\sigma R)^{-1}$ where v_{th} is the thermal velocity of the carriers. With this expression for τ, Eq. [29] can be rewritten

$$\vec{E}_{th} = \frac{lv_{th}\sigma R}{\mu_p} . \tag{30}$$

For a numerical estimate, we take as the electrode separation $l = 10^{-3}$ cm, the thermal velocity $v_{th} = 10^7$ cm/sec, the capture cross section $\sigma = 10^{-15}$ cm^2, and the density of recombination centers $R = 10^{15}$ cm^{-3}. The threshold field is then calculated to be 10^3 V/cm if we assume a mobility of the minority carriers of 10 cm^2/V sec. If the penetration depth $1/\chi$ of the light is smaller than l, than l has to be replaced by this value, thus giving an even lower threshold field. We expect therefore that recombination will not present a problem for operation of a photoreceptor below $\leq 10^4$ V/cm with an efficiency of unity.

4.7 Transport Effects: Trapping of Charge Carriers

Traps can give rise to a degradation of the efficiency. The efficiency will not be affected if a trapped carrier is reemitted from a trap and transported to the electrodes of the photoreceptor before the latent image is further processed. Otherwise the efficiency is reduced. Therefore, we will consider a trap deep here if it stores charge for a period longer than this handling time. A charge carrier will arrive at the electrodes if the distance it travels within time T_l before the latent image is developed is large compared to the electrode separation l. Hence, the following condition should hold:

$$l < \vec{E}\mu\tau\alpha. \tag{31}$$

The product $\vec{E}\mu\tau$ is the mean free path of a carrier before capture by a trap and α is a factor describing the frequency with which a carrier is emitted from a trap within time T_l. If the emission probability from a trap is ν, then

$$\alpha = \nu T_l. \tag{32}$$

The emission probability ν and the mean free time τ are related, and one obtains for the product $(\nu\tau)$ the expression

$$(\nu\tau) = \frac{N_{eff}}{N_D} \exp\left\{-\frac{\Delta E}{kT}\right\}. \tag{33}$$

Here N_D is the density of traps, ΔE is their separation from the corresponding band, and N_{eff} is the effective density of states.

Eqs. [31]–[33] give then a threshold for the energy ΔE of a trap below which the efficiency is not affected, the condition being

$$\Delta E \leq kT \ln\left(\frac{N_{eff} T_l \mu \vec{E}}{N_D l}\right). \tag{34}$$

In this formula the actual field has been replaced by an average field $\vec{E}$ so that $l/\mu\vec{E}$ represents the transit time of a carrier.

A numerical example gives an energy ΔE of 0.6 eV that a trap may have without affecting the efficiency. This value of ΔE was obtained assuming that for $T_l = 1$ sec, $l = 10^{-3}$ cm, $\vec{E} = 10$V/cm, $\mu = 1$ cm^2/Vsec, $N_D = 10^{15}$ cm^{-3}, and $N_{eff} = 10^{18}$ cm^{-3}.

4.7 Dark Decay

In all our considerations it has been tacitly implied that the photoreceptor is sensitive in the whole visible range of the spectrum. In this case, the bandgap of the material would be approximately 1.6 eV, since pho-

toexcitation then occurs across the bandgap for wavelengths $\lambda \leq 7800$ Å. A lower limit of the useful bandgap arises from the dark decay. In the charged state, the thermal equilibrium is usually strongly disturbed in the photoreceptor, and a Fermi level can no longer strictly be defined. The rate of thermal generation of electrons and holes must be identical, however, in order to satisfy steady-state conditions. This leads to a demarcation level near the middle of the forbidden gap such that states above this level are substantially empty and states below are substantially filled with electrons. A small current is due to the thermal generation of charge carriers. If we assume essentially homogeneous distribution of imperfect states in the forbidden gap, a two-step process is responsible for the generation in the dark—states at or near the middle of the forbidden gap are emptied by excitation of electrons to the conduction band and are refilled by electrons from the valence band at the same rate. This thermal generation process of free electrons and holes occurs at a higher rate than the direct excitation across the bandgap and than the generation due to impurity states that are not located close to the middle of the forbidden gap.

The charge carriers are swept out of the photoreceptor and if no transport limitations occur, the current density is given by

$$j = eN_D v_{th} \sigma N_{eff} \exp\left\{-\frac{E_g}{2kT}\right\} l. \qquad [35]$$

Here N_D is the density of states filled with electrons at midgap, N_{eff} is the effective density of states, E_g is the width of the forbidden gap, and the other symbols have their usual meaning. From [16], we obtain the discharge time due to this current. Since the width of the forbidden gap has to be close to 1.6 eV, however, it is more interesting to calculate the density of imperfection states near midgap that can be tolerated in order to obtain a sufficiently long dark decay time. Combining Eqs. [35] and [16] we obtain

$$N_D = \frac{\epsilon \epsilon_0}{l^2} \cdot \frac{V \exp\left(\frac{E_g}{2kT}\right)}{e v_{th} \sigma N_{eff} T}. \qquad [36]$$

A numerical estimate gives a density N_D of 10^{16} cm^{-3} for a dark discharge time t of 300 sec and for a photoreceptor with a bandgap of 1.6 eV. The other parameters were $N_{eff} = 10^{18}$ cm^{-3}, $v_{th} = 10^7$ cm/sec, $\sigma = 10^{-15}$ cm^2, and $l = 10^{-3}$ cm. This density of defect states is indeed surprisingly high.

There are, of course, other reasons for a dark current to flow, such as nonideal blocking contacts, high field effects at the contacts, etc.[24] These mechanisms are not directly related to the property of the photoreceptor,

and will not be discussed here. In practice, these effects could become important if they give rise to higher dark discharge rates than those expected on the basis of Eq. [35].

5. Experimental Feasability Study

An experimental study of the ideas outlined in the previous sections will have to comprise first a demonstration of the sensitivity of the development process and then the selection of a photoreceptor with the desired properties. In the final test, both will be combined to determine if the sensitivity can be substantially improved.

5.1 The Development Process

(a) *Experimental*
To test the sensitivity of the development process, we first simulated the latent image by applying a voltage to a conductor and by inducing the charge on the insulating film (Fig. 10). The amount of the induced and of the transferred charge can be measured, so that losses of the charge upon lifting off the film could be determined. The optical density upon development was measured as a function of the transferred charge and of the voltage applied to the conductor. Resolution test were included in the experiments by using bar-pattern-shaped conductors. The storage capability of the insulating film was determined by remeasuring the charge remaining on the film after a time t had elapsed after charging. Subsequently, the charge pattern was developed in order to check the loss in resolution. The homogeneity of the charge transferred to a film and the storage time of the charge on the film depend on the polymer film used. Our preferred material was polycarbonate, a commercially available polymer.

(b) *Results*

The first point to test was the sensitivity of the developing process. When an attempt was made to transfer higher charges, the curve usually flattened off and circular uncharged areas appeared; upon toning, these
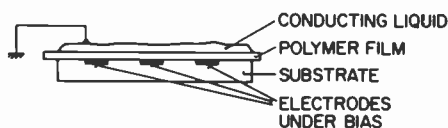

CONDUCTING LIQUID
POLYMER FILM
SUBSTRATE
ELECTRODES
UNDER BIAS

Fig. 10—Configuration used for simulating latent images.

became visible as white spots. The charge induced and transferred to the polycarbonate film was found to increase linearly with applied voltage up to a charge density of approximately 4.10^{-9} C/cm^2, which corresponds to 2.5×10^{10} elementary charges/cm^2. The curves shown in Fig. 11 were taken for films of different thickness and different relative dielectric constants. The ratio of the charges transferred to the two films at a certain voltage is determined exactly by the ratio of the thickness and of the dielectric constant of the films.

The charge transferred at $V = 0$ is finite. Variations of the experimental conditions proved that the charge transferred to the film at $V = 0$ is due to interfacial phenomena between the liquid and the polycarbonate film, as well as due to the contact potential difference between the grounding electrode and the electrode that was biased if measurements with $V \neq 0$ were made.

The optical density as a function of the charge density on the polymer film is shown in Fig. 12. The toner used for these experiments was Xerox toner 06 C 25 L. The size of the toner particles was determined with a microscope and found to be 12–15 μm, i.e., substantially larger than the assumed size of the particles in our previous considerations (dry toners with smaller particle sizes were not available). An optical density of 2 was obtained at a charge density of 2×10^{10} elementary charges/cm^2.
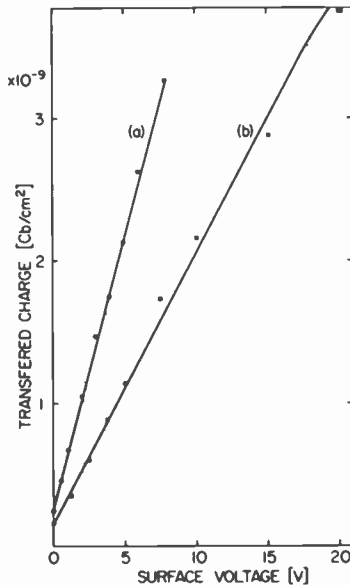

Fig. 11—Induced and transferred charge as a function of voltage. Parameter is the film thickness.
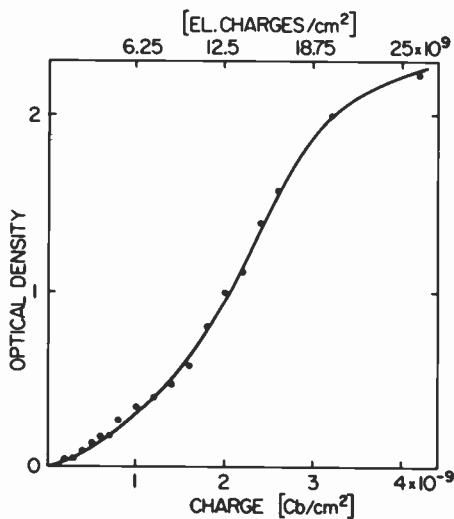
Fig. 12—Optical density as a function of charge density on the polymer film. Toner used is Xerox 06 C 25 L.

The gradation of the development process is rather steep, the whole optical density range being covered by the small charge density range of between about 0.5 and 2.5×10^{10} elementary charges/cm^2. It is not known, whether this lack in performance is due to the large particle size of the toner or due an incomplete toner deposition in the weakly charged areas. The background density, or fog, is low according to these experiments, of the order of 0.05. The graininess of the image is high due to the rather large toner particles in the case of dry toner. This is evidenced by the image of a charge pattern (Fig. 13). The toned area has an optical density of about 1.2.

The resolution obtainable was influenced by three factors—the particle size of the toner, the thickness of the film to which the charge pattern was transferred, and the spreading of the charge in or on the film. We will only explore the question of the charge spreading; this is the most important question because the others can, in principle at least, be dealt with by appropriate selection of the toners and film thickness.

The charge may spread either through the bulk or along the surface by injection or it may be neutralized by the intrinsic conductivity of the polycarbonate film itself or by the conductivity of the air. A bar shaped pattern combined with an ∼1 cm^2 uniform area transferred to the film represents a convenient means to distinguish the various effects. A loss in resolution gives information on the charge spreading; a loss in charge can be observed by measuring the charge on the film.
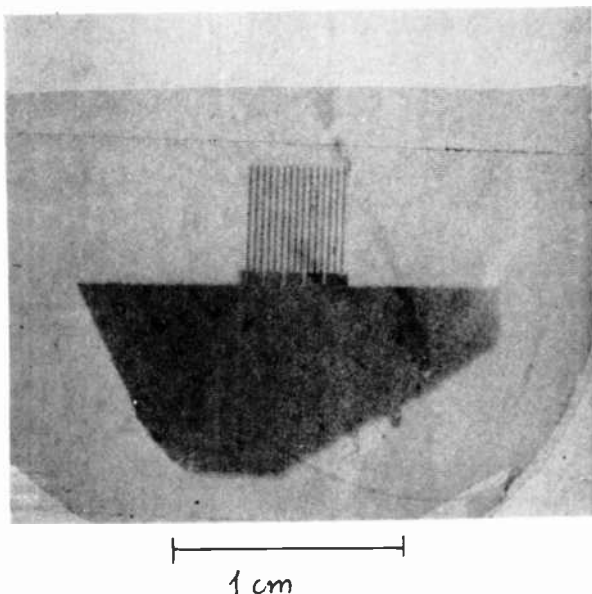
Fig. 13—Image of a test pattern used for the simulation experiments.

After the charge was remeasured, the film could again be stored, but this is not possible after the resolution test, since this test is made by toning and subsequent comparison of the image with the original.

The relative loss $\Delta Q/Q$ of the charge as a function of time is plotted in Fig. 14. The samples were stored at room temperature in a desk drawer. The loss increases linearly with the logarithm of time up to 100 days, which indicates a decreasing loss rate with time. The loss after 100 days was 15%. The sample measured after 360 days storage showed an anomalously large increase in the loss of charge, which must have been due to some catastrophic event. The images of the patterns are shown in Fig. 15. Surprisingly, there is no substantial increase in the width of bars visible, even in the case of the sample that had suffered from the catastrophic loss of charge.

5.2 The Photoreceptor

(a) Selection of Material
The bandgap as well as the mobilities of the material to be selected must fall within the range proposed in Sections 4.2–4.8, i.e., the width of the forbidden band has to be close to 1.6 eV and the carrier mobilities should be greater than 10^2 cm^2/Vsec. Several materials are close to these spec-
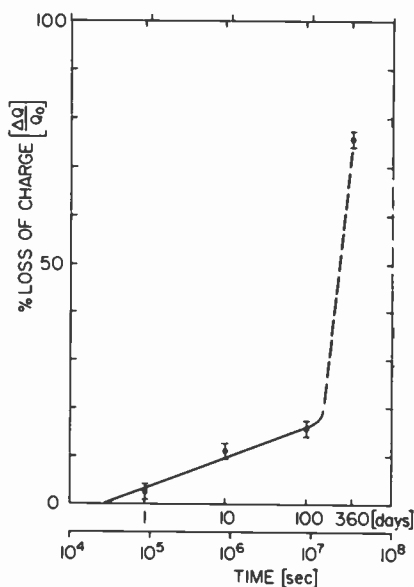
Fig. 14—Relative loss of charge on a polycarbonate film as a function of time.

ifications—Si (E_G = 1.1 eV), CdSe (E_G = 1.7 eV), CdTe (E_G = 1.5 eV), GaAs (E_G = 1.45 eV), and InP (E_G = 1.25 eV). The samples of CdTe, GaAs, and InP available could not be charged, the reasons being unknown. The Si samples could be charged but had a fast dark decay. The electrical properties of CdSe seemed to be most promising, and first experiments with single crystals indicated good charge acceptance. There were several problems to be solved. Can the CdSe be prepared with sufficient purity and homogeneity to provide an operation range of the layers at fields below 10^4 V/cm at an efficiency of unity? The preparation of the material and the details of its photoelectric properties will be reported elsewhere.[25] We restrict ourselves here to a presentation of the electrophotographic properties.

(b) Light Sensitivity of CdSe Layers

The optical density versus exposure characteristic of an electrophotographically produced image is, in general, influenced by the light-induced discharge characteristic and the sensitivity as measured by the exposure time needed to discharge the photoreceptor completely. Therefore, not only the discharge time but also the surface voltage versus time characteristics were studied in detail. The CdSe layers we investigated could only be charged negatively.
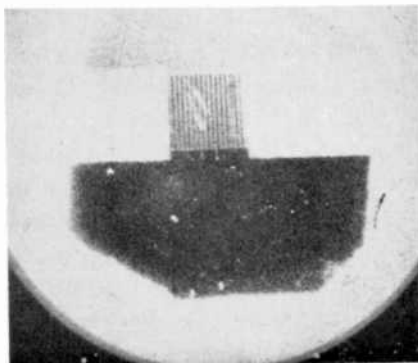
10 days
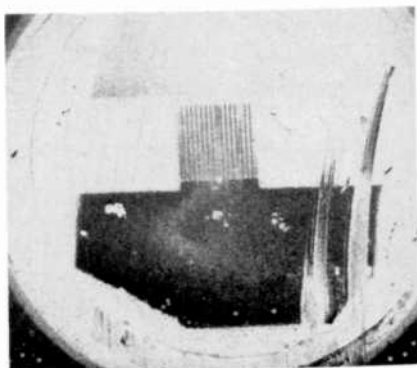
100 days
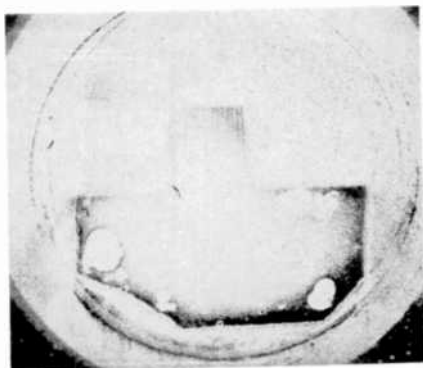
360 days

1 cm

Fig. 15—Developed test pattern whose loss of charge is given in Fig. 14.

with other photoreceptors shown in Fig. 18, therefore, a wide spread of data is given. The sensitivity of the photoreceptor plotted in this figure is proportional to η^{-1}. Thus it is the inverse of the number of photons per cm^2 needed to discharge the layer to 10% of its initial voltage. The sensitivity of the CdSe layers is independent of wavelength below $\lambda = 7000$ Å and drops to lower values at longer wavelengths. All the other electrophotographic materials are less sensitive over the whole visible spectral range. As-Sb-Se and Se photoreceptors are of comparable sensitivity in the spectral range below $\lambda = 4000$ Å, which is less interesting for photography. The data for the other materials were taken from Schaffert.[26]

(c) The Dark Decay of CdSe Layers

To be useful, the photoreceptor must be able to store an electrostatic charge pattern for periods substantially longer than the period of time between charging and transfer of the latent image to the polymer film. The faster the dark decay the more distortion of the information content.

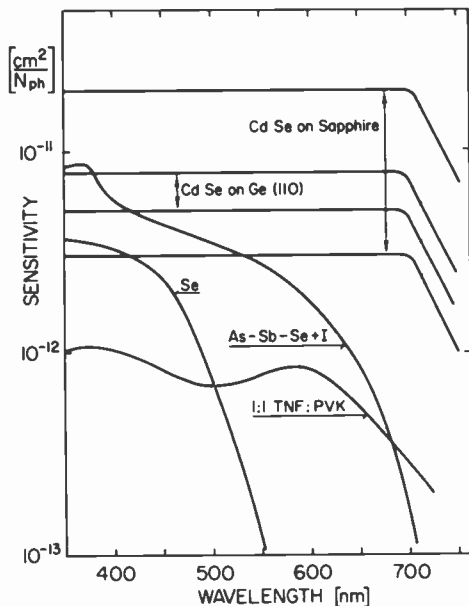The dark decay of the layers was found to be of the order of 300 sec-

Fig. 18—Photosensitivity of various photoreceptors in comparison to CdSe. The data for Se, As-Sb-Se+I, and TNF:PVK are taken from Schaffert.[26]

onds. The best fit to the dark decay characteristic was a logarithmic time law:

$$V = V_i - V_k \log\left(1 + \frac{t}{t_0}\right). \tag{37}$$

V_k and t_0 are empirical constants and V_i is the initial voltage. Typical values for V_k are 1 V and for the time constant $t_0 = 1$ sec. The logarithmic time law indicates a decay rate of the voltage that decreases with time. By differentiation of Eq. [37] with respect to time, one obtains the rate of change of the voltage:

$$\frac{dV}{dt} = -\frac{V_k}{t_0} M \frac{1}{e^{\frac{V_i - V}{MV_k}}} \quad \text{for } (M = \log e = 0.43) \tag{38}$$

The rate of change dV/dt decreases, as is easily verified with the above constants for V_k and t_0, to $\frac{1}{50}$ of its initial value when the surface voltage reaches half of its initial value. Thus, in order to reduce the change of the surface voltage within the time of handling, it is advantageous to wait until the surface voltage and, hence, the dark decay rate has reached a certain value before taking a picture.

The dark decay rate increases significantly with temperature. Though, in principle, the logarithmic time law can be explained by various mechanisms, inconsistencies and ambiguities remain for the explanation of this temperature dependence. Therefore, no satisfactory mechanism for the dark decay can be given at the present time.

5.3 Results with an Experimental Camera

The transfer of latent images from CdSe layers to polycarbonate films requires the construction of a photographic apparatus that provides the following functions—charging of the CdSe layer with a corona or some other means, exposure of the charged CdSe, bringing the polymer film into close contact with the photoreceptor, induction of the charge, and transfer of the latent image to the polycarbonate film.

To establish a correlation between our definition of the sensitivity S of Eq. [1] and the ASA speed normally used in photography, we measured the brightness of the scene to be taken with an exposure meter. To obtain an image, a certain exposure time and stop had to be chosen. With these data, the sensitivity could then be directly read on the scale of the exposure meter.

The scene used was a television test pattern that includes resolution elements as well as a gray scale in 11 steps. A picture taken of the test pattern is shown in Fig. 19. The sensitivity of this particular CdSe layer
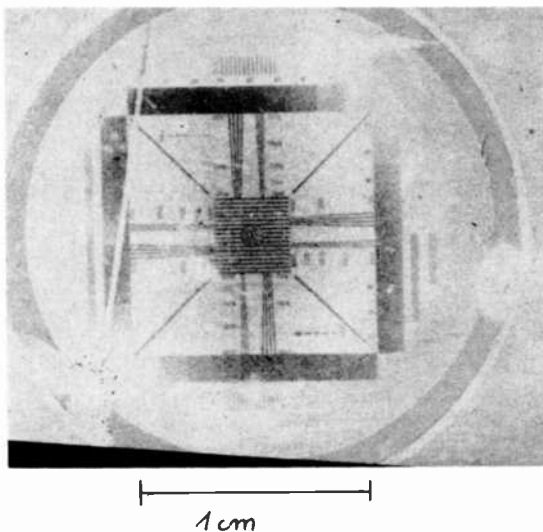
Fig. 19—TV-test pattern taken with an experimental electrophotographic camera. Sensitivity of the CdSe-layer ~100 ASA.

was 100 ASA, the picture was developed with powder toner. The thickness of the polycarbonate film to which the latent image was transferred was 12 μm.

The image obtained is characterized by a rather high background density or fog and a lack of a good gray scale. The fog, though not unexpected, is high and inhomogeneous. Briefly, the image quality is below what would have been expected on the basis of the simulation experiments with the toner. Therefore the suspicion was that the lack in image quality can be traced back to other sources. Some experiments were made to clarify this.

Fig. 20 shows a sequence of pictures obtained by exposing a charged layer to increasing amounts of light. The inhomogeneous charge acceptance, the graininess of the prints (which is definitively in excess of that of the print in Fig. 13 obtained in the simulation experiments) and possibly also an inhomogeneous photosensitivity are evident. We conclude from this experiment, that the failure to reproduce a gray scale, as well as the unexpected high background density, is due to a lack of spatial homogeneity of the charge acceptance and of the photosensitivity of the CdSe layer. Both effects give variations of the optical density comparable to what should be obtained with the gray scale.

Exposure time: 0.2 sec | 0.1 sec | 0.04 sec | 0.02 sec | 0.01 sec | 0.004 sec | unexposed | Simulated 10V applied
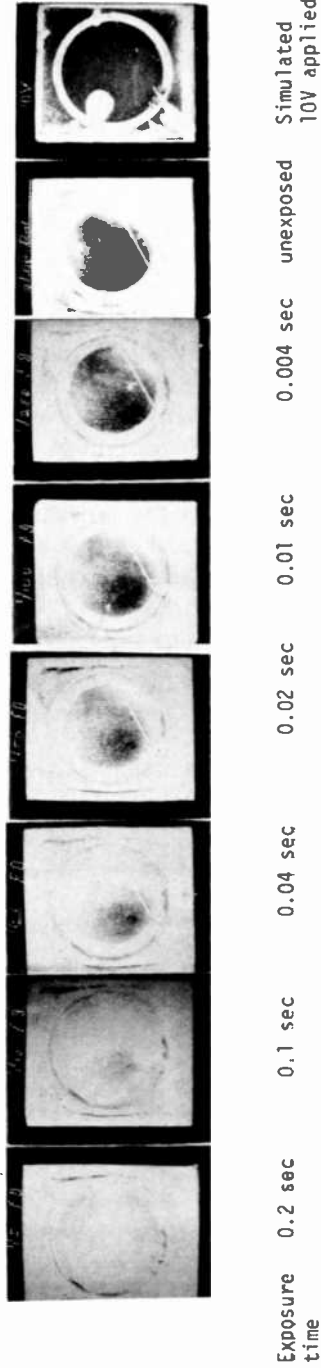
Fig. 20—Images of an supposedly uniformly charged CdSe layer exposed to increasing amounts of light.

6 Conclusion

The background for an experimental study of the sensitivity of the electrophotographic process was obtained from a theoretical consideration of the limits of electrophotography. The conclusions of the theoretical study are:

(1) The sensitivity of the development process is such that an optical density of 2 with reasonable signal-to-noise ratio can be obtained with a charge density as low as $1-2 \times 10^{10}$ elementary charges/cm^2. The optical density should, within a wide range of toner particles, be independent of the particle size. The assumption is that the charge pattern is available in a monopolar form.

(2) It should be possible to prepare photoreceptors that operate at surface charge densities of $10^{10}-10^{11}$ elementary charges/cm^2 with an efficiency of unity. Thus, this surface charge can be dissipated with approximately the same number of photons.

(3) Use of such a photoreceptor and transfer of the latent image into a monopolar charge pattern will give a highly sensitive electrophotographic process (sensitivity comparable to that of silver halide photography).

The experimental study indicated, that a sensitivity of ~ASA 100 can be achieved if CdSe layers are used as photoreceptors and if the transfer technique described previously is used. The resolution of the process was satisfactory, the storage capability of the latent image on the polycarbonate film was of the order of 100 days, and the optical density was found to be 2 at a surface charge density of 2.5×10^{10} elementary charges/cm^2.

Unsatisfactory results were obtained in that the reproduction of gray scale was poor, the toned areas showed much graininess, and there was a high background optical density. These deficiencies were traced back primarily to an inhomogeneous charge acceptance and photosensitivity of the CdSe layers, which gave rise to strong distortions of gray tones. Certainly, an improved photoreceptor should reveal the exact limitations of the electrophotographic process with respect to image quality.

Acknowledgment

References

[1] W. E. Bixby, P. G. Andrus, L. E. Walkup, *Phot. Eng.*, **5**, p. 210, 1954.

[2] Characteristic Curves for positive silverhalide films may be found, e.g., in the *Basic Photographic Sensitometry Workbook*, Kodak Publication Z-22-Ed, 2nd edition, 1971.

[3] For a definition of ASA-speed see, e.g., *Electrooptics Handbook*, RCA, Solid-State Div., Somerville, N.J. 07930.

[4] H. Fiedler, H. W. Stottmeister, "Investigations of Triboelectric Behavior of Cascade Developers," *J. Signal AM.*, **4**, p. 311, 1976.

[5] A. Rose, *Vision, Human and Electronic*, Plenum Press, N.Y., N.Y. (1973).

[6] H. Kiess, "A Step Towards High-sensitivity Electrophotography," *The J. of Phot. Science*, **25** p. 121, 1977.

[7] Meinke-Gundlach, *Taschenbuch d. Hochfrequenztechnik*, 1962, Springer Verlag, Berlin (1962).

[8] A discussion of noise in the toner deposition process and in other means to develop electrostatic charge pattern will be presented in an article in *Reports on Progress in Imaging Science and Technology*, to be published by The Focal Library.

[9] For example, K. Hoffmann, "Sandwichsysteme," 4, Internat. Kongress für Reprographie und Information, 1975.

[10] H. S. Sommers Jr., "Response of Photoconducting Imaging Devices with Floating Electrodes," *J.A.P.*, **34**, p. 2923, 1963.

[11] A. Rose, "The Role of Space-Charge-Limited Currents in Photoconductivity-Controlled Devices," *IEE Trans. Electron Devices*, ED, **19**, p. 430, 1972.

[12] A. Rose and M. A. Lampert, "Gain-Bandwidth Product for Photoconductors," *RCA Review*, **20**, p. 57, March 1959.

[13] A. Rose, *Concepts in Photoconductivity and Allied Problems*, Interscience Publications (1963).

[14] H. Kiess, "The Pysics of Electrical Changing and Discharging of Semiconductors," *RCA Review*, **36**, p. 667, Dec. 1975.

[15] P. J. Warter, *Proc. Third Int. Conf. on Photoconductors*, p. 311, Pergamon Press, Oxford (1971).

[16] J. C. Knights and E. A. Davis, "Photogeneration of Charge Carriers in Amorphous Selenium," *J. Phys. Chem. Sol.*, **35**, p. 543, 1974.

[17] A. Rose, "The Acoustoelectric Effects and Energy Losses in Hot Electrons—IV," *RCA Review*, **30**, p. 435, 1969.

[18] H. Kiess, to be published in, *Reports on Progress in Imaging Science and Technology*, The Focal Library.

[19] N. F. Mott, "Electrons in Disordered Structures," *Adv. Phys.*, **16**, p. 49, 1967.

[20] M. H. Cohen, "Basic Concepts in the Theory of Amorphous Semiconductors," *Proc Tenth Int. Conf. on the Phys. of Semicond.*, Cambridge Mass, 1970.

[21] R. H. Bube, "Photoconductivity in Amorphous Semiconductors," *RCA Review*, **36**, p. 467, 1975.

[22] D. L. Stockman, "The Present Status of Organic Photoconductors in Electrophotography," in *Current Problems in Electrophotography*, ed. by W. F. Berg and K. Hauffe, Walter de Gruyter (1972).

[23] F. Stockmann, "Zur Sàttigung von Photostromen in starken elektrischen Feldern," *Phys. Stat. Sol.*, **2**, p. 517, 1962.

[24] H. Kiess, "On the Dark Decay of Negatively Charged ZnO Single Crystals," in *Current Problems in Electrophotography*, ed. by W. F. Berg and K. Hauffe, Walter de Gruyter (1972).

[25] B. Curtis, H. Brunner, K. Frick and H. Kiess, to be published.

[26] R. M. Schaffert, *Electrophotography*, enlarged and revised Edition, The Focal Press (1975).

[27] D. M. Pai and R. C. Enck, "Photogeneration in Electrophotographic Materials," 1974 Summer Symposium, Photoconductor Image Technology, Theory and Practice, SPSE 1974.

Patents Issued to RCA Inventors

October

L. Abbott, G. W. Beakley, and R. E. Flory System for Passing Two Color TV Signals Through Non-Linear Path (4,120,001)

A. A. Ahmed Switchable Current Amplifiers (4,119,924)

R. A. Bartolini and J. P. Russell Duplicating a Holographic Record by Using Two Reference Beams (4,121,881)

T. V. Bolger and R. A. Dischert Signal Defect Compensator (4,122,489)

R. J. Bosselaers Frequency Synthesizer with Frequency Modulated Output (4,119,925)

T. N. Chin Cathode for Flat Panel Display (4,119,882)

L. A. Cochran and R. L. Shanley, 2nd Service Switch Arrangement for a Color Television Receiver (4,123,776)

T. L. Credelle System for Achieving Image Uniformity in Display Devices (4,121,137)

J. M. Cusack Method and Apparatus for Determining a Signal of Uniform Period (4,121,211)

W. F. Dietz North-South Pincushion Distortion Correction Circuit (4,118,656)

E. C. Fox Signal Defect Detection and Compensation with Signal De-Emphasis (4,119,812)

R. A. Gange Cathode Structure and Method of Operating the Same (4,121,130)

A. M. Goldschmidt Turntable Rotational Speed and Phase Control System for a VideoDisc Play/Record Apparatus (4,123,779)

L. A. Goodman, A. W. Levine, and D. Meyerhofer Electro-Optic Device (4,120,567)

G. M. Harayda Data Encoding Keyboard (4,120,044)

W. Hinn Video Amplifier with Suppressed Radio Frequency Radiation (4,118,731)

W. Hulstrunk Semiconductor Device Having Reduced Leakage Current (4,122,483)

A. C. Ipri and J. H. Scott, Jr. Integrated Circuit Structure and Method for Making Same (4,119,992)

H. Kressel and F. Z. Hawrylo Lateral Mode Control in Semiconductor Lasers (4,122,410)

V. Krishnamurthy Cathode-Ray Tube with Double Tension Band (4,121,257)

T. F. Lenihan, Single Wire Transmission of Multiple Switch Operations (4,118,700)

H. G. Lewis, Jr. and S. B. Calo Error Detection and Correction (4,119,945)

A. C. Luther, Jr. and D. A. Sauer AM Transmitter with an Offest Voltage to the RF Stage to Compensate for Switching Time of the Modulators (4,122,415)

D. P. Marinelli Method for Depositing Epitaxial Semiconductor from the Liquid Phase (4,123,302)

W. D. Masterton Cathode-Ray Tube with a Corrugated Mask Having a Corrugated Skirt (4,122,368)

D. F. Medendorp and P. C. Schwabel Amplifier Protection Circuit (4,122,400)

L. P. Nahay Digital Time Division Multiplex Switching System (4,119,807)

J. S. Oblak and P. J. Schmalz Shielded, DC Isolated RF Connector Assemby (4,122,416)

C. J. Petrizio Touch Switch Circuits (4,119,864)

C. E. Profera Antenna Feed Network (4,122,453)

J. J. Risko and L. S. Napoli Amplitude Modulated Impatt Diode Oscillator and a Low Cost Communication System Using Same (4,118,598)

L. R. Rockett, Jr. CCD Binary-to-Gray Code Generator (4,119,961)

R. L. Shanley, 2nd Set-Up Arrangement for a Color Television Receiver (4,118,729)

S. Shwartzman and A. Mayer Transducer Assembly for Megasonic Cleaning (4,118,649)

W. A. Sonntag and T. F. Simpson Method and Apparatus for Simulating Magnetic Environment of Television Receivers (4,122,485)

C. M. Wine Memory Type Tuning System with Provisions to Facilitate Setup (4,123,713)

November

K. C. Adam and F. C. Easter Over-Current Protection Circuit for Voltage Regulator (4,127,885)

A. A. Ahmed Delayed Kinescope Blanking Pulse Generator (4,126,815)

H. R. Beelitz and D. R. Preslar Electrical Circuit for Multiplexing and Dividing Different Bands or Frequencies (4,127,820)

H. R. Beelitz and D. R. Preslar Integrated Circuit Mesa Bipolar Device on Insulating Substrate Incorporating Schottky Barrier Contact (4,127,860)

A. E. Bell, D. E. Carlson, and B. F. Williams Photovoltaic Device Having Increased Absorption Efficiency (4,126,150)

D. P. Bortfeld, R. W. Cohen, and D. A. DeWolf Electron Gun Having a Distributed Electrostatic Lens (4,124,810)

J. E. Carnes and R. H. Dawson Balanced Capacitance Charge Transfer Device (4,126,836)

J. T. Coble Spiked Low-Voltage Aging of Cathode-Ray Tubes (4,125,306)

C. F. Coleman VideoDisc Insertion/Extraction System for a VideoDisc Player (4,124,866)

F. C. Easter Over-Current Protection Circuit for Voltage Regulator (4,127,886)

D. W. Fairbanks Solar Energy Heat Apparatus (4,126,121)

R. E. Fernsler, D. W. Luz, and J. C. Peer Inrush Current Start-Up Circuit for a Television Receiver (4,127,875)

J. S. Fuhrer and E. O. Keizer Narrowed-Electrode Pickup Stylus for VideoDisc Systems (4,124,867)

L. A. Goodman, W. B. Hall, and K. W. Hang Self Illuminated Liquid Crystal Display Device (4,126,384)

L. S. Greenberg Plastic Encapsulated Semiconductor Devices (4,124,864)

R. E. Hanson and R. E. Tetrev Compression Test Using Battery Voltage Waveform During Cranking (4,126,037)

J. H. Helm Rotational Restraint for VideoDisc Package (4,124,118)

K. Katagi Image Resolution Enhancement Method and Apparatus (4,127,873)

S. W. Kessler, Jr. and J. A. Olmstead Semiconductor Device with Ballast Resistor Adapted for a Transcalent Device (4,126,879)

B. A. Kirschner Phase Lock Loop Indicator (4,125,815)

H. W. Lehmann and R. W. Widmer Fabrication of Multi-Level Relief Patterns in a Substrate (4,124,473)

E. S. Lo Novel Amino Siloxane Lubricants (4,127,872)

B. G. Marks High Voltage Electron Tube Base with Drip Relief Means (4,127,313)

F. J. Marlowe Electron Gun Control System (4,126,814)

J. H. McCusker and S. S. Perlman Uniform Surface Acoustic Wave Transducer Configuration Having Improved Frequency Selectivity (4,126,838)

K. Miyatani and I. Sato Grooved N-Type TiO_2 Semiconductor Anode for a Water Photolysis Apparatus (4,124,464)

J. J. Moscony and G. S. Gadbois Etching a Succession of Articles from a Strip of Sheet Metal (4,126,510)

J. T. O'Brien, A. C. Limm, P. Nyul, and V. S. Tassia, Jr. Radiation Emitter-Detector Package (4,125,777)

E. S. Poliniak and N. V. Desai Method of Transferring a Surface Relief Pattern from a Wet Poly(Olefin Sulfone) Layer to a Metal Layer (4,126,712)

J. K. Randolph Automatic Release Mechanism for a Tether (4,126,850)

O. H. Schade, Jr. Low Leakage Gate Protection Circuit (4,126,830)

F. N. Sechi Microwave Coupler (4,124,823)

R. L. Shanley, 2nd Kinescope Beam Current Limiter Employing Automatic Sequential Control of Image Contrast and Brightness to Limit Beam Current (4,126,884)

D. H. Willis High Voltage Protection Circuit (4,126,816)

December

J. A. Allen and C. F. Coleman Stylus Position Control System (4,128,247)

C. H. Anderson Beam Guide for Display Device with Beam Injection Means (4,128,784)

T. W. Branton Cathode Ray Tube with Stress-Relieved Slot-Aperture Shadow Mask (4,131,822)

B. R. Clay and D. A. Gore Hologram Having Expanded Viewing Area (4,130,338)

T. L. Credelle Modular Flat Display Device with Beam Convergence (4,131,823)

T. J. Cunningham and H. L. Schwartzberg Solder Connection between Copper and Aluminum Conductors (4,129,744)

C. A. Deckert Pretreatment of Polyvinyl Chloride Plastics for Electroless Deposition (4,131,698)

W. Denhollander Side Pincushion Correction Circuit with Low Dissipation Damping (4,130,783)

E. B. Gamble DC Converter Using Pulsed Resonant Circuit (4,128,868)

P. E. Haferl Correction Circuit for Load Dependent Raster Distortion (4,129,806)

M. R. Johns Circularly Polarized Antenna Using Slotted Cylinder and Conductive Rods (4,129,871)

K. Katagi Range Mark Generation (4,128,834)

K. Knop Fine-Line Diffractive Subtractive Color Filters (4,130,347)

I. Ladany and H. Kressel Degradation Resistance of Semiconductor Electroluminescent Devices (4,131,904)

R. D. Larrabee Power Transfer Apparatus (4,131,827)

C. J. Martin and R. J. Ryan Vinyl Chloride Based Injection Molding Composition (4,129,536)

R. S. Mezrich and E. T. Koenig High Resolution Pulse-Echo Ultrasonic-Imaging Display System (4,131,021)

R. S. Mezrich Pulse-Echo Ultrasonic-Imaging Display System (4,131,022)

R. S. Mezrich and C. H. Anderson Pulse-Echo Ultrasonic-Imaging Display System (4,131,023)

R. S. Mezrich and J. Y. Avins Pulse-Echo Ultrasonic-Imaging Display System (4,131,025)

C. R. Mills Circuit Test Apparatus (4,129,826)

J. W. Mirsch Multilayered Deflection Yoke (4,128,824)

C. K. Mok Array of Directional Filters (4,129,840)

E. J. Nossen and V. F. Volertas Unidirectional Phase Shift Keyed Communication System (4,130,802)

C. F. Smollin Circuit for Rearranging Word Bits (4,130,886)

D. J. Tamutus Method of Making a Thermoplastic Lens by Vacuum Forming (4,129,628)

D. H. Vilkomerson and R. S. Mezrich Pulse-Echo Ultrasonic-Imaging Display System (4,131,024)

P. P. Webb Multi-Element Avalanche Photodiode Having Reduced Electrical Noise (4,129,878)

S. Weisbrod Image Display Device Commutator (4,129,804)

C. E. Weitzel and D. R. Capewell Method of Making Silicon on Sapphire Field Effect Transistors with Specifically Aligned Gates (4,131,496)

AUTHORS

George J. Brucker received the B.S. degree in physics from St. Peter's College, Jersey City, N.J., in 1943, the M.A. degree in physics from Columbia University, New York, N.Y., and the Ph.D. degree in physics from New York University, New York, in 1955.

For 11 years Dr. Brucker worked for USA ECOM at Fort Monmouth, New Jersey, where he did research work in high-energy radiation physics, especially the effects of radiation on organic and inorganic scintillating materials. In 1962 he joined the Astro-Electronics Division of RCA where he investigated multiple-charge exchange reactions in an accelerating electric field and carried out experimental studies of the electron beam-plasma interaction. His most recent work has been in the field of radiation damage to spacecraft systems and solid state devices, including a broad field of spacecraft applications such as sensors, power, communications, command and control, special experiments, and computers. Some of the spacecraft requiring hardening design included TIROS, RCA SATCOM, Atmosphere Explorer, and DMSP. Environments for these spacecraft and their systems cover the natural Van Allen belts as well as more complex nuclear bomb burst effects. Dr. Brucker studied the impact of radiation damage in silicon devices, such as experimental correlation of electron, proton, and neutron effects in transistors and solar cells. He was Project Scientist on a contract to study the effect of lithium on radiation damage in silicon, and he has recently investigated the use of CMOS/SOS and MNOS memory devices for a hardened computer as part of his work on the development of hardened semiconductor devices.

Dr. Brucker is a member of the American Physical Society.

Helmut Kiess attended the University of Stuttgart from 1953 to 1957 and the University of Darmstadt from 1958 to 1960. He received the doctor's degree from the University of Karlsruhe in 1963. Dr. Kiess joined the Laboratories RCA Ltd., Zürich, Switzerland in 1963 and since then has worked on the physics of photoconductors and insulators. During the period from July 1970 to April 1971 he was at RCA Laboratories in Princeton.

Ramon U. Martinelli received the A.B. and M.S. degrees from Dartmouth College, Hanover, N.H., in 1960 and 1962, respectively, and the Ph.D. degree in electrical engineering from Princeton University, Princeton, N.J., in 1966.

He joined RCA Laboratories as a Member of the Technical Staff in 1966 and until 1974 worked on electron emission and transport problems. His present research is in the area of electron device physics.

Dr. Martinelli is a member of the American Physical Society.

Arye Rosen received the B.S.E.E. degree cum laude from Howard University in 1963 and the M.Sc.E. degree from Johns Hopkins University (which he attended on a Gillman Fellowship) in 1965. He was an instructor at Johns Hopkins during 1963–64. From 1964 to 1967, Mr. Rosen was concerned with systems design at General Telephone and Electronics International, and with antenna and circuit design at Channel Master, Inc., and American Electronics Laboratories, Inc. In 1967, Mr. Rosen joined RCA Laboratories where he is presently engaged in the study and development of microwave circuits and devices. He is the recipient of a 1972 RCA Laboratories

Outstanding Achievement Award for a team effort in the development of S-band TRAPATT amplifiers. From 1970 to 1971, on leave of absence from RCA, Mr. Rosen was engaged in research in the Division of Cardiology at Jefferson Medical College in Philadelphia, Pa., where he received the degree of M.Sc. in Physiology and where he presently holds an appointment to the staff of the Department of Medicine.

Mr. Rosen is a member of Tau Beta Pi, Sigma Xi, and the Association of Professional Engineers of British Columbia.

Alfred Schwarzmann (M'66) was born in Bamberg, West Germany, on December 26, 1930. He received the B.Sc. degree in physics from La Salle College, Philadelphia, PA, in 1966.

He joined RCA at Moorestown, N.J. in 1956, as a Member of the Technical Staff where he has been engaged in the design of high-power transmitters. Since 1960 he has been a Senior Member of the Advanced Development Groups at RCA, where he has been conducting research and development on solid state and microwave integrated circuit components for radar and communications equipments.

George A. Swartz received the B.S. degree from Massachusetts Institute of Technology, Cambridge, in 1952 and the M.S. and Ph.D. degrees in physics from the University of Pennsylvania, Phildelphia, in 1954 and 1958, respectively.

He joined the technical staff of RCA Laboratories in 1957. His work has been in the fields of plasma propulsion, plasma stability, microwave phenomena in gaseous and solid-state plasmas, solid-state physics, and in the development of low-noise high-efficiency IMPATT diodes, the development of low-loss high-power p-i-n diodes, and, most recently, the development of high-efficiency solar cells for high-level solar concentration. His work in collaboration with L. Napoli on a beam-plasma amplifier was cited by Industrial Research magazine for an I-R 100 award in 1963. He has received two RCA Achievement Awards.

Dr. Swartz is a member of the American Physical Society and Sigma Xi.

Theodor M. Wagner received the Ing. grad. degree from the Oscar von Miller-Polytechnikum in Munich, Germany in 1953. He was employed with Rohde und Schwarz in circuit design of TV broadcast measuring equipment for six years. He was a group leader at Agfa-Gevaert's Lab of Physics, for six years prior to coming to the United States in 1964. In 1964 and 1965, he designed chroma processing circuits of color TV receivers with General Electric. In 1966 and 1967, his work included studies on vidicon tubes and the design of a high resolution industrial camera for medical and radar scope displays at General Electro-Dynamics Corp. in Garland, Texas.

He joined RCA Burbank in 1968. Mr. Wagner was a member of the team that received the 1969 David Sarnoff Outstanding Team Award in Engineering for the electro-optical design of the single-tube color camera. In 1972, Mr. Wagner transferred to the David Sarnoff Research Center at the RCA Laboratories in Princeton, N.J., where he is currently working on analyzing TV receiver colorimetry and optimizing measurement techniques.

He is member of the SMPTE and the SPSE.